

REPORT DOCUMENTATION PAGE

AFRL-SR-BL-TR-01-

Public reporting burden for this collection of information is estimated to average 1 hour per response, including the time for reviewing this collection of information. Send comments regarding this burden estimate or this burden to Department of Defense, Washington Headquarters Services, Directorate for Information Operations and Report 4302. Respondents should be aware that notwithstanding any other provision of law, no person shall be subject to any penal valid OMB control number. PLEASE DO NOT RETURN YOUR FORM TO THE ABOVE ADDRESS.

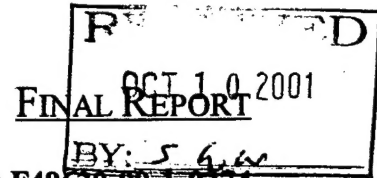
maintaining the
s for reducing
/A 22202-
lay a currently

0567

1. REPORT DATE (DD-MM-YYYY) 31 - 08 - 2001		2. REPORT TYPE Final Report		3. DATES COVERED June 1999- May 2001	
4. TITLE AND SUBTITLE High Temperature Fatigue Cracking Mechanisms				5a. CONTRACT NUMBER	
				5b. GRANT NUMBER F49620-99-1-0274	
				5c. PROGRAM ELEMENT NUMBER	
6. AUTHOR(S) Keh-Minn Chang, Bernard Cooper, Bruce Kang				5d. PROJECT NUMBER	
				5e. TASK NUMBER	
				5f. WORK UNIT NUMBER	
7. PERFORMING ORGANIZATION NAME(S) AND ADDRESS(ES) AND ADDRESS(ES) West Virginia University Morgantown, WV 26506				8. PERFORMING ORGANIZATION REPORT NUMBER	
9. SPONSORING / MONITORING AGENCY NAME(S) AND ADDRESS(ES) Air Force Office of Scientific Research 801 N. Randolph St. Arlington, VA 22203				10. SPONSOR/MONITOR'S ACRONYM(S)	
12. DISTRIBUTION / AVAILABILITY STATEMENT DISTRIBUTION STATEMENT A Approved for Public Release Distribution Unlimited					
13. SUPPLEMENTARY NOTES					
14. ABSTRACT The project progresses as planned in the proposal. During this 2-years project, we finished the following tasks: <ul style="list-style-type: none"> Development of a new methodology to evaluate the resistance on the time-dependent fatigue crack growth (FCG) behavior of the materials. A new concept of damage zone is introduced and verified experimentally the damage zone size of the various alloys and the relationship between damage zone size and the resistance of FCG. Characterization of time-dependent fatigue crack growth (FCG) behavior of selected alloys, including Waspaloy, U 720, IN 718, IN 706 and IN 783. Investigation of beneficial effect of creep on hold-time FCG of Waspaloy. Investigation of in-situ crack tip deformation in selected superalloys related to SAGBO damage. Research on the role of the nickel-oxygen interaction on the mechanism for grain boundary diffusion of oxygen and enhancement of that diffusion. 					
15. SUBJECT TERMS Fatigue Crack Growth, Time Dependence, Damage Zone, Oxygen Embrittlement					
16. SECURITY CLASSIFICATION OF: Unclassified			17. LIMITATION OF ABSTRACT	18. NUMBER OF PAGES	19a. NAME OF RESPONSIBLE PERSON
a. REPORT	b. ABSTRACT	c. THIS PAGE	UL	96	Keh-Minn Chang
					19b. TELEPHONE NUMBER (include area code) (304) 293-3111 ext. 2335

20011126 092

AIR FORCE OFFICE OF SCIENTIFIC RESEARCH (AFOSR)
NOTICE OF TRANSMITTAL DTIC. THIS TECHNICAL REPORT
HAS BEEN REVIEWED AND IS APPROVED FOR PUBLIC RELEASE
LAW AFR 190-12. DISTRIBUTION IS UNLIMITED.



DoD EPSCoR Grant F49620-99-1-0274
Air Force Office of Scientific Research

High-Temperature Fatigue Cracking Mechanisms

Principal Investigators

Keh-Minn Chang
Bruce Kang
Dept. of Mechanical and Aerospace Engineering

Bernard R. Cooper
Dept. of Physics

West Virginia University
Morgantown, WV

August 31, 2001

Table of Contents

1. Acknowledgement	1
2. Objectives	1
3. Status of Effort	1
4. Accomplishments/New Findings	2
4.1 New Methodology with Damage Zone Concept	3
4.2 Time Dependent Fatigue Crack Growth	12
4.3 Beneficial Effect of Creep on Hold-time FCG of Waspaloy	19
4.4 In-situ Crack Tip Deformation	22
4.5 Oxygen Impurities in NiAl: Relaxation Effects	28
5. Personnel Supported	33
6. Publications	34
7. Interactions/Transitions	35
Tables	37
Figure Captions	40

1. Acknowledgement

Special Metals Corp.(SMC) at Huntington, WV has provided a number of commercial grade superalloys, including Waspaloy, IN718, IN706, IN783, and U720. We would like to express our appreciation for their support of sufficient experimental materials. SMC technical staff, S. Patel, J.J. deBarbadillo, and S.K. Mannan, also offered many useful discussion and suggestions during the course of research.

2. Objectives

The objective of this research is to develop a comprehensive understanding of high-temperature fatigue cracking mechanisms in various high-strength superalloys. The alloying effects on fatigue cracking resistance will be studied through a multi-disciplinary effort, which combines metallurgy, micro-mechanics, finite element analysis, and material physics. The important goals to be achieved in this research are listed as follows:

- An innovative methodology to measure and to characterize the damage developed during high-temperature fatigue cracking process in selected commercial superalloys of industrial interest.
- Micro-mechanics study on the evolution of strain/stress fields near the crack tip as high-temperature fatigue cracking proceeds.
- Atomistic modeling of alloying effects on the selective oxidation behavior along grain boundaries and free surfaces.

A special attention in this research study will focus on distinguishing the internal (creep) and external (environmental) factors that contribute the time-dependence of high-temperature fatigue cracking.

3. Status of Effort

The project progresses as planned in the proposal. During this 2-years project, we finished the following tasks:

- Development of a new methodology to evaluate the resistance on the time-dependent fatigue crack growth (FCG) behavior of the materials. A new concept of damage zone is

introduced and verified experimentally the damage zone size of the various alloys and the relationship between damage zone size and the resistance of FCG.

- Characterization of time-dependent FCG behavior of selected alloys, including Waspaloy, U 720, IN718, IN706 and IN783.
- Investigation of beneficial effect of creep on hold-time FCG of Waspaloy.
- Investigation of in-situ crack tip deformation in selected superalloys related to SAGBO damage.
- Research on the role of the nickel-oxygen interaction on the mechanism for grain boundary diffusion of oxygen and enhancement of that diffusion.

4. Accomplishments/New Findings

Table I lists the chemical compositions of superalloys evaluated in this project. All the materials were provided by Special Metals Corp., Huntington, WV. The alloys were produced by standard manufacture processes including vacuum melting, forging and rolling. The four superalloys received commercial heat treatments, which are also given in Table I. IN783 with normal composition was performed three different heat treatments, and a high-Cr version (5.6% Cr) IN783 was just performed standard heat treatment (a).

(a) Normal heat treatment for both high-Cr alloy (code H) and normal composition alloy (code R).

1120 °C/1 hr, air cool; + 843°C/4 hrs, air cool + 720 °C/8hrs, furnace cool at 55 °C/ hr to 620 °C, hold at 620 °C for 8 hrs and then air cool.

(b) No β heat treatment for normal composition alloy (code S)

1120 °C/1 hr, water quench + 720 °C/8hrs, furnace cool at 55 °C/ hr to 620 °C, hold at 620 °C for 8 hrs and then air cool.

(c) Long term exposure (code U)

After normal heat treatment (R) , IN783 was exposed at 500°C for 3000 hrs.

4.1 New Methodology with Damage Zone Concept

4.1.1 Damage Zone Concept

In recent years, many models based on the linear elastic fracture mechanics (LEFM) have been proposed for fatigue crack growth. It has been established that fatigue crack growth rates (da/dN) in metals, generally vary with the alternating stress intensity factor $\Delta K = (K_{max} - K_{min})$. Most of the models have an exponential relationship between da/dN and ΔK . Different exponents have been obtained in different models. Although theoretically the linear elastic fracture mechanics approach can only be employed in entire elastic condition, it has been confirmed that LEFM is still valid under small yielding area condition (length of yielding area in front of the crack tip is much smaller than crack length).

Figure 1 shows the sketch of several fatigue crack growth models. There is a crack with a length l , suffering a load stress σ . Also there is a shear stress τ in front of the crack tip and the crack tip opening displacement is assumed to be δ . Although in most cases the nominal stress σ is lower than the yield stress of the materials, there is still a plastic zone, which appears because of the stress concentration. The length of the plastic zone is D . Most of the fatigue crack growth models are base on the sketch.

As mentioned by Davidson, the first category of the models are parametric, considering the relationship between the crack growth rate and a driving force, such as stress intensity range ΔK . These models do not address the physics of the processes near the crack tip, which lead to crack advancement. The second category of fatigue crack growth models consider the crack tip opening displacement to be proportional to the crack growth rate, which results in the growth rate being proportional to $(\Delta K)^2$. However, as mentioned by Paris, the exponent of the crack growth rate curve varies widely. The next category of the models focus on the damage in front of the crack tip. Mostly the damage was assumed to be proportional to the inelastic strain. In spite of the difference in the assumption of the models, the Paris Law was always obtained as:

$$\frac{da}{dN} = c \times (\Delta K)^n \quad (1)$$

where (da/dN) is the crack growth per cycle, ΔK is the stress intensity range, c and n are constants. The constants differ in various models.

Paris Law can be well employed for the fatigue test under high frequency or lower temperature when the crack growth rate is cycle dependent. If the test is carried out at higher temperatures and low frequency or longer holding-time, the time-dependent factors must be taken into account and the crack growth rate becomes time dependent.

Two reasons creep and oxidation, were reported to be responsible for the time-dependent fatigue crack growth behavior. Since the grain boundary is the fast channel for oxygen diffusion at high temperature, it has indicated that the Stress Assisted Grain Boundary Oxidation (SAGBO) plays the most important role on the environmental effect^{18,19}. The time dependent high temperature crack propagation rates of many materials in vacuum, as well as inert gas environments²⁰⁻²⁴, are lower in order of magnitude than air.

Although the environment effect has been well accepted as the principal reason for the time dependent crack growth, there are very few models to illustrate this behavior and there is still not a good parameter to evaluate the materials resistance on the time dependent crack growth. In this paper, we want to provide a new parameter, Damage Zone to explain the crack growth and evaluate the resistance of materials. The concept has been successfully employed on several superalloys.

It has been proposed that the crack growth is the result of material's damage in front of the crack tip. During the loading process, the resistance of material in front of the tip decreases, and will be less than a critical value which is necessary for preventing the crack growth. During the next loading cycle, the crack will pass through the damaged material, and the new damaged zone appears.

In the cycle dependent "pure" fatigue, the material in front of the crack tip is damaged only by cyclic loading. However, if the test is conducted at higher temperature and there is hold-time at max load in fatigue cycle, the time-dependent behaviors must be taken into account. Damage by cyclic loading accounts for a very less amount of the total damage of materials. Considering the hold-time fatigue, during the hold-time at maximum loading, the material in front of the crack tip is damaged by the diffusion of oxygen and creep, and the resistance against cracking is lowered. During the next unloading and loading, the crack will pass through the damage zone and result in

further crack growth. Then the cycle repeats again. This kind of crack growth is obviously time-dependent. The size of damage zone represents the resistance of materials against the crack growth. Therefore, the concept of **Damage Zone** is defined as: *the area in front of the crack tip, where the material is damaged by the environmental factors and the resistance of material on crack growth is lower than a criterion which can prevent the crack growth during the loading cycle.*

4.1.2 Experimental setup

In the past years, West Virginia University has developed a mechanical testing system completely controlled by personal computer for measuring various mechanical properties of materials. The whole system consists of three sub-systems including mechanical loading system, crack monitor system and furnace system. These sub-systems provide the following capabilities:

- Perform tension, compression, fatigue, fracture mechanics, as well as other standard tests;
- Monitor crack propagation;
- Reach to high temperatures with fast heating and cooling response.

Currently, the software package developed has six testing capabilities: tensile, compression, fracture toughness, fatigue/creep crack growth, quench cracking, and heat treatment. The constant ΔK controlled fatigue crack growth can be carried out, and stable crack growth rate can be obtained.

Figure 4 shows the flow chart of the crack monitor system and the controlling analog to maintain constant ΔK during the testing. The components used in crack monitor system includes HP 6033A Power Supply, HP 34401 Multimeter and Personal Computer (PC) with AT-GPIB TNT interface. HP 6033A power supply is used to provide constant current through the testing specimen. When the crack length of the specimen extends, the resistance of the specimen increases and thus the potential drop across the crack also increases. The changes in potential drop will be detected by HP 34401 Multimeter. The results are transferred to PC through AT-GPIB TNT interface. PC then calculates the new crack length based on Johnson's equation:

where A and A_0 represented the actual and initial crack lengths, respectively; U and U_0 were

$$A = \frac{2W}{\pi} \times \cos^{-1} \left[\frac{\cosh(\pi Y / 2W)}{\cosh\{(U/U_0) \cosh^{-1}[\cosh(\pi Y / 2W) / \cos(\pi A_0 / 2W)]\}} \right] \quad (2)$$

updated and initial measured potential drops, respectively; W and Y represented the specimen width and one half of the potential probe span respectively.

The major purpose of the crack monitor system is to provide the capability of controlling the stress intensity level K , which is required for all kinds of crack propagation tests. After recognizing any crack propagation, PC evaluates the load level based on the requested K level and new crack length using Tada's empirical equation:

$$K = \frac{P}{B\sqrt{W}} \times \frac{\sqrt{2 \tan \theta}}{\cos \theta} \left[0.752 + 2.02 \left(\frac{a}{W} \right) + 0.37(1 - \sin \theta)^3 \right] \quad (3)$$

where P represents the applied load, B is the thickness, W is the width, a is the crack length, and $\theta = (\pi a)/2W$. The specimen other than SEN (Single Edge Notch) may need other formula to calculate the load. After comparing with the load level measured from the load cell, PC sends out proper analog signal (0-10V) to DC Force Controller through AT-MIO-16E-10 interface to adjust the load applied to the specimen. Consequently, the constant K controlling is attained.

The fatigue crack growths of superalloys at room temperature and relatively lower temperatures are cycle dependent. Testing parameters, such as cycle period and waveform, play a negligible role in determining how fast the crack will grow for a fixed ΔK . However, as the temperature increases higher than 500°C, superalloys start to show a time-dependent component of fatigue crack growth. The formation of the damage zone (will be illustrated in detail later) in front of crack tip is the key to understanding the time-dependent fatigue crack growth behavior in air. The zone is a weakened area caused by the combination of mechanical and environmental effects.

Let us consider hold-time fatigue cycles applying in a crack in air. During the hold time, the crack may or may not grow depending on the incubation period at the test temperature. Nevertheless a damage zone is built up in front of the crack tip. After the hold time, the crack receives the subsequent cyclic stress intensity (unloading and then loading). A substantial crack increment results from fast crack growth in the damaged zone. The physical process of crack

growth under time-dependent conditions includes damage zone build up, accelerated cyclic crack growth, and sustained loading crack growth. However, the damage zone is too small to be clearly observed in the common fatigue tests.

To investigate the maximum damage zone of the materials during the sustained loading, one particular test procedure is designed in this research. Figure 4 shows the sketch map of such a testing procedure. The SEN specimens were pre-cracked at room temperature with a lower stress intensity triangle cycles up to at least 0.1 inch. The pre-cracked specimens were then heated to the testing temperature and loaded by the constant stress intensity K sustained loading. After a sufficient period of sustained loading, the specimen was cooled to room temperature. Fatigue test was conducted with the frequency of 1/6 Hz, and the K_{max} was kept the same as that of sustained loading. The damage zone size was obtained within this test by measuring the distance to reach the steady fatigue crack growth rate.

4.1.3 Incubation time and damage zone size

Figure 5 shows the typical crack growth behavior of IN718 during various loading stages. It is clear that both pre-cracking and sustained loading have incubation times before reaching steady crack growth. The steady crack growth rates under given stress intensity factors are determined by linear regression analysis. It is sufficient to use linear elastic approximation (or under small-scale yielding condition) to characterize crack propagation behaviors of superalloys studied here.

The existence of a damage zone in front of the crack tip was confirmed by the figure (c), Damage Access stage. The crack growth rate, which is the first derivation of the curve, was remarkably different for each point of the curve. Comparing with the final crack growth rate (Figure 6), the crack grew much faster in the material closer to the crack tip during sustained loading. The da/dN within Damage Zone decreases linearly with the crack length. That means the material in front of the crack tip was badly damaged during the Sustained Loading. However, it is clear that the damage is localized and the material outside the damage zone is not damaged. The crack growth stopped during the last cycles of Damage Access. The size of Damage Zone formed during Sustained Loading can be easily measured in Figure (c).

Figure 7 shows the incubation times and the sizes of damage zone measured at 650°C in different alloys. The incubation times of IN718 and IN706 are shorter than those of U720 and Waspaloy, while the damage zone sizes of IN718 and IN706 are larger than those of U720 and

Waspaloy. Crack growth behavior under time-dependent conditions can be treated as a process of damage accumulation. There is a critical level of damage below that the crack can not grow under static (sustained) loading. The loading in incubation time is just the accumulation of damage, which is the combination of mechanical and environmental effects.

As pointed out by Spedial, any differences in da/dN observed for materials operated under cycle-dependent conditions (room temperature or in vacuum environment) can be effectively explained by differences in elastic modulus. Normalizing ΔK with the elastic modulus can unify fatigue crack growth rates measured for a wide variety of alloy systems. The difference of the resistance to fatigue cracking in air is mainly caused by the different potential against the environmental effect, i.e., oxygen embrittlement by air under loading. Our results conclude that U720 and Waspaloy have better resistance to stress assisted oxygen embrittlement than IN706 and IN718.

4.1.4 Temperature effect on the damage zone size

The formation of the damage zone in front of crack tip is the key to understanding the time-dependent cracking behavior in air. The necessary requirements to form a damage zone include temperature, time, stress intensity and environment. Consider hold-time fatigue cycles (such as 3+177S) applying in a crack in air. During the hold time, the crack may or may not grow depending on the incubation period at the test temperature. Nevertheless a damage zone is built up in front of the crack tip. The formation of damage zone is at a speed equivalent to the sustained loading crack growth rate as the steady crack growth is attained. After the hold time, the crack receives the subsequent cyclic stress intensity (unloading and then loading). A substantial crack increment results from fast crack growth in the damaged zone. The physical process of crack growth under time-dependent conditions includes damage zone build up, accelerated cyclic crack growth, and sustained loading crack growth.

Figure 8 shows the temperature effect on the damage zone sizes of the superalloys after sufficient sustained loading. The stress intensity factor for sustained loading is fixed at 34.5 MPa \sqrt{m} for all temperatures. At 538°C, no sustained loading crack growth or damage zone is detectable in U720 and Waspaloy. In contrast, steady crack growth appears in IN718 and IN706. Damage zones of all the four superalloys increase with temperature. The size of damage zone measured in Waspaloy and U720 is always smaller than that of IN718 and IN706 at all temperatures.

4.1.4 Effect of Microstructure on the damage zone size - In783

IN783 samples with four different treatments were examined by optical microscope for grain morphology and scanning electron micrography (SEM) for β phase. Figure 9 shows the grain structures of IN783 after four different heat treatments. Solution annealing at 1120°C was applied on all samples, equaxed grain structure was resulted with similar grain size of ASTM 7.5- 8.0. Some precipitates remain after solution annealing, which distribute along the flow lines in rolling direction. The addition of chromium (H) seem not affect grain size.

The precipitation of NiAl- β phase is believed to play an essential role on many mechanical properties of IN783. Figure 10 shows SEM observation of β particles after four heat treatments. In general, the nucleation of β phase in Ni fcc matrix is heterogeneous. A few coarse β particles disperse randomly in the matrix after solution annealing, as seen in Fig. 10(c). After the β aging at 843°C/4 hrs, plate-like β particles favorably precipitate along grain boundaries. The Cr addition or over-exposure heat treatment has little effect on the morphology of β phases.

(1) Sustained load crack growth process

Figure 11 displays the testing results for specimen without the β phase treatment. As shown in Figure 2, the crack length remains unchanged for about 200 seconds after applying a static K_{max} . It takes about 560 seconds to reach a steady crack growth rate, da/dt . The intersection between the steady crack growth stage and no crack growth stage is defined as the incubation time, t_i , after which sustained load crack grows linearly. The sustained load crack growth rate, da/dt , can be simply calculated by linear regression of the steady crack growth portion.

The sustained load crack propagation is a thermal activation process associated with the applied load and temperature. Before reaching a steady sustained load crack growth, there is a period of time wherein the crack keeps unchanged. This period is defined as the incubation time corresponding to the accumulation process of oxygen diffusion into materials and the interaction between oxygen and materials. As long as this accumulation reaches a critical status, the crack will initiate and then propagate. In other words, the damage zone caused by environment is established during this accumulation process. The accomplishment of the critical or saturation damage zone will cause crack to grow. Therefore, the incubation period is also associated with the thermal activation process. Figure 12 plots the relationship between incubation time and

temperature. These measured results reconfirm that incubation period and crack growth process under sustained load condition is indeed a result of thermal embrittlement process due to oxygen diffusion ahead of crack tip.

(2) Damage Zone Assessment

Figure 13 plots the damage zone size as a function of holding time period. Three lines parallel each other, so a thermal activation equation was adopted to correlate with the damage zone size(x) and temperature (T)

$$x = A \cdot t \cdot \exp\left(\frac{-Q}{RT}\right) \quad (4)$$

where A is a constant, t is holding period, and Q is thermal activation energy. Figure 9 gives Q a value of 239 KJ/mole.

Figure 14 compares the sustained load crack growth rate (da/dt) and the damage zone propagation rate (dx/dt). As exhibited in Figure 14 two sets of data, da/dt and dx/dt, are comparable considering experimental error.

In summary, alloy 783 without β phase H.T. displays SAGBO sensitivity which allows the fatigue crack to grow in an accelerated rate under hold time fatigue load as well as sustained load crack to grow linearly in thermal activation rate-controlled process. The crack growth is associated with the formation and propagation of damage zone controlled by the thermodynamic oxygen embrittlement.

Over-aged alloy 783 also displays a steady sustained load crack growth. Figure 15 compares the sustained load crack growth rate over aged alloy 783 at different temperature with that of alloy 783 subjected to no β phase treatment. Relative to alloy 783 without β phase treatment, the over-aged alloy 783 displays a comparable sustained crack growth rate and incubation period at different temperatures.

Interestingly, alloy 783 with β phase aging has not demonstrated a significantly detectable crack growth for over 100 hours under sustained load condition at elevated temperature. The crack length is almost unchanged for over 100 hours, although there was very slight change in crack

length at test beginning and after 3000 minutes. This phenomenon, defined as the crack retardation or crack arrest here, also took place at 538°C under sustained load condition.

4.2 Time Dependent Fatigue Crack Growth

4.2.1 Holding-time fatigue test

The SEN specimens were tested in a closed-loop servo-hydraulic MTS 8100 system, and the testing procedure was controlled and recorded by PC software, which was developed by West Virginia University. The specimen was pre-cracked up to at least 0.1 inch by triangle cycles with low stress intensity at room temperature. Fatigue cracking tests were then carried out at elevated temperatures using constant alternating stress intensity factor ΔK with different loading waveforms. The testing sequence was firstly the triangle cycles of 0.333 Hz (3S), and then the trapezoid waveform with 10 seconds holding at maximum stress intensity (3+10S); followed by another triangle cycles of 0.333Hz, and at last the trapezoid waveform with 30 seconds holding at maximum stress intensity (3+30S). For each stage, the crack grew up to 0.05 inch to reach the steady crack growth rate. Finally the specimen was broken up for the calibration of the crack length, and the steady crack growth rates for every stage were obtained. The testing procedure is sketched in Figure 16.

4.2.2 Effects of Alloy Chemistry - IN706, IN718, U720 & Waspaloy

Figure 17 shows the fatigue crack growth rates of the superalloys as a function of holding time at maximum stress intensity. As expected, all of the alloys have similar growth rates under the triangle cycles with three-second period. The crack growth rates under waveforms 3+10S and 3+30S show remarkable increases reflecting the time-dependence nature. The measured crack growth rates increase with holding time. While Waspaloy and U720 show a mild increase of crack growth rate, IN718 exhibits a significant change of da/dN under the conditions of trapezoid waveform with 10 and 30 seconds holding at max stress intensity.

Scanning electron fractography of the fracture surfaces of IN718 for different testing conditions are shown in Figure 18. It is clear that the failure mode of pre-crack at room temperature is transgranular and ductile with small area of quasi-cleavage. Some fatigue striations can be found on the surfaces. The rough surface indicates a high-energy mode of failure with no secondary cracking. The fracture mode of fatigue at 650°C is almost totally intergranular with obvious secondary crack, regardless the difference of holding time. Since it has been indicated that the

fatigue fracture mode of IN718 in vacuum is ductile transgranular, the intergranular mode in air should be contributed as the result of oxygen embrittlement. It is seen from Figure 11(c) that there is a clear boundary between pre-crack at room temperature and fatigue at 650°C.

The pre-crack fracture mode of U720 at room temperature is similar as that of IN718, i.e., transgranular and ductile with a little area of quasi-cleavage. However, as shown in Figure 19, the fatigue fracture mode of U720 at 650°C is different from IN718. Both of the surfaces of fatigue at 3 seconds and 3+30 seconds show the mixture of transgranular and intergranular failure modes. The proportion of intergranular mode increases as the extension of holding time. There are a number of particles on the fracture surface, which are believed to be the primary γ' precipitates in U720.

It is shown in Figure 17 that the fatigue crack growth rates of alloys tested at 3S are almost the same in spite of the difference of the alloy chemistry. Comparing with 3+10S and 3+30S waveforms, 3S triangle cycles seems to be cycle-dependent rather than time-dependent. The oxygen diffusion and oxygen embrittlement along grain boundaries do not play a dominant role during growth. Consequently, the crack growth rates for these four superalloys are similar each other. As the holding time is imposed, different crack growth rates were measured in different alloys. Waspaloy and U720 show better resistance to fatigue cracking under such a time dependent condition.

Comparing with IN718 and IN706, both U720 and Waspaloy contain about a high level of Co (13-14%) but no Fe. It has been proposed that Co is beneficial to temperature stability and oxidation resistance of superalloys, and Fe shows the contrary effect. That is why most of the high temperature superalloys contain some Co and without Fe.

It has been demonstrated that the segregation and enrichment of niobium at grain boundary surfaces is also responsible for the environmental enhancement of crack growth in IN718. The oxidation of niobium and rupture of a brittle niobium oxide (Nb_2O_5 -type) film on the boundary surfaces reduces the alloy's crack growth resistance.

4.2.3 Effect of Temperature

Figure 20 shows the FCGRs of Waspaloy at 650°C and 705°C under various loading conditions. It is found that the FCGRs increase as of holding-time at both temperatures. Temperature plays more important role on FCGR than stress intensity factor. Comparing the results at 705°C with that at 650°C, the temperature was increased about 10% and the stress intensity factor was reduced about 40%. The FCGRs at 705°C are still much higher than that at 650°C.

4.2.4 Effects of Microstructures - IN783

Fatigue crack growth behavior (sample S) under constant ΔK at 650°C is illustrated in Figure 21. As the cyclic stress intensity factor ΔK was kept constant during test, the crack would propagate at a constant rate for a given waveform. The slope of the linear portion represents the steady crack growth, and the crack growth rate can be determined by linear regression analysis. Time dependence of fatigue crack growth is obvious at 650°C. The crack growth rate under a waveform of 100 seconds hold time is dramatically increased to be five times (5X) faster than that of triangular 3S cycles. With increase in hold time, the crack growth rate tends to increase more.

In addition to hold time, temperature also plays a major role on fatigue crack growth behavior. Figure 22 summarizes all results of IN783 with different microstructures through four heat treatments. Two temperatures, 538°C and 650°C, coupled with three waveforms, 3S, 3+100S, and 3+300S, were used. At 650°C, all specimens display full time-dependent fatigue crack growth, i.e. the crack growth rate is proportionally increased with the period of fatigue waveform. At 538°C, the time-dependence of crack growth rate does not start until the hold time is longer than 100 seconds. Raising temperature would not only accelerate the crack growth rate under the time-dependent condition, but also trigger the hold time effects occurring with waveforms of shorter period.

Direct comparison of microstructural effects on the hold-time crack growth in IN783 is plotted in Figure 23. Formation of β phase plays a very important role in improvement of crack growth resistance. Without the heat treatment of β aging, IN783 shows dramatic increase in fatigue crack growth rate, especially under the waveforms with long hold time. Over exposure at 500°C

for 3000 hours also cause higher crack growth rate. It is believed that the β precipitates along grain boundaries may undergo phase transformation.

The addition of 3% Cr appears not to have significant impact on hold-time fatigue crack growth, provided that the alloy receives the same heat treatments including β aging. The crack growth rates at both 538°C and 650°C remain the same in both standard and Cr-added alloys. The beneficial effects of β precipitates along grain boundaries may surpass the Cr addition.

4.2.5 Full time-dependent Fatigue Crack Identification

In order to identify full time-dependent fatigue crack growth behavior, the sustained load crack growth rate was employed to relate with the fatigue crack growth rate. Figure 24 gives an example concerning how to identify the full time-dependent FCP. In Figure 24, static crack growth rate (da/dt) converted from fatigue crack growth rate (da/dn) by multiplying the frequency of a fatigue cycle is plotted as a function of fatigue period, where t_{∞} represents sustained load crack growth. The fact that the static crack growth rate (da/dt) of alloy 783 without β phase H.T. keeps a constant value under various hold time period suggests the crack grows in the full time dependent mode. Since there exists a steady sustained loading crack growth for over aged alloy 783, FCP of over-aged alloy 783 displays the full time-dependent mode. However, the crack growth of alloy 783 with β phase H.T. appears to be retarded, i.e. no detectable crack length available for testing system, when introducing a 1000s hold time fatigue load and sustained load. Also, these crack retardation phenomenon takes place at lower temperature (538°C) under sustained load condition. The crack growth of alloy 783 with β aging demonstrates an abnormal time-dependent mode, which also occurred in high Cr alloy 783.

On the basis of the results above, it is evident that the existence of β precipitates plays a very important role in affecting SAGBO-induced crack growth of alloy 783. The absence of β phase aging in alloy 783 causes an accelerated fatigue crack growth under hold time fatigue condition at elevated temperature, and further increasing the period of hold time results in crack propagation in a full time-dependent mode which is governed by a thermal activation process. The steady sustained load crack growth rate can be employed to relate with the time dependent crack growth rate. In contrast, the presence of β phase aging in alloy 783 introduces the

abnormal time-dependent fatigue crack propagation during a certain period of hold time, further increasing the length of hold time period causes the crack retardation. This observation suggests that the crack growth resistance can be improved dramatically through an introduction of the precipitation of β phase in alloy 783.

Full time-dependent FCP model

Since the damage zone propagation rate (dx/dt) is equal to the sustained loading crack growth rate (da/dt) as well as da/dt is kept constant under full-time dependent condition. A relationship relating the full time dependent fatigue crack growth rate (da/dn) with the thermal activation equation can be derived as follows.

$$\begin{aligned} \therefore x &= A \cdot t \cdot \exp\left(\frac{-Q}{RT}\right) \\ \text{and } \frac{da}{dt} &= \frac{dx}{dt} \\ \text{fatigue crack growth rate can be written as} \\ \frac{da}{dt} &= \frac{1}{t} \cdot \frac{da}{dn} \\ \text{and } \frac{da}{dt} &= A \cdot e^{\left(\frac{-Q}{RT}\right)} \\ \therefore \frac{da}{dn} &= A \cdot t \cdot e^{\left(\frac{-Q}{RT}\right)} \\ \text{so } \ln\left(\frac{da}{dn}\right) &= \ln(t) - \frac{Q}{RT} + \ln(A) \\ \text{let } \alpha(t, T) &= \ln(t) - \frac{Q}{RT} \\ \text{and } C &= \ln(A) \end{aligned}$$

therefore, the fatigue crack growth rate

$$\ln\left(\frac{da}{dn}\right) = \alpha(t, T) + C \quad (5)$$

where $\alpha(t,T)$ is termed as time-dependent factor which is a function of hold time period of fatigue cycle and absolute temperature under constant stress intensity factor (K) condition, C is a constant if K keeps constant, Q is the value thermal activation which can be determined by measuring the sustained load crack growth rate at different temperature. Indeed the time-dependent factor can acts as a universal index to associate with fatigue crack growth rate at different temperatures and frequencies.

Based on equation (5), Figure 25 re-plots the measured fatigue crack growth rate of no β aged alloy against the time-dependent factor, $\alpha(t,T)$. As exhibited in Figure 25, all data fall on one curve that consists of two straight lines. The horizontal line with a constant crack growth rate, termed as $(da/dn)_c$ represents the cycle-dependent domain. Cyclic stress intensity, ΔK , is the governed parameter, and Paris Law can describe the cycle-dependent fatigue crack propagation (FCP) behavior as seen in equation (3). The other line obtained from sustained load crack growth rate displays the time-dependent domain, wherein static stress intensity K_{max} , determines the crack growth rate. Equation (5) can describe the time-dependent FCP behavior.

The empirical expression of time-dependent fatigue crack growth of alloy 783 without β phase treatment can be obtained simply by linear regression of time-dependent domain in Figure 25 as indicated in equation (5) by which the time-dependent fatigue crack growth rate can be calculated.

For no β aged alloy 783:

$$\ln\left(\frac{da}{dn}\right) = \alpha(t, T) + 24.82 \quad (6)$$

Equation (5) and Figure 25 provide a simple and direct approach to describe the fatigue crack growth behavior of alloy 783 at elevated temperature. Note that since the time-dependent fatigue crack growth behavior is sensitive to the variations in microstructure as discussed before, alloy 783 with different microstructure, e.g. the presence of β phase or variation of grain size, would have its own characteristic curve similar to Figure 25.

In summary the two fatigue crack propagation (FCP) regions of alloy 783 subjected to no β phase treatment, i.e., cycle-dependent and time dependent domains, are governed by different driving forces for crack growth. The former is purely the mechanical loading in cyclic form as a driving force, and the crack propagates by transgranular fracture mode. The latter consists of the thermal activation induced air embrittlement under static stress intensity. The brittle intergranular fracture mode always appears in the time-dependent domain.

4.3 Beneficial Effect of Creep on Hold-time FCG of Waspaloy

As previously mentioned, creep and environmental effect happened at the same time during the hold-time FCG test in air, it is difficult to distinguish them between each other. Moreover, some new research results show that there is no increase in FCGR of some alloys with increasing of hold-time, if the tests were done at higher temperature ($\geq 700^{\circ}\text{C}$). The purpose of this chapter is to investigate the creep effect on the hold-time FCG behavior of Waspaloy at elevated temperature.

Waspaloy was selected in the research because it shows better resistance to the hold-time FCG than other superalloys, such as Inconel 718, Inconel 706 and Udimet 720. FCG tests were performed with different hold-time at 760°C under both constant K and constant load control. Fractographical analyses were conducted by means of SEM.

4.3.1 Hold-time Effect on FCG behaviors of Waspaloy under 760°C

The results of FCG tests under constant K control is shown as Figure 26. The tests were carried out under constant K control. It is interesting that under 760°C , the FCGRs for 3+100S are lower than that for 3S at lower K. When K_{\max} was increased to $32.5 \text{ MPa}\cdot\text{m}^{1/2}$, the FCGR of 3+100S became higher than that of 3S. The results at 760°C show that under lower ΔK condition, the hold-time plays a beneficial role, instead of harmful one, in the FCG behavior of Waspaloy. If the stress intensity factor is higher than a critical value, the hold-time shows its harmful effect.

FCG results under constant load show similar trend with the ones under constant K control. As shown in Figure 27, at the beginning of the tests, K value was relatively low, and FCGRs of the specimen under hold-time fatigue condition were lower than that of the specimen under "pure" fatigue condition. As K increases, FCGRs with hold-time become closer to that without holding time. Finally, the FCGRs with hold-time are higher than that without holding.

$$\left(\frac{da}{dn}\right)_{3S} = (5.24 \times 10^{-10}) \times (\Delta K)^{2.45} \quad (7a)$$

$$\left(\frac{da}{dn}\right)_{3+100S} = (2.24 \times 10^{-12}) \times (\Delta K)^{3.82} \quad (7b)$$

Eq. (7a) and (7b) are the regression of the 3S and 3+100S results. Comparing with the result without hold-time, hold-time increases the exponent but reduces the constant in Paris law. The

other effect of hold-time is the offset of stage III FCG. Stage III of the hold-time FCG appears earlier than that of "pure" fatigue.

Figure 28 shows the SEM pictures of fracture surfaces of the specimens after constant load control FCG tests at 760°C. Both of the pictures were taken at the positions in steady state FCG. It is clear that the dominant fracture mode of the specimen under 3S loading is intragranular, while the one under 3+100S loading is intergranular. The Secondary crack can be found at both of the specimens.

4.3.2 Effect of creep

During the hold-time FCG test, the creep behavior of the specimen is not homogeneous because of the stress concentration in front of the crack tip. Generally speaking, creep can affect the FCG behavior through three ways: stress relaxation, microstructure change and creep crack growth.

Riedel *etc.* analyzed the creep behavior in front of the crack tip. If a load is applied and then held constant, a creep zone gradually develops in plastic zone. They argued that the stresses' well within the creep zone could be described by:

$$\sigma_y = \left(\frac{C(t)}{A I_n r} \right)^{\frac{1}{n+1}} \hat{\sigma}_y(n, \theta) \quad (8)$$

where n is the exponent in the creep equation, A , I_n are numerical constants, $\hat{\sigma}_y(n, \theta)$ is a variable as a function of n and θ , r is the distance from the crack tip. $C(t)$ is a parameter that characterizes the amplitude of the local stress singularity in the creep zone.

$$C(t) = \frac{K_I^2 (1-\nu)^2}{(n+1)Et} \quad (9)$$

where K_I is the first mode stress intensity factor, ν is the Poisson ration, E is the Young's modulus and t is hold-time. $C(t)$ varies with time and is equal to C^* in the limit of long time behavior. If the remote load is fixed, the stresses in the creep zone relax with time, as creep strain accumulates in the crack tip region. The "effective" stress was lowered by stress relaxation during hold time. Creep plays a beneficial role on FCG by stress relaxation.

The microstructure of the material in front of the crack tip is changed during the hold-time. The principal deformation processes during creep are slip, sub-grain formation and grain-boundary sliding. The dislocation structure of the material is changed during creep, at the same time dynamic recovery and recrystallization occur. However, the investigations of the structural changes during creep and their effect of FCG behavior are still ongoing and not included in this paper.

During stage III, the accumulated creep damages leads to the cavity nucleation and growth at the grain boundaries, then causes the creep crack growth. The creep crack growth would accelerate the FCG of the alloy. Figure 29 shows the 3+100S crack growth behaviors of the specimen under various stages. The dc electric potential (EP) drop technique was employed to monitor crack length during the test and EP voltage represents the crack length. It is obvious that during the steady state FCG, the crack length keeps constant during the hold-time, if neglect the vibration of read-out. On the contrary, there is a small jump of the crack during the hold-time, if it is in stage III. Creep does not play beneficial role on FCG any more.

4.4 In-situ Crack Tip Deformation

The objective of this research is to determine the mechanism of the Stress Accelerated Grain Boundary Oxidation (SAGBO) embrittlement of INCONEL 783. Crack growth tests were conducted on IN 783, three-point-bend specimens in air and controlled oxygen atmosphere at a temperature of 538 °C and 650 °C on two types of specimens, with and without β -phase. A total of six experiments were conducted, three of them corresponding to three specimens with β -phase, and three specimens without β -phase, respectively. Two types of loading were applied, constant displacement (fixed-grip) and constant load.

High Temperature Moiré Interferometry (HTMI) was used to determine full-field displacements of fatigue pre-cracked single edge notched specimens under sustained loading and various controlled oxygen-content environments. Based on the full-field crack tip moiré fringes, stress intensity factor, crack growth rates and crack tip plastic yield zone size and shape estimations were evaluated.

4.4.1 Experimental setup

Figure 30 shows the typical three-point-bend specimen dimensions. Specimens were fatigue pre-cracked to provide a starting nominal pre-cracked plus notch length of approximately 4 mm.

At the beginning of this research task, concerted effort was dedicated to the completion and improvement of the controlled-environmental high temperature materials testing apparatus, as shown in Figure 31. Main components of the testing equipment are consisted of:

- (1) UHV Chamber. The chamber access ports accommodate a variety of experimental devices, analytical instruments, viewports and feedthroughs. Ion pump, turbomolecular pump and mechanical pump are attached to the UHV chamber.
- (2) Specimen Holder. This is the core part of the UHV test apparatus which was designed to assure high precision, easy specimen installation, efficient attachment of heating system, easy maneuverability, and maximum protection against electrical shocks. The specimen holder was designed for three-point-bend specimens. The heating system consists of a 1000 W quartz and a reflector attached to the specimen holder. The system proved to be very efficient and the specimen can be easily heated up to 650 °C. The maximum attainable temperature, in vacuum condition, can be up to 1000°C

- (3) Loading Frame. It is for constant loading condition. A special adapter was designed to accommodate a Sensotec loadcell in between the loading frame and the vacuum chamber. The loadcell was calibrated before each test. The loading frame can also be used with satisfactory results, as a “constant displacement” type of loading.
- (4) Cooling System. The UHV chamber is wrapped with water-cooled copper tubes, as shown in Figure 31. Fine control of the water flow is necessary to minimize system vibration.
- (5) Sensors. Chamber pressure is monitored through Pirani and cold cathode tubes pressure gauges. There are leak valves with gas cylinders attached for fine controlling of the gas flow (argon and oxygen) to the chamber. A thermocouple is attached to the specimen holder to monitor the temperature. A gate valve serve to protect the glass viewing port against heat radiation. A residual gas analyzer (RGA) is attached to the UHV chamber for monitoring the chemical composition of the gases inside the environmental chamber before, during and after the experiments.

Optical Setup. Full field crack-tip displacements are measured using High Temperature Moiré Interferometry (HTMI). The images were captured using a CCD camera. Figure 32 shows the schematic representation of the optical

4.4.2 Results and Discussions

(1) Thermal expansion

Moiré Interferometry proved to be a useful method in determining the coefficient of thermal expansion of the analyzed specimens. All the tests involved high temperature, and for the accuracy of the results, gradually increasing in small steps of 20-30 °C of the temperature of the specimen correlated with waiting times of 15-20 minutes for each step, ensured uniform thermal expansion and displacements.

To determine the thermal expansion coefficient, either in air or vacuum, the following procedure was used:

- the mirrors were adjusted in the optical setup to get the null displacement field of the fringe pattern.

- the specimens were heated up to 100-120 ° C; at this temperature the thermal expansion introduced a modification in the fringe pattern.
- the temperature was gradually increased, in steps, images of the fringe pattern were captured at each corresponding step. Because the stress induced by the thermal expansion is uniform all over the specimen, without any stress concentrations, a normal fringe pattern is represented by parallel, equidistant fringes.

Figure 33 is an example of the fringe pattern induced by the thermal expansion.

- the thermal strains were determined through

$$\varepsilon_T = 1/f * \Delta x_T \quad (10)$$

where ε_T represents the strain corresponding to temperature T, f is the grating frequency, in our case 1200 lines/mm, Δx_T is the distance between two fringes corresponding to the same temperature T. Thermal expansion coefficient is the slope of the curve, plotting the strain versus temperature. Figure 34 represents the results of the experimental data. These results are in agreement with the data found in the literature. The precision of the method is given by the precision of the scale and dimensions measurement. In this case the precision is in hundredths of mm. The error is $\pm 5\%$.

Test Matrix: A series of six experiments were conducted, for three specimens with β -phase, and three specimens without β -phase, in similar environmental and temperature conditions. The results demonstrate the difference between the two types of specimens, and the importance of the effect that β -phase has on the fracture behavior of the material. The importance of our experiments resides, not only in the combination of air, as a testing environment, with sustained loading, but also vacuum followed by a partial pressure of oxygen as a testing condition, combined with sustained loading.

Table II illustrates the effect of the testing conditions and the presence of the β -phase in the evaluation of the crack growth behavior. Crack growth rate is inversely proportional to volume % β -phase. Our experiments have proven that for sustained load, crack growth is influenced by oxygen from the environment, for the specimens with β -phase, both in air and partial pressure of

oxygen, at temperatures of 538 and 650°C. The presence of intergranular precipitates of β -phase provided increased environmental crack growth resistance.

Crack growth tests were conducted using fatigue pre-cracked three-point-bend specimens. Constant load crack-growth tests were performed at 538°C and 650°C in air using a convection furnace mounted on a loaded creep frame, and in a partial pressure of oxygen, at the same temperatures, using the equipment described before. Crack lengths were measured based on the moiré fringes.

(2) Crack Growth Evaluation. Principal Strains. Effective Stresses

For each type of specimen, with or without β -phase, two types of loading, were applied, constant displacement (fixed grip) and constant loading, in two different types of environments, air and 10^{-6} Torr vacuum, and two different temperatures, 538 and 650°C. Different initial stress intensity factors were applied. The creep crack growth or sustained load crack growth, is a time dependent behavior. Both in air or vacuum the specimens with β -phase didn't reveal any initial crack growth. The specimens without β -phase revealed elastic crack growth in air, both at 538 and 650°C. Usually, a testing procedure using Moiré Interferometry, included the following:

- adjusted the optical alignment, to obtain the initial null field at the room temperature.
- gradually increased the temperature in small steps of 30 – 50 °C, up to the testing temperature, ensuring that the specimen was subjected to a uniform thermal expansion.
- readjusted the fringe pattern to a null-field, at the final testing temperature.
- pictures were captured corresponding to each individual step in applying load and the representative results are shown in Figures 35 to 39.

As seen in Figure 35, the A5 specimen, tested in air, 538 °C, had the same crack length of 1.36 mm for an initial value of stress intensity factor $K_I = 12.52 \text{ Mpa}\sqrt{\text{m}}$ up to a value $K_I = 55.2 \text{ Mpa}\sqrt{\text{m}}$. In Figure 36, crack length of the B5 specimen (without β -phase), tested in air, 538°C, increased from 0.80 mm, corresponding to a value $K_I = 12.48 \text{ Mpa}\sqrt{\text{m}}$ up to 1.46 mm corresponding to a stress intensity factor value $K_I = 35.42 \text{ Mpa}\sqrt{\text{m}}$. At this value, the crack length remained the same. Further increasing of the load led to gradually increasing of the ductile plastic zone. B4 specimen tested in air at 650 °C had the same behavior. In Figure 39, the crack

length have grown from 0.62mm, $K_I = 10.33 \text{ Mpa}\sqrt{\text{m}}$, up to 1.31 mm, corresponding to a stress intensity factor value $K_I = 45.3 \text{ Mpa}\sqrt{\text{m}}$. The crack length remained the same afterward, subsequent load steps increased the size of the ductile failure zone.

Figures 36 and 40 show the principal strain distribution of specimens B5 and B4 respectively. Figure 37 show the effective stress distribution of the specimen B5. The effective stress areas were compared with the theoretical results based on the Linear Elastic Fracture Mechanics to ensure that the nominal behavior, that characterize crack tip conditions, is linear elastic. The programs used to determine the crack-tip principal strain distribution and the crack-tip effective stress distribution are developed by R. Kamil.

One of the tests (B6 specimen) revealed important test results that may be connected to the SAGBO mechanism of the test alloy. The test procedure and the measurement of the crack growth revealed the same conclusion. For the specimens without β -phase the oxygen is responsible for the time-dependent crack growth induced by environmental effects under sustained load. The specimens with β -phase were insensitive to the environmental effect.

Figure 43 represent the chemical composition of the atmosphere in the testing vacuum chamber, after reaching the initial pressure of approximately 10^{-6} Torr. Important for our experiments was, the initial partial pressure of the oxygen, 10^{-8} Torr, representing the pressure at which the specimen B6 was loaded for 40 hours. A ductile type of crack-tip deformation during this testing period in vacuum where the applied loads were increased gradually, up to a value of the stress intensity factor $K_I = 24.73 \text{ Mpa}\sqrt{\text{m}}$. Figure 45 represent the moiré fringe pattern corresponding to the period of constant type of loading, of 40 hours. After this period 40 Torr, pressure of oxygen was introduced to the test chamber as seen in Figure 46. After the incubation time of 2 hours and 57 minutes, a clear elastic crack growth was observed as shown in Figure 46. The length of the elastic crack growth is about 0.07 mm. After 7 hours the crack extension was 0.11 mm. After another 30 min the specimen failed. Figure 4.15 shows the principal strain distribution of the B6 specimen during the testing.

The same procedure was repeated with A4 specimen, as shown in Figure 48. After 26 hours from the starting time of the experiment, a pressure of oxygen was introduced up to 9 Torr. Because there was no modification of the crack length due to oxygen input, the applied load continued to

be increased as seen in Figure 49. The result was just a continuously increasing of the crack-tip plastic zone, and when the load reached approximately 700 lb, the specimen failed.

Figures 41 and 42 represent the testing sequences for specimen B6 and A4 respectively.

4.5 Oxygen Impurities in NiAl: Relaxation Effects.

At intermediate to high temperature, nickel aluminides, and many other intermetallics, exhibit brittle intergranular fracture due to the oxygen-induced embrittlement. At high temperature, the oxidation will selectively attack the least noble constituent, which is aluminum, and form the oxide product Al_2O_3 . In some cases, these oxide products can provide a stable oxide layer that protects the alloy underneath it from further oxygen attack. NiAl is one of the intermetallics that are able to form a protective oxide layer and therefore is used as a coating for other intermetallic alloys. The oxidation resistance decreases as we move toward the nickel-rich part of the Ni-Al phase diagram. The most damaging effect of oxygen occurs when it causes the pesting degradation phenomenon (essentially spontaneous disintegration in air). Some intermetallic compounds that form protective coatings at high temperature literally disintegrate when heated in the intermediate temperature range. This occurs only on polycrystalline samples, so it is sometimes also termed intergranular attack. Among nickel aluminides, the pesting phenomenon has been observed in NiAl, and in Ni_3Al .

Despite the extreme effects that it can cause, we are un-aware of any previous *ab initio* study performed on the effects of oxygen in nickel aluminides. Moreover, most studies of other impurities are limited by not allowing the atoms within the supercell to relax. Relaxation effects are especially relevant to the case of impurity atoms located at the grain boundary where they can be relatively free to move and bond to certain constituent atoms of the host alloy.

4.5.1 Methodology

In this work we have used a full-potential linear muffin-tin orbital method within the local density approximation (LDA) to study the effects of oxygen impurities on the electronic structure of NiAl. The details of this method have been documented elsewhere. For the work reported in this paper, we use nine (*spd*) orbitals for each atom in the supercell and assign three LMTO basis functions for each orbital, corresponding to $k = -1.50$, -0.50 , and 1.00 , respectively. Here k is the wave-number parameter; the square of k is the absolute value of the energy of the basis function, measured relative to the muffin-tin zero, while its sign is equal to the sign of the energy. The large number of basis functions used provides our full-potential method with good flexibility to find the lowest-energy density.

The 16-atom supercell that was used in the computation is shown in Figure 51. Pure NiAl crystallizes in the B2 structure with lattice constant of 5.4450 a.u. The calculated equilibrium lattice constant using our FP-LMTO method is 5.3451 a.u., which agrees with the experimental value within 2%. The supercell is constructed from 2^3 unit cells of NiAl. The oxygen impurity atom is placed at the center of the supercell, replacing a nickel or an aluminum atom. For a given supercell lattice constant, we allow the atoms in the unit cell to relax to find the minimum total energy for that lattice constant. By symmetry, only the eight nearest neighbors of the oxygen atom are allowed to relax, and they can only move radially away or toward the center oxygen atom (we do not consider the possibility of symmetry breaking). Only one parameter is needed to describe the relaxation, namely, the distance of these neighboring atoms from the central oxygen atom.

4.5.2 Results and Discussion

The computed total energies for the relaxed 16-atom supercell are shown in Figure 52 and compared with the curves for the unrelaxed supercell. Each continuous curve shown in Figure 52 is obtained by fitting 8–9 LMTO data points computed around the minimum-energy lattice constant using an eight-parameter fitting function. The calculated relaxation energies E_R are listed in Table II. We use the following definition for the relaxation energy:

$$E_R = E_r(a_r) - E_u(a_u) \quad (11)$$

with a_u and a_r being the lattice constants that give the minimum energy for the unrelaxed (E_u) and relaxed (E_r) configurations, respectively. The computed energy curves lie very close to each other, and the relaxation energies are relatively small, being about 100K and 200K (in equivalent temperature scale) for oxygen at the Al and Ni sites, respectively. These numbers are about the same as the accuracy of the LMTO-LDA method, which has been estimated at about 1 mRy (158K). Numerically, however, our FP-LMTO method did not produce any notable fluctuation and we believe that some confidence can be placed in these numbers.

The computed relaxation data are shown in Figure 53 where we track the nearest-neighbor distances between the atoms in the unit cell on the (011) plane as we change the supercell lattice constant. Figure 53(b) displays the results for the case of oxygen at the Ni site. Shown are $d(\text{Al-O})$, which is the distance between the central O atom and one of its eight nearest-neighbor Al atoms, and $d(\text{Ni-Al})$, which is the distance between the Al atom and its nearest-neighbor Ni atom

(at one of the corners of the supercell). Without relaxation, the oxygen atom will be at (0,0,0), the aluminum atom at, e.g., (1/4, 1/4, 1/4) and the nickel atom at (1/2, 1/2, 1/2). As we vary the lattice constant a , the distances scale linearly with it: $d(\text{Al-O})=d(\text{Ni-Al})=a\sqrt{3}/4$. This relation is still approximately followed when we relax the atoms, as shown in Figure 53, with the aluminum atoms only attracted slightly more toward the central oxygen atom.

A significantly different situation occurs if we place the oxygen atom at the Al site, as shown in Figure 53(a). In this case, the nearest neighbors of the central O atom are Ni atoms, the distance between them is $d(\text{Ni-O})$, and each of these Ni atoms neighbors an Al atom at its nearest corner of the supercell, where the distance between them is denoted by $d(\text{Ni-Al})$. Under pressure, for lattice constants smaller than the equilibrium value, the Ni atoms slightly relax toward the central oxygen atom, away from the corner Al atoms. However, as the lattice constant is increased above the equilibrium value, the intervening Ni atoms very quickly start to move *away* from the central oxygen atom and relax closer to their neighboring Al atoms. We view this as reflecting a mutual repulsion between the oxygen and nickel atoms in the NiAl environment. Experimentally, the formation rate of aluminum oxide during exposure of nickel aluminides to oxygen is known to be much higher than that of nickel oxide.

The relaxation behavior of the atoms is thus seen to differ markedly depending on whether the impurity oxygen atom occupies an Al or a Ni site, especially in the stretched-supercell case, where the atoms have greater freedom to move around. This may have some relevance to the case of oxygen attack on polycrystalline nickel aluminides (pestring). We believe this reflects a situation where the oxygen atoms cause a sort of "wedge effect," seeping into the grain boundaries to reduce the intergranular cohesion and opening up the polycrystal wider for more infiltration of oxygen. This provides a *self-propelling* mechanism for oxygen atoms to infiltrate a polycrystal of nickel aluminide and, along the way, destroy the intergranular cohesion between the grains, effectively disintegrating the polycrystal. In this scenario the pestring phenomenon can be seen to be fueled by the *combination* of two major factors: the thermal intergranular diffusion of oxygen and the strongly *preferential* bonding of oxygen with one of the components of the alloy (aluminum in nickel aluminides). More insights into this phenomenon can perhaps be obtained by performing a molecular-dynamics (MD) simulation using microscopic parameters

that are extracted from an *ab initio* calculation such as reported in this paper. Campbell *et al.* have performed such a MD simulation for the oxidation of aluminum nanoclusters.

The energetics of the preferential bonding of oxygen in NiAl can be studied by calculating the site selection energy. The total energy for pure bulk metal (per atom) is used to provide a reference energy for the constituent species. In our case, these are the total energies of fcc Ni and fcc Al. These have been calculated using the same FP-LMTO method and their values are

$$E(\text{Ni}) = -3036.8304 \text{ Ry}, \quad (12)$$

$$E(\text{Al}) = -2483.8440 \text{ Ry}. \quad (13)$$

The total energies for the 16-atom supercell with one oxygen atom replacing a Ni or an Al atom are listed in Table III. We list the minimum of the total energy of the relaxed supercell. The site selection energy is defined to be the difference between the following two values:

$$E_{\text{Ni}} = E(\text{Ni}) + E(\text{Ni}_7\text{Al}_8\text{O}) = -28\,315.7204 \text{ Ry}, \quad (14)$$

$$E_{\text{Al}} = E(\text{Al}) + E(\text{Ni}_8\text{Al}_7\text{O}) = -28\,315.5827 \text{ Ry}. \quad (15)$$

Taking the difference, an oxygen atom in NiAl will prefer to occupy a nickel site with the site selection energy of

$$\Delta E = 137.7 \text{ mRy} = 21\,730 \text{ K}. \quad (16)$$

That oxygen will prefer to occupy a nickel site over an aluminum site seems to contradict one's expectation based on the atomic radii of the constituent atoms. Since the atomic radius of oxygen is closer to that of aluminum rather than nickel, one would expect that the oxygen would prefer to occupy an aluminum site over the nickel site. To understand our result, we need to recall the previously deduced mutual repulsion between oxygen and nickel in the NiAl environment. An oxygen atom will therefore prefer to be surrounded by nearest neighbors of aluminum, rather than nickel, atoms. It will achieve this simply by occupying a nickel site.

Finally, in Figure 54 we show the total density of states (DOS) for the two supercell systems that we study in this work, $\text{Ni}_8\text{Al}_7\text{O}$ and $\text{Ni}_7\text{Al}_8\text{O}$, calculated from the FP-LMTO energy bands using the tetrahedron method. For comparison, we also show the corresponding total DOS for pure NiAl. The dominant feature of the NiAl DOS is the existence of the sharp peaks due to the *d* orbitals of nickel, which hybridize only weakly with the other orbitals. Placing the oxygen atom

at the Al site in $\text{Ni}_8\text{Al}_7\text{O}$ allows for some hybridization between these d orbitals and the delocalized p orbitals of oxygen. This results in reduced sharpness of the Ni d state peaks in the DOS without essentially any shift in the position of the peaks, as can be seen in Figure 54(a). On the other hand, if we place the oxygen impurity at the Ni site, then the nickel atoms will not have the oxygen atom as their nearest neighbor. The oxygen atom will have the aluminum atoms as its nearest neighbors. Being the more electronegative element, oxygen will interact with the valence electrons of Al and will localize a portion of those electrons around itself. This depletes the Ni sites of some of the electrons from the Al that was formerly occupying its site in the pure NiAl case. The end result of this is a lower electrostatic potential at the Ni sites and the reduction of the on-site energies of the d orbitals of Ni, without much change in their spatial extent. This translates to an almost rigid downward shift in the position of the Ni d state peaks in the DOS without much alteration in their width. This downward shift of about 25 mRy can quite readily be discerned in Figure 54(b).

5. Personnel Supported

This project supports the following professional personnel in Department of Mechanical and Aerospace Engineering (MAE) and in Department of Physics:

Faculty –

<i>Keh-Minn Chang</i>	Professor, Mechanical and Aerospace Engineering.
<i>Bruce Kang</i>	Associate Professor, Mechanical and Aerospace Engineering.
<i>Bernard R. Cooper</i>	Benedum Professor, Physics

Postdoctoral –

<i>Xingbo Liu</i>	Mechanical and Aerospace Engineering.
<i>Jian Mao</i>	Mechanical and Aerospace Engineering.
<i>David Djajaputra</i>	Physics

Graduate Research Assistant –

<i>Longzhou Ma</i>	Ph.D. student, Mechanical and Aerospace Engineering.
<i>Matthew Burris</i>	M.S. student, Mechanical and Aerospace Engineering.
<i>Cezar Cislou</i>	M.S. student, Mechanical and Aerospace Engineering.
<i>Roxana Cislou</i>	M.S. student, Mechanical and Aerospace Engineering.

6. Publications

1. D. Djajaputra and B.R. Cooper, "Hydrogen Atom in a Spherical Well: Linear Approximation" *European Journal of Physics*, 21 (2000) 261.
2. D. Djajaputra and B.R. Cooper, "Oxygen Impurities in NiAl: Relaxation Effects" *Physical Review B*, 64 (2001) 085121.
3. J. Mao, V. Keefer, K.-M. Chang and D. Furrer, "An Investigation on Quench Cracking Behavior of Superalloy Udimet 720Li" *Journal of Materials Engineering and Performance*, 9 (2000) 204.
4. W. Yang, W. Chen, K.-M. Chang, S. Mannan, and J. deBarbadillo, "Monte Carlo Sampling for the Microsegregation Measurements in Cast Structures," *Metall. Mater. Trans., A*, 31A (2000) 2569.
5. K.-M. Chang, and X. Liu "Effects of γ' Content on the Mechanical Behavior of Waspaloy Alloy System," *Materials Science and Engineering A*, A308 (2001) 1.
6. W. Yang, W. Chen and K.-M. Chang, "Freckle Criteria for the Upward Directional Solidification of Alloys," *Metall. Mater. Trans., A*, 32A (2001) 397.
7. X. Liu, J. Dong, X. Xie and K.-M. Chang, "The Appearance of Magnesium and Its Effect on Mechanical Properties of Inconel 718 with Low Sulfur Content," *Materials Science and Engineering A*, A303 (2001) 262.
8. J. Mao, K.-M. Chang, W. Yang, K. Ray, S. Vaze and D. Furrer, "Cooling Precipitation and Strengthening Study in Powder Metallurgy Superalloy U720Li", *Met. Mat. Trans. A* (2001) in press.
9. J. Mao, K.-M. Chang, W. Yang, D. Furrer, K. Ray and S. Vaze "Cooling Precipitation and Strengthening Study in Powder Metallurgy Superalloy R88DT", *Mat. Sci. & Eng. A* (2001) in press.

7. Interactions/Transitions

Conference Presentation –

1. W. Chen, W. Yang, K.-M. Chang, S. K. Mannan, and J. J. deBarbadillo, "Solidification Diagram of Ni-Cr-Fe-Nb System," TMS symposium proceedings of Advanced Technology for Superalloy Affordability, ed. K.-M. Chang, etc., March 2000, pp. 93-102.
2. L. Ma, K.-M. Chang, and S.K. Mannan, "The Effects of Heat Treatment on Time-dependent Fatigue Crack Propagation in a Low Thermal Expansion Superalloy INCONEL 783," TMS symposium proceedings of Advanced Technology for Superalloy Affordability, ed. K.-M. Chang, etc., March 2000, pp. 131-140.
3. M.S. Seehra, A. Manivannan, C. Cionca, L. Ma, and K.-M. Chang, "Effects of Heat Treatments and Thermomechanical Processing on the Beta and Gamma Phases in Inconel 783 Alloy," TMS symposium proceedings of Advanced Technology for Superalloy Affordability, ed. K.-M. Chang, etc., March 2000, pp. 141-148.
4. "Effects of Atomic Oxygen on Cohesion in Nickel-rich Metals", Tenth Conference on Computational Research on Materials, Lakeview, WV, May, 2000.
5. "Effects of Vacancies and Oxygen Impurities on Cohesion in Nickel Aluminides" American Physical Society Meeting, Minneapolis, March, 2000.
6. W. Yang, W. Chen, K.-M. Chang, S. Mannan, and J. deBarbadillo, "Segregation and Solid Evolution During the Solidification of Nb-Containing Superalloys", "Superalloys 2000", TMS (2000) 75.
7. J. Mao, K.-M. Chang and D. Furrer, "Quench Cracking Characterization of Superalloys Using Fracture Mechanics Approach", "Superalloys 2000", TMS (2000) 109.
8. L. Ma, K.-M. Chang, S. Mannan and S. Patel, "Effect of Thermomechanical Processing on Fatigue Crack Propagation in Inconel Alloy 783", "Superalloys 2000", TMS (2000) 601.

9. X. Liu, L. Ma & K-M. Chang: " Time-dependent Crack Growth Behaviors of Five Superalloys", "Superalloys 718, 625, 706 and Various Derivatives", TMS (2001) 543.
10. W. Yang, W. Chen, K.-M. Chang, S. Mannan, J. deBarbadillo and K. Morita, "Freckles in Remelted Niobium Containing Superalloys", "Superalloys 718, 625, 706 and Various Derivatives", TMS (2001) 113.
11. Z. Long, W. Yang and K.-M. Chang, "Freckle Formation and Thermodynamic Assessment for Nb-bearing Superalloys", "Superalloys 718, 625, 706 and Various Derivatives", TMS (2001) 745.

Table I. The compositions and heat treatments of test alloys (wt.%)

Alloy	C	Ni	Co	Cr	Fe	W	Mo	Nb	Ti	Al
IN718	0.04	52.5	--	19.0	18.5		3.0	5.1	0.9	0.5
IN706	0.03	41.5	--	16.0	37.5		--	2.9	1.75	0.2
IN783	0.01	28.5	34.0	3.0	26.1		--	3.0	0.1	5.4
U720	0.03	Bal.	14.6	15.6	--	1.25	3.0		5.0	2.5
Waspaloy	0.08	57.0	13.5	19.5	--		4.3	--	3.0	3.0
Heat Treatment										
IN718	980C/1h/AC+720C/8h/FC→620C/8h/AC									
IN706	1800F/1h/AC+1550F/3h/AC+1325F/8h/FC(100F/h)→1150F/8h/AC									
U720	2020F/2h/OQ+1400F/8h/AC+1200F/24h/AC									
Waspaloy	1868F/4h/OQ+1562F/4h/AC+1400F/16h/AC									

<u>Specimen</u>	A4** vacuum 10 ⁻⁶ Torr	A5 air	A6 air	B4 air	B5 air	B6 vacuum 10 ⁻⁶ Torr
Temperature ° C	538	538	650	650	538	538
<u>Loading Type</u> K value*	II K _I =32.63	I K _I =12.52	I K _I =11.25	I K _I =10.33	I K _I =12.48	II K _I =24.73
Initial applied load	P=1545 N	P=578 N	P=554 N	P=542 N	P=694 N	P=1248 N
<u>Results</u>	No crack growth observed	No crack growth observed	No crack growth observed	0.69 mm crack growth	0.66 mm crack growth	No crack growth under vacuum; observed crack growth 170 minutes after introducing 40 Torr of oxygen

* Mpa√m

** After 26 hours, 9 Torr of oxygen was input into the test chamber
see Figures 4.16, 4.17, 4.18 for detailed testing sequence

A: specimens - with β phase
B: specimens - without β phase
I: Constant Displacement (Fixed-Grip) Loading
II: Constant Load

Table II Test Matrix

TABLE III. Equilibrium lattice constant a_r for fully relaxed supercell, its total energy E_r , and the corresponding relaxation energy E_R (relative to the unrelaxed supercell).

Supercell	a_r (a.u.)	E_r (Ry)	E_R (mRy)
$\text{Ni}_8\text{Al}_7\text{O}$	10.5878	-27831.7387	-0.675
$\text{Ni}_7\text{Al}_8\text{O}$	10.6567	-25278.8899	-1.236

List of Figures

Figure 1: Sketch of fatigue crack growth models.

Figure 2: Sketch of the Damage Zone

Figure 3: Sketch map for the computer controlled crack monitoring and constant K controlling system.

Figure 4: The sketch map of the testing procedure.

Figure 5: Typical Crack Growth Behavior of IN718.

Figure 6: Relationship between da/dN and crack length during Damage Access stage.

Figure 7: Incubation times and damage zones of the alloys.

Figure 8: Temperature effect on the damage zone sizes of the alloys.

Figure 9: Grain structures of IN783 under different heat treatments.

Figure 10: SEM micrograph of β phase formation under different heat treatments.

Figure 11: Sustained load crack growth of alloy 783 without β phase aging at $K=38.5\text{MPa}\sqrt{\text{m}}$ and 650°C

Figure 12: Incubation time as a function of temperature in alloy 783 without β aging, at constant $K=38.5\text{MPa}\sqrt{\text{m}}$

Figure 13: Damage zone size against holding time period at $K_{\text{max}}=38.5\text{MPa}\sqrt{\text{m}}$

Figure 14: Comparison of da/dt and dx/dt for no β aging at $K_{\text{max}}=38.5\text{MPa}\sqrt{\text{m}}$

Figure 15: Sustained load crack growth of over aged alloy 783 vs. temperature at $K=38.5\text{MPa}\sqrt{\text{m}}$

Figure 16: The sketch map of the holding-time fatigue crack growth test.

Figure 17: Fatigue crack growth rates of Waspaloy, U720, IN718 and IN706 as function of holding time at maximum stress intensity.

Figure 18: Scanning electron micrographs of IN718 fatigue fracture surfaces.

Figure 19: Scanning electron micrographs of U720 fatigue fracture surfaces.

Figure 20: FCG behavior of Waspaloy at 650°C and 705°C under constant ΔK control.

Figure 21: Crack growth of IN783 at constant $\Delta K=33.5\text{ksi}\sqrt{\text{in}}$.

Figure 22: Fatigue crack growth for IN783 with various treatments.

Figure 23: Fatigue crack growth comparison of IN783 alloys with various treatments.

Figure 24: Fatigue crack growth rates of no β aging normalized by time dependent factor at
 $K=38.5\text{MPa}\sqrt{\text{m}}$

Figure 25: Normalized fatigue crack growth rates of alloy783.

Figure 26: Effect of K on FCGR of Waspaloy at 760°C under 3S and 3+100S loading (constant K control).

Figure 27: Effect of K on FCGR of Waspaloy at 760°C under 3S and 3+100S loading (constant load control).

Figure 28: Fracture surfaces of the specimens after constant load control FCG tests at 760°C.

Figure 29: The FCG behaviors within one cycle during various stages. (760°C, 3+100S)

Figure 30: Specimen Dimensions.

Figure 31: UHV Material Testing System.

Figure 32: Schematic of Moiré Interferometry Set-up.

Figure 33: Comparative fringe pattern induced by thermal expansion.

Figure 34: Comparative thermal expansion data of different specimens in different environmental conditions.

Figure 35: A5 specimen, 538⁰ C, air

Figure 36: B5 Specimen, 538⁰ C, air

Figure 37: Principal Strains Distribution, B5 Specimen, 538°C, air

Figure 38, B5 Specimen, Effective Stresses

Figure 39, B4 Specimen, 650⁰ C, air

Figure 40: B4 specimen, 650⁰ C, air, Principal Strain Distribution

Figure 41: Testing Sequence for B6 Specimen

Figure 42: Testing Sequence for A4 Specimen

Figure 43: Gas Composition in the Testing Chamber, 538°C.

Figure 44, B6 Specimen, 538°C, vacuum 10^{-6} Torr

Figure 45: B6 Specimen, 538°C, vacuum 10^{-6} Torr

Figure 46: B6 specimen, 538°C

Figure 47: B6 specimen, Principal Strain Distribution

Figure 48: A4 specimen, 538°C, vacuum 10^{-6} Torr

Figure 49: A4 specimen, 538°C

Figure 50: A4 specimen, Principal Strains Distribution

Figure 51. The 16-atom supercell used in the present work. The cubic supercell is built up from 2^3 unit cells of NiAl. The impurity atom (O) is placed at the center of the supercell, substituting for Ni in this picture (supercell $\text{Ni}_7\text{Al}_8\text{O}$). We also use a similar supercell, where the oxygen atom is placed at an Al site (supercell $\text{Ni}_8\text{Al}_7\text{O}$).

Figure 52. The FP-LMTO total energy with 16-atom supercell for the case of oxygen substituting for an aluminum atom (a), and oxygen substituting for a nickel atom (b). In both panels, the top curve is for an unrelaxed supercell while the bottom curve is for the relaxed supercell. The equilibrium lattice spacing and the relaxation energy are listed in Table III.

Figure 53. Nearest-neighbor (NN) distances between atoms in the unit cell on the (011) plane as a function of the supercell lattice constant.

Figure 54. Total density of states for the 16-atom supercell calculated using the FP-LMTO method. For comparison, in each panel we also show the negative of the density of states for pure NiAl. Vertical arrows on the energy axis point to the positions of the Fermi energy.

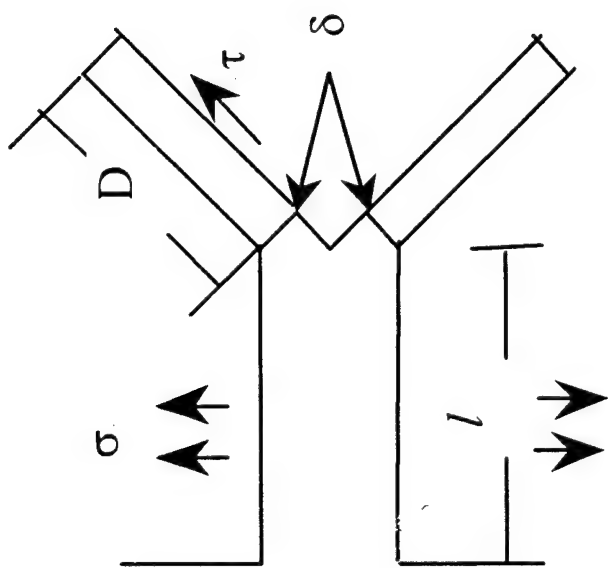


Figure 1: Sketch of fatigue crack growth models.

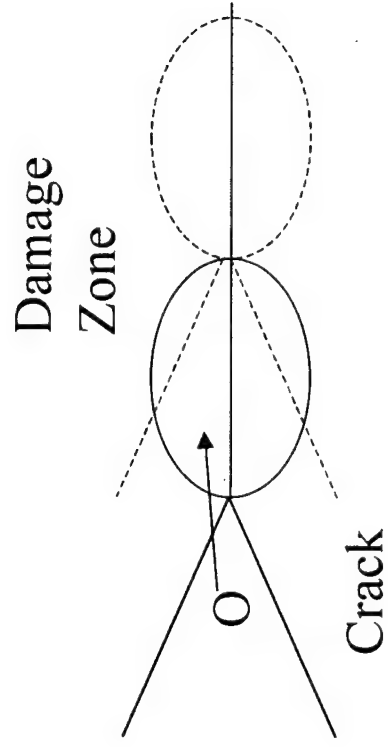


Figure 2: Sketch of the Damage Zone

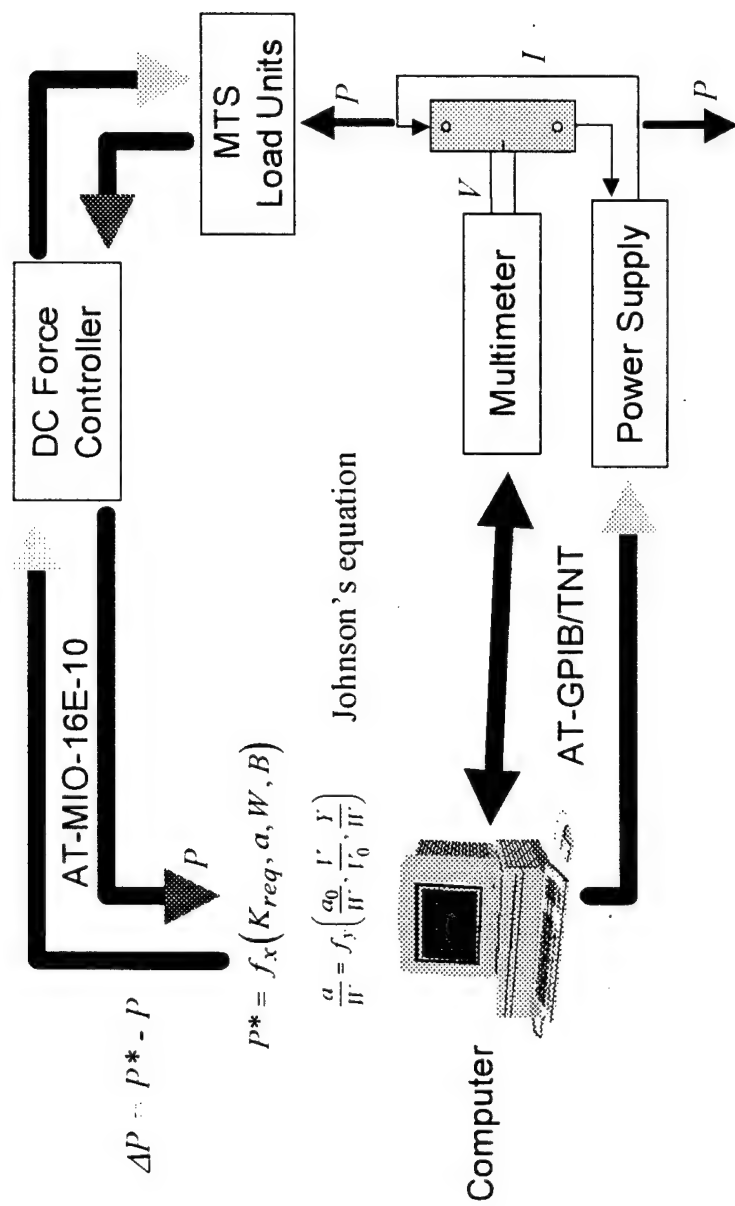


Figure 3: Sketch map for the computer controlled crack monitoring and constant K controlling system.

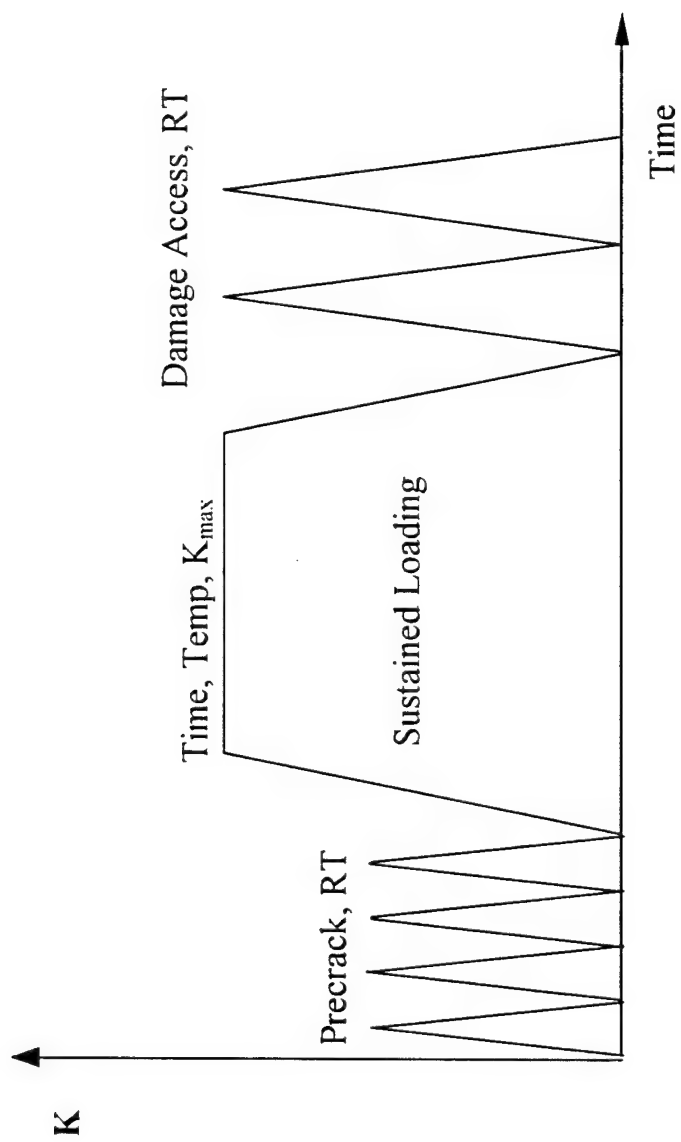
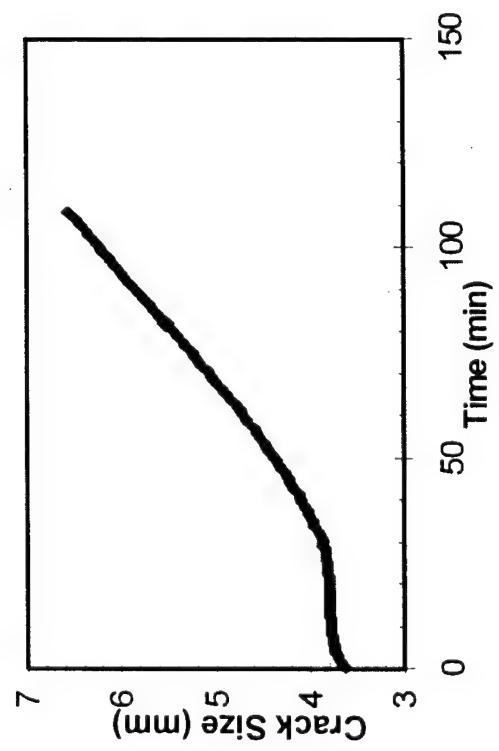
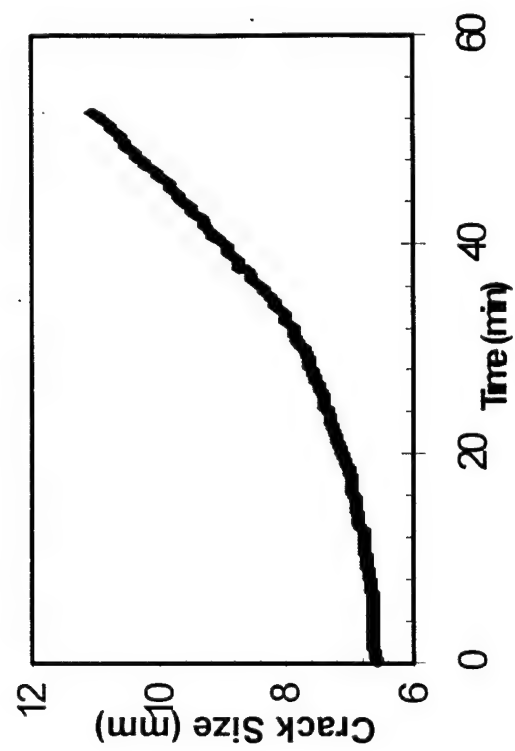


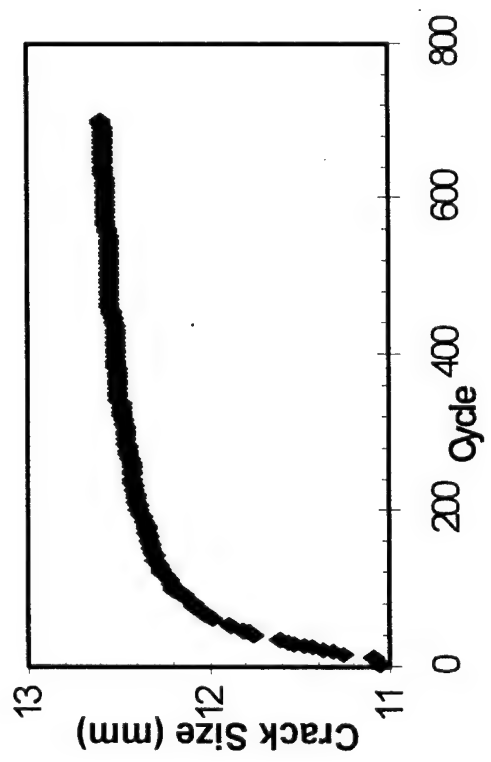
Figure 4. The sketch map of the testing procedure.



(a) Pre-Crack



(b) Sustained Loading



(c) Damage Access

Figure 5: Typical Crack Growth Behavior of IN718.

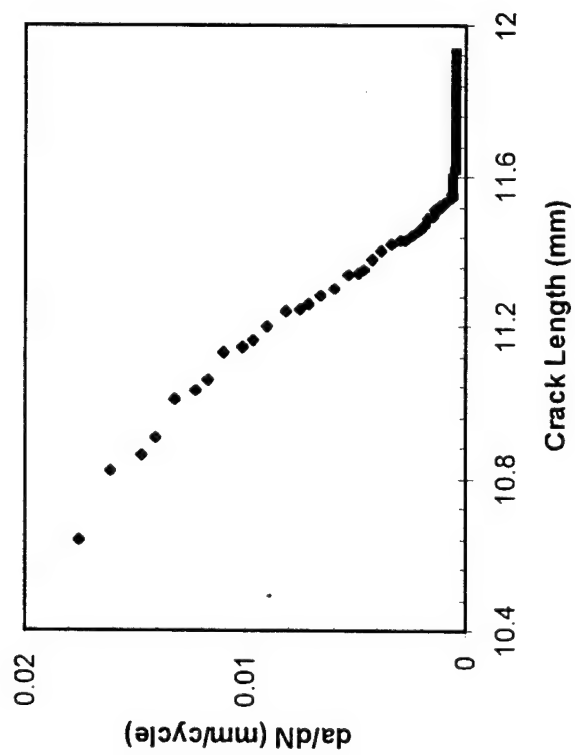


Figure 6: Relationship between da/dN and crack length during Damage Access stage.

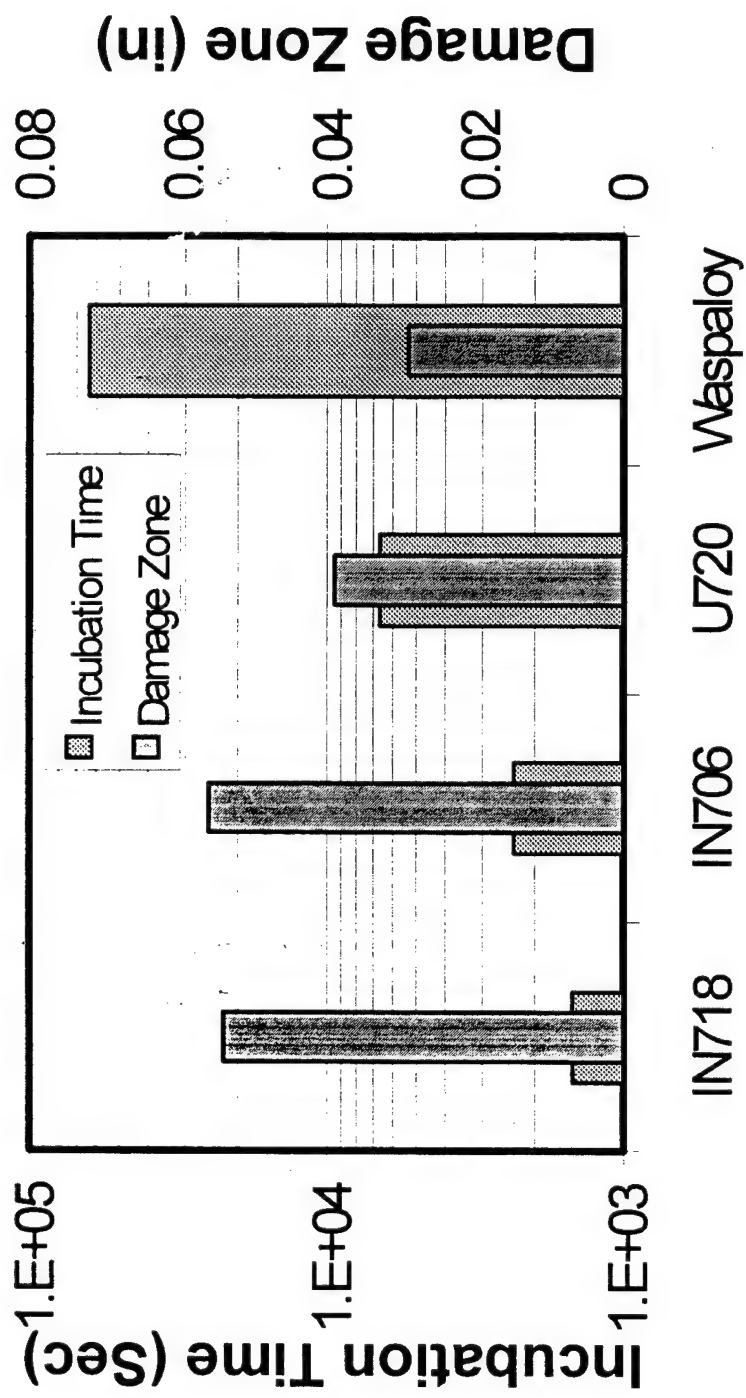


Figure 7: Incubation times and damage zones of the alloys.

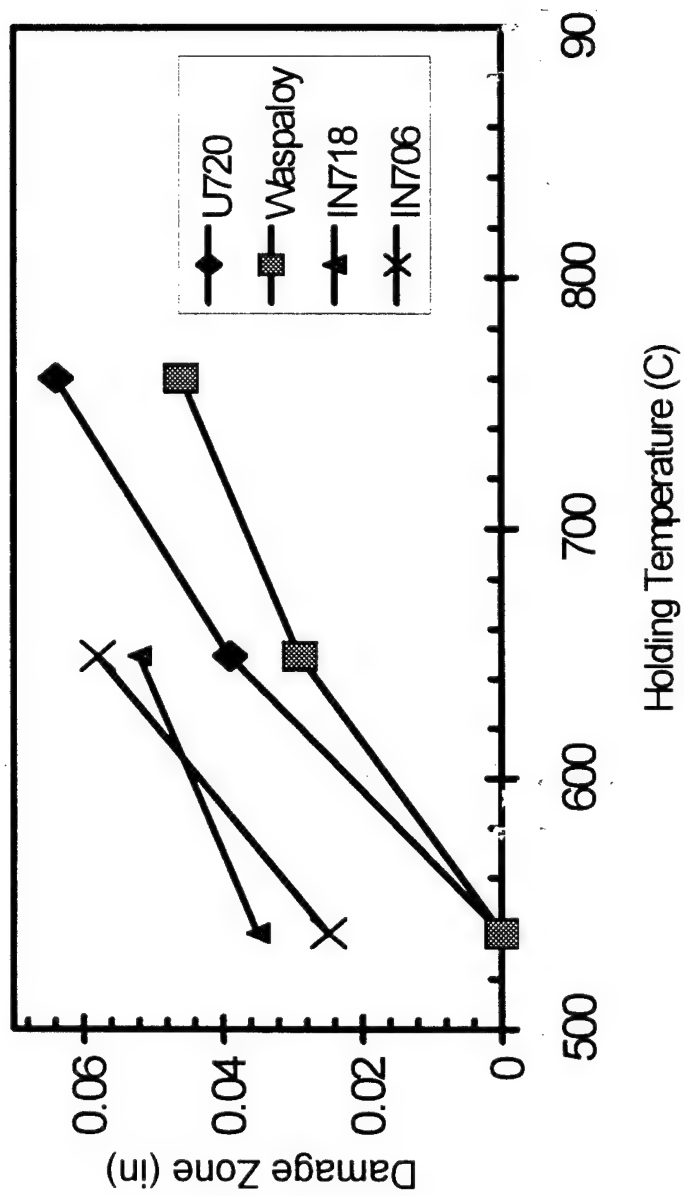
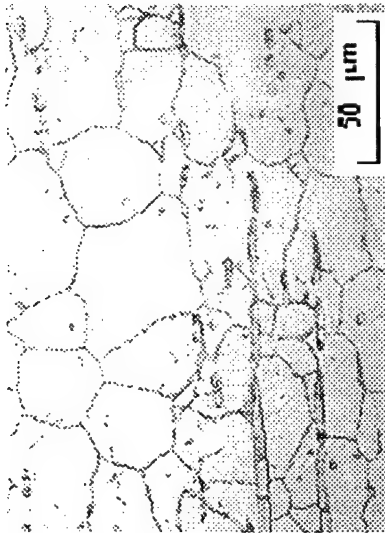
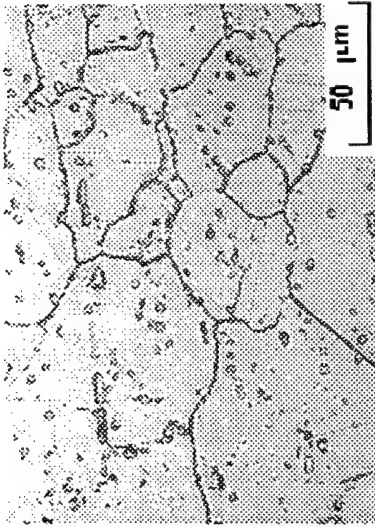


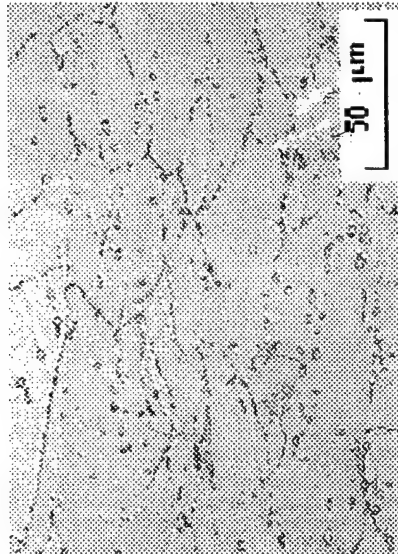
Figure 8: Temperature effect on the damage zone sizes of the alloys.



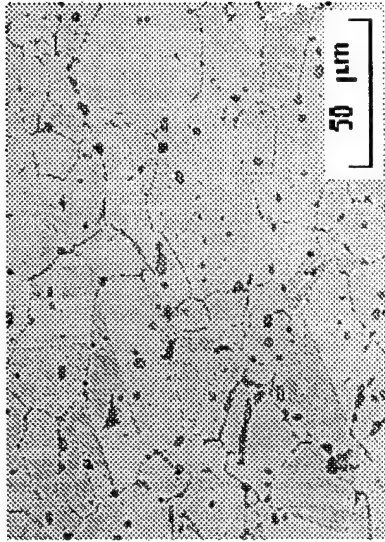
(a) High-Cr. H



(b) Normal Heat Treatment, R

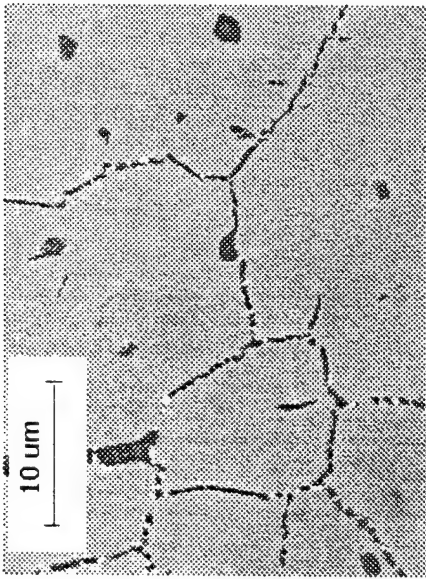


(c) No beta .S

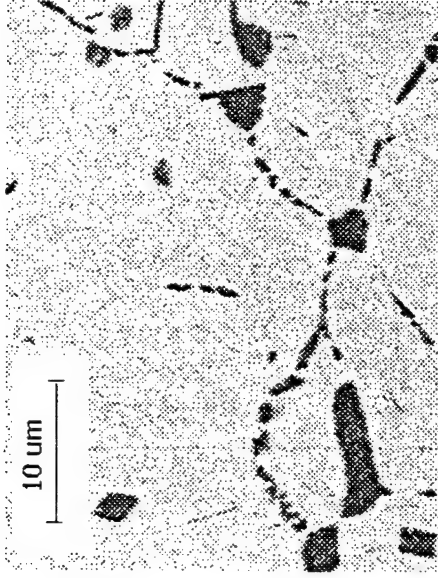


(d) Over exposure, U

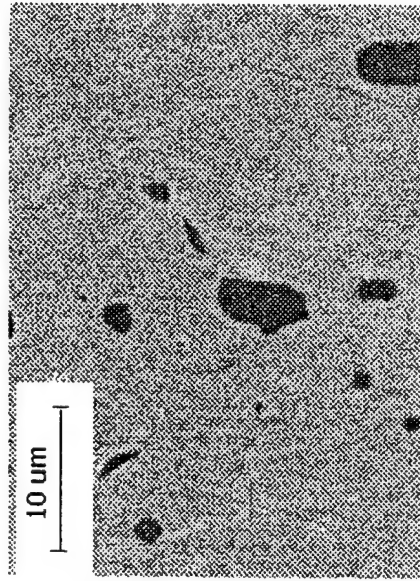
Figure 9. Grain structure of IN783 under different heat treatments.



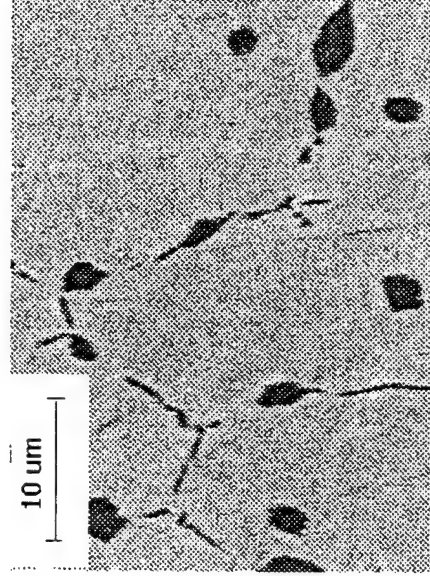
(a) High chrome, H



(b) Normal heat treatment (R)



(c) No β aging heat treatment (S)



(d) Over exposure (U)

Figure 10: SEM micrograph of β phase formation under different heat treatments.

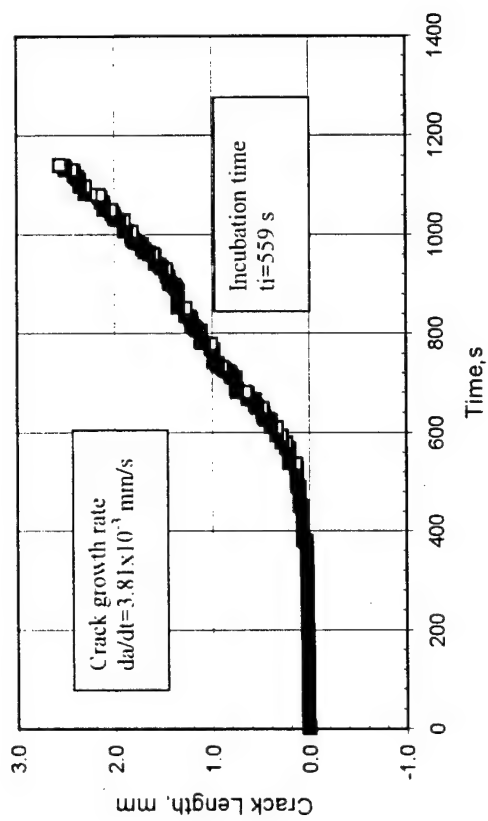


Figure 11: Sustained load crack growth of alloy 783 without β phase aging at $K=38.5 \text{ MPa}\sqrt{\text{m}}$ and 650°C

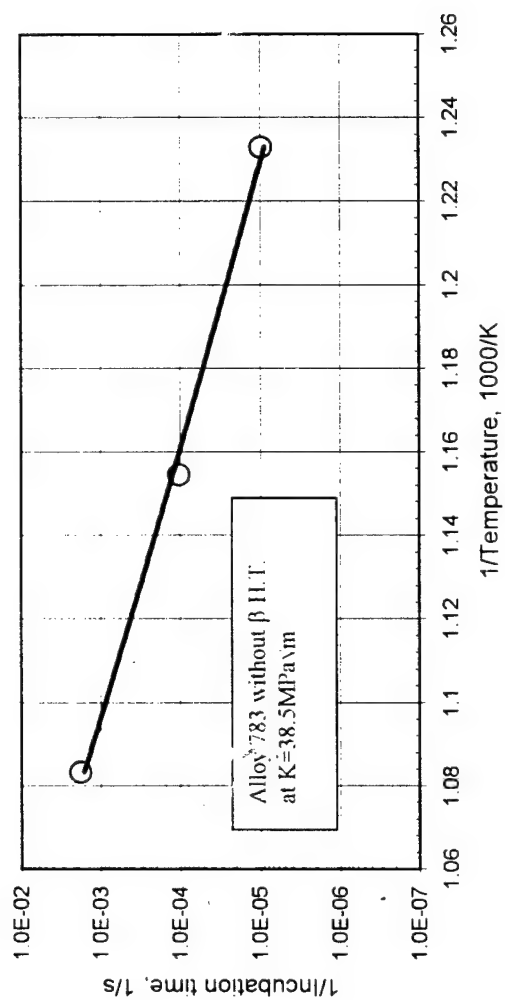


Figure 12: Incubation time as a function of temperature in alloy 783 without β aging, at constant $K=38.5 \text{ MPa}\sqrt{\text{m}}$

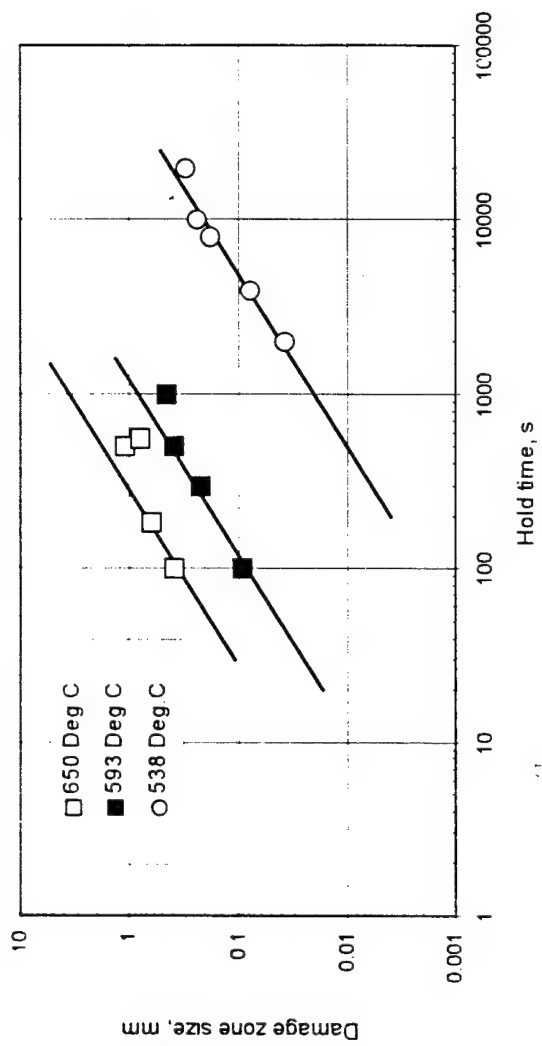


Figure 13: Damage zone size against holding time period at $K_{max} = 38.5 \text{ MPa}\sqrt{\text{m}}$

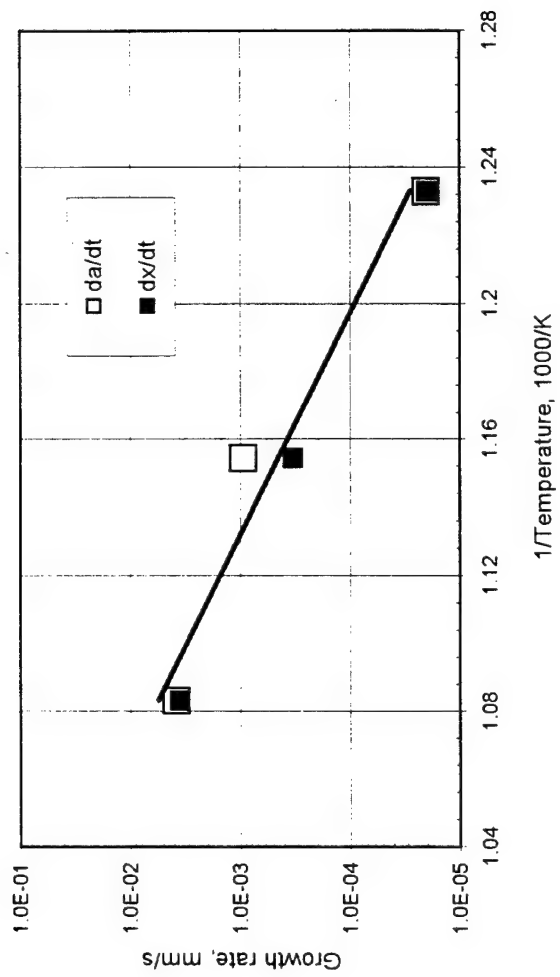


Figure 14: Comparison of da/dt and dx/dt for no β aging at $K_{max} = 38.5 \text{ MPa}\sqrt{\text{m}}$

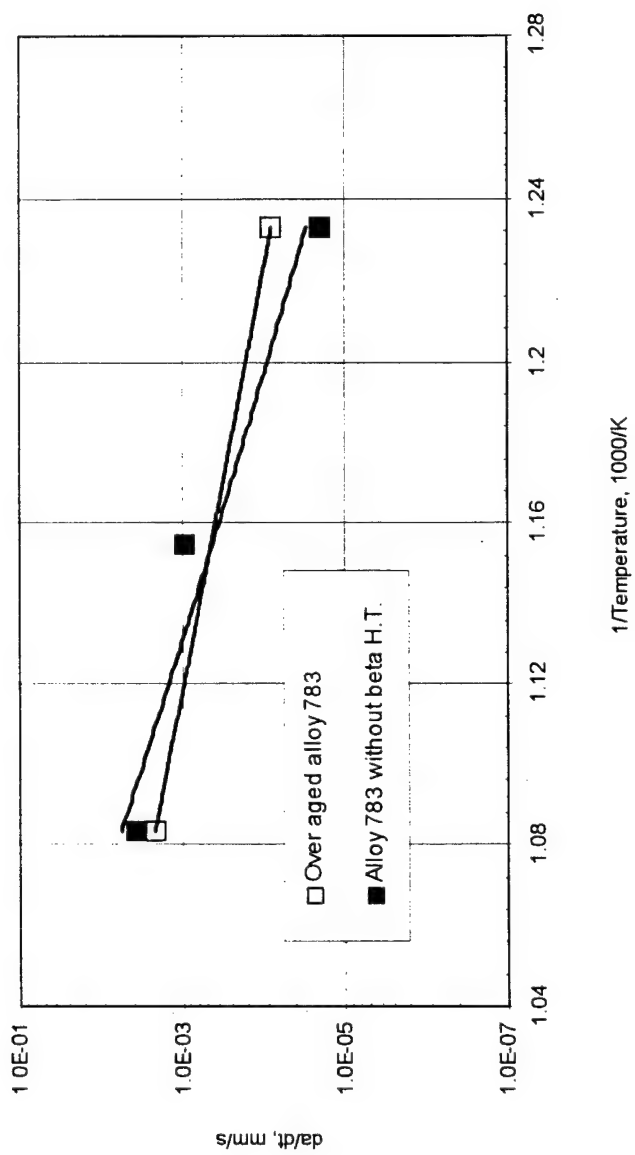


Figure 15: Sustained load crack growth of over aged alloy 783 vs. temperature at $K=38.5 \text{ MPa}\sqrt{\text{m}}$

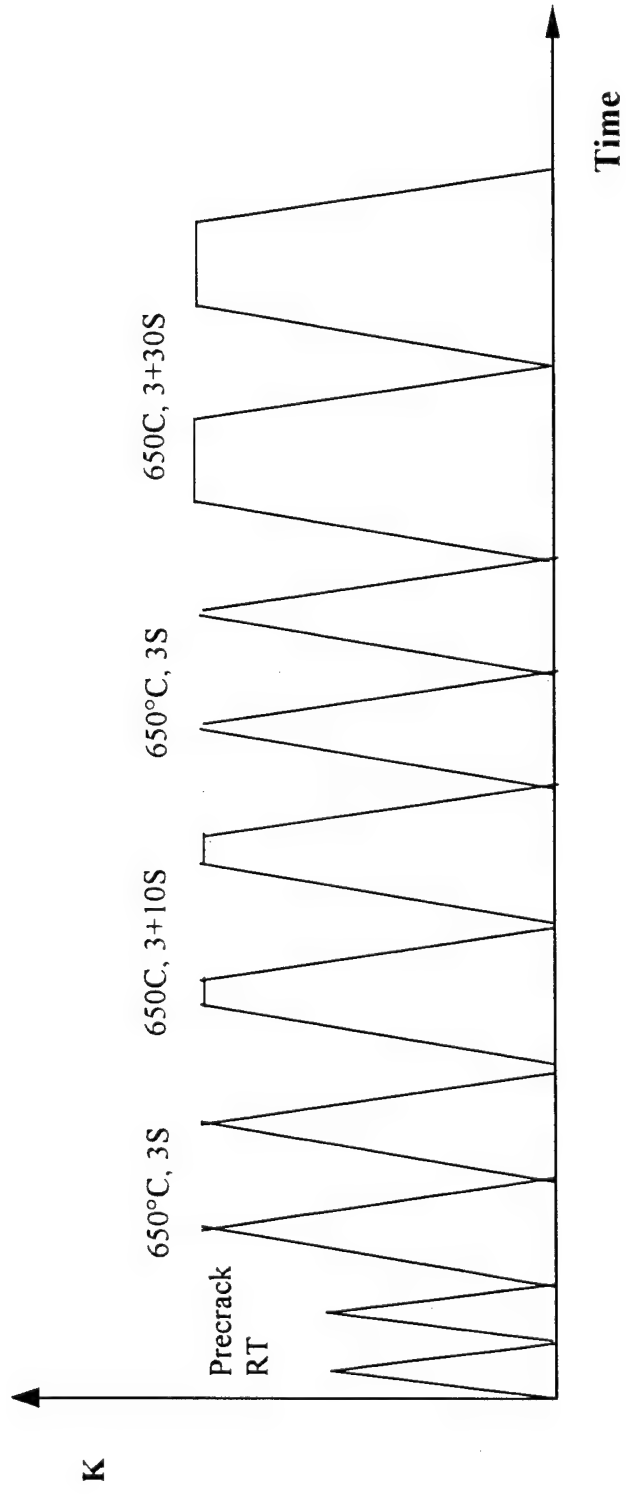


Figure 16: The sketch map of the holding-time fatigue crack growth test.

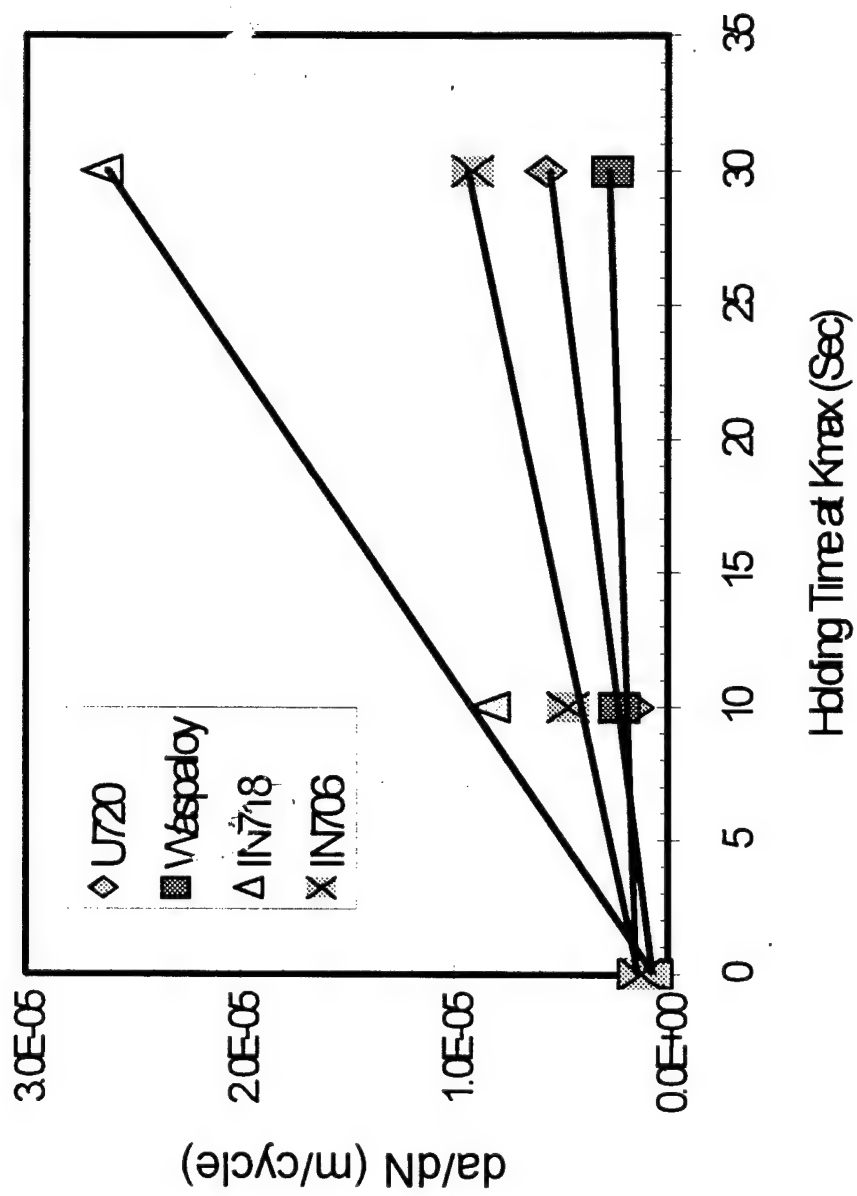
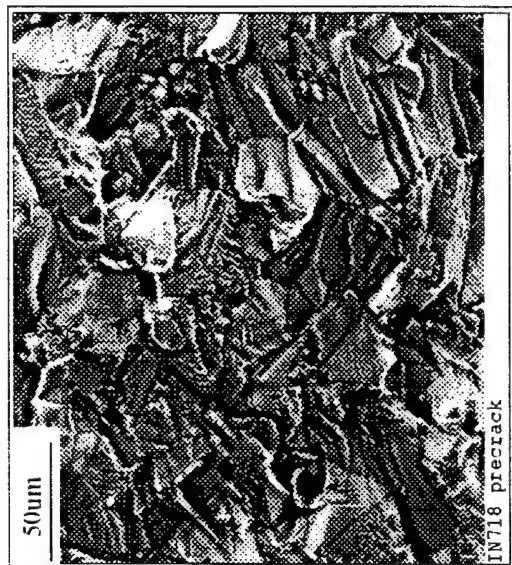
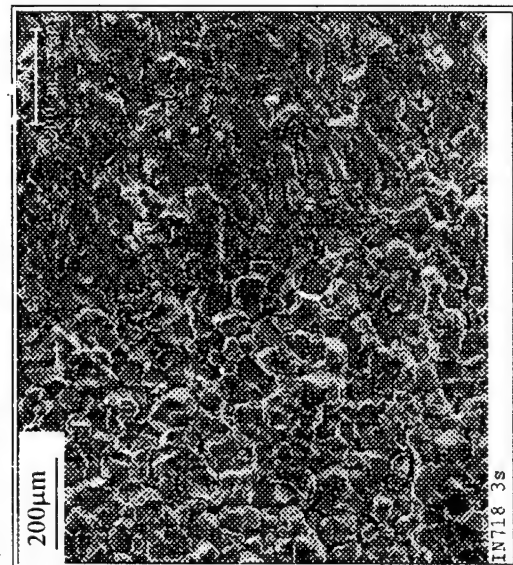


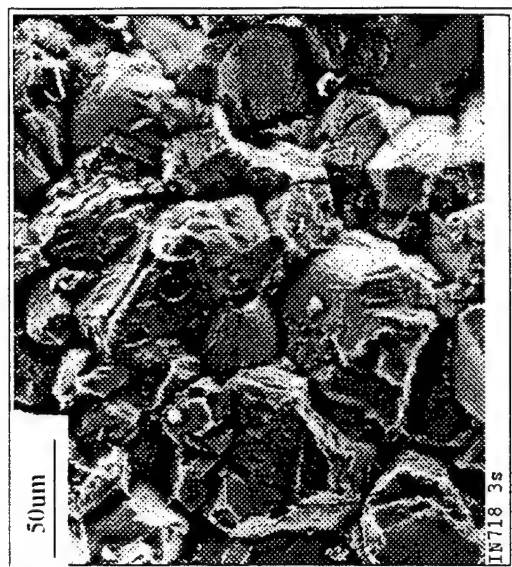
Figure 17: Fatigue crack growth rates of Waspaloy, U720, IN718 and IN706 as function of holding time at maximum stress intensity.



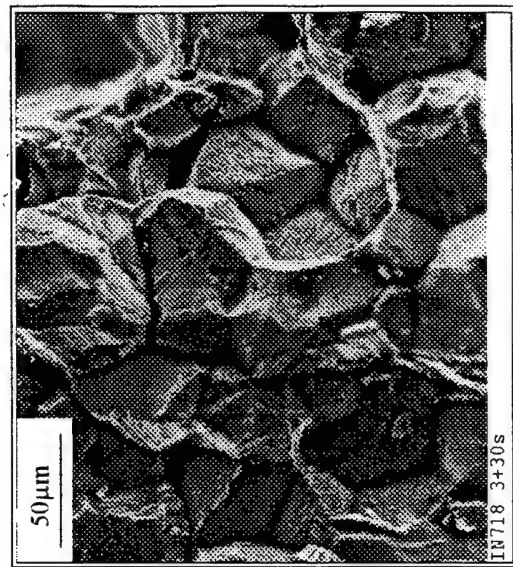
(a) - Precrack



(c) - Transition area, Precrack-Fatigue

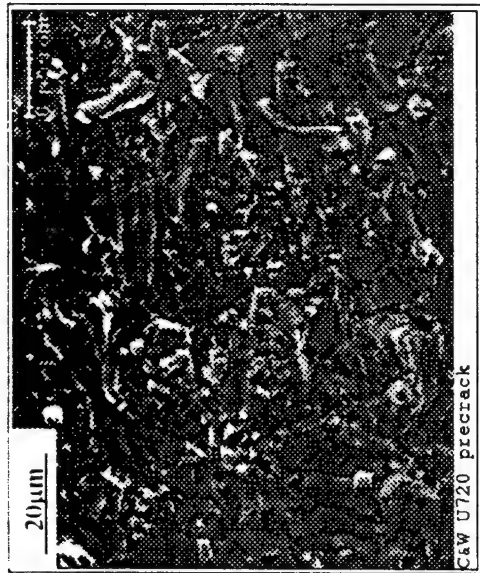


(b) - Fatigue, 3S

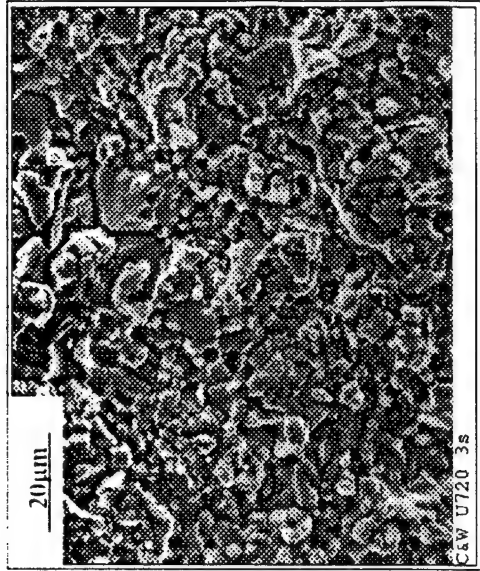


(d) - Fatigue, 3+30S

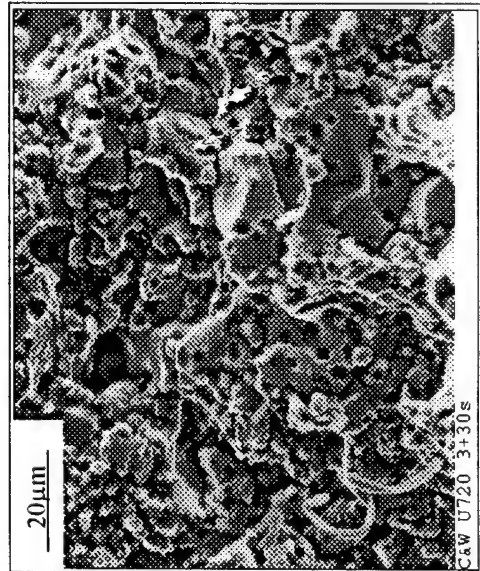
Figure 18: Scanning electron micrographs of IN718 fatigue fracture surfaces.



(a) - Precrack



(b) - Fatigue, 3S



(c) - Fatigue, 3+30S

Figure 19: Scanning electron micrographs of U720 fatigue fracture surfaces.

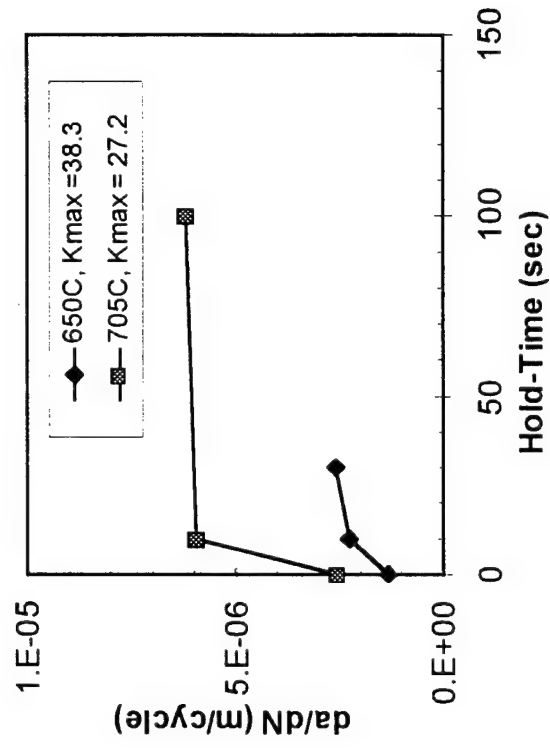


Figure 20: FCG behavior of Waspaloy at 650°C and 705°C under constant ΔK control.

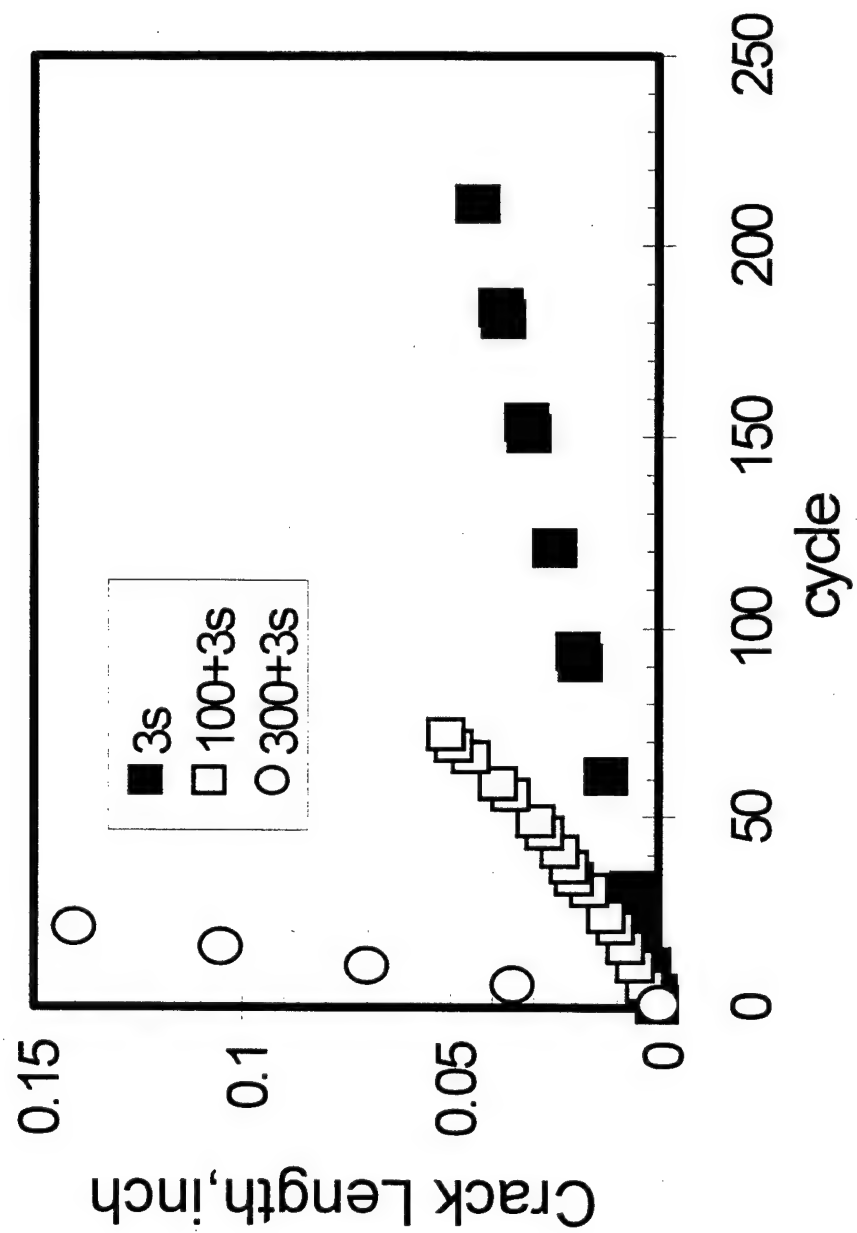
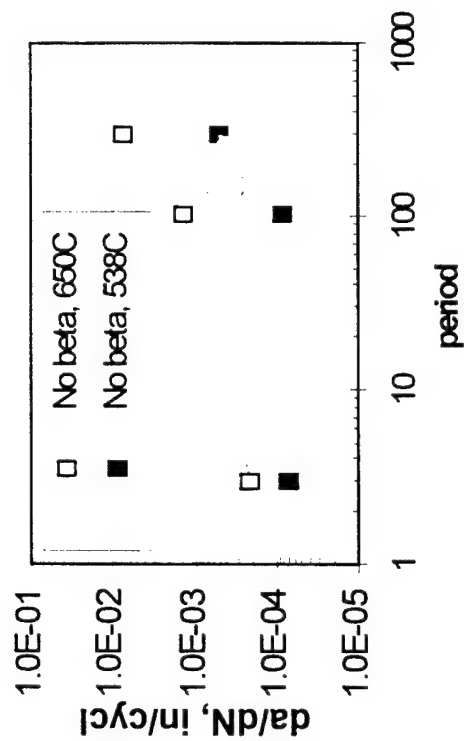
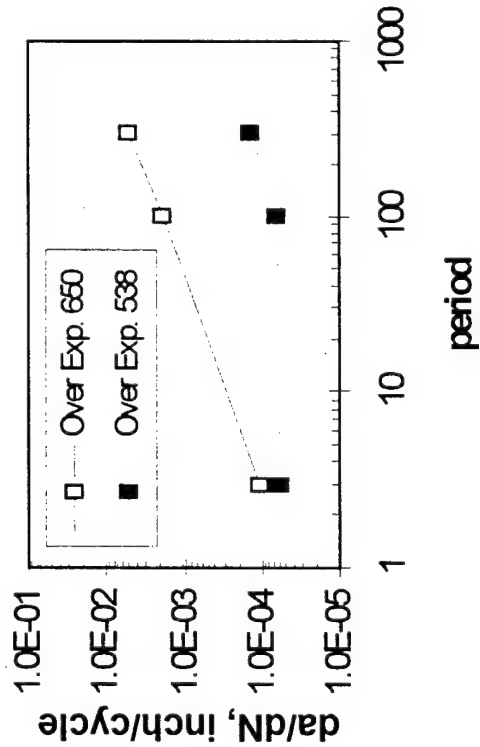


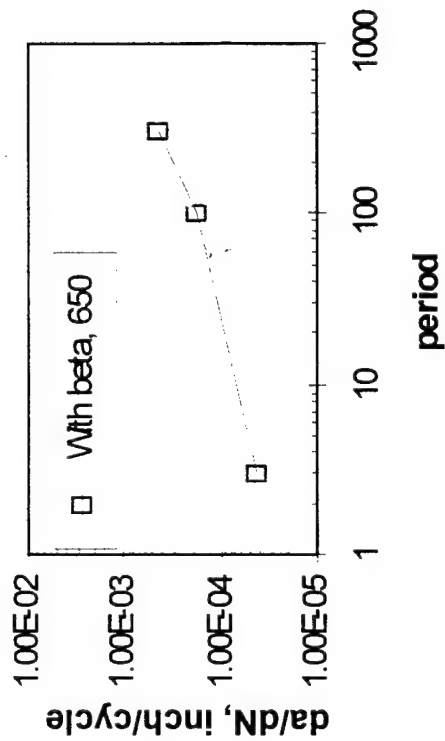
Figure 21: Crack growth of IN783 at constant $\Delta K=33.5 \text{ ksi}\sqrt{\text{in.}}$.



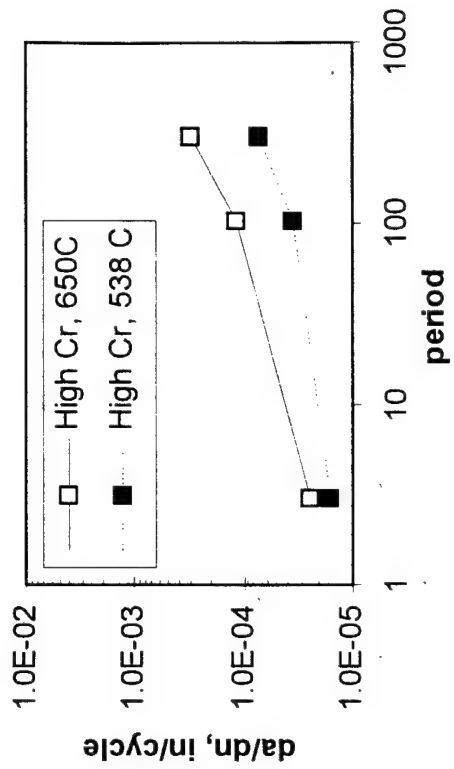
(a) No beta HT (Sample S)



(c) Over exposure (Sample U)



(b) With beta HT (Sample R)



(d) High Chrome (Sample H)

Figure 22: Fatigue crack growth for various treatments

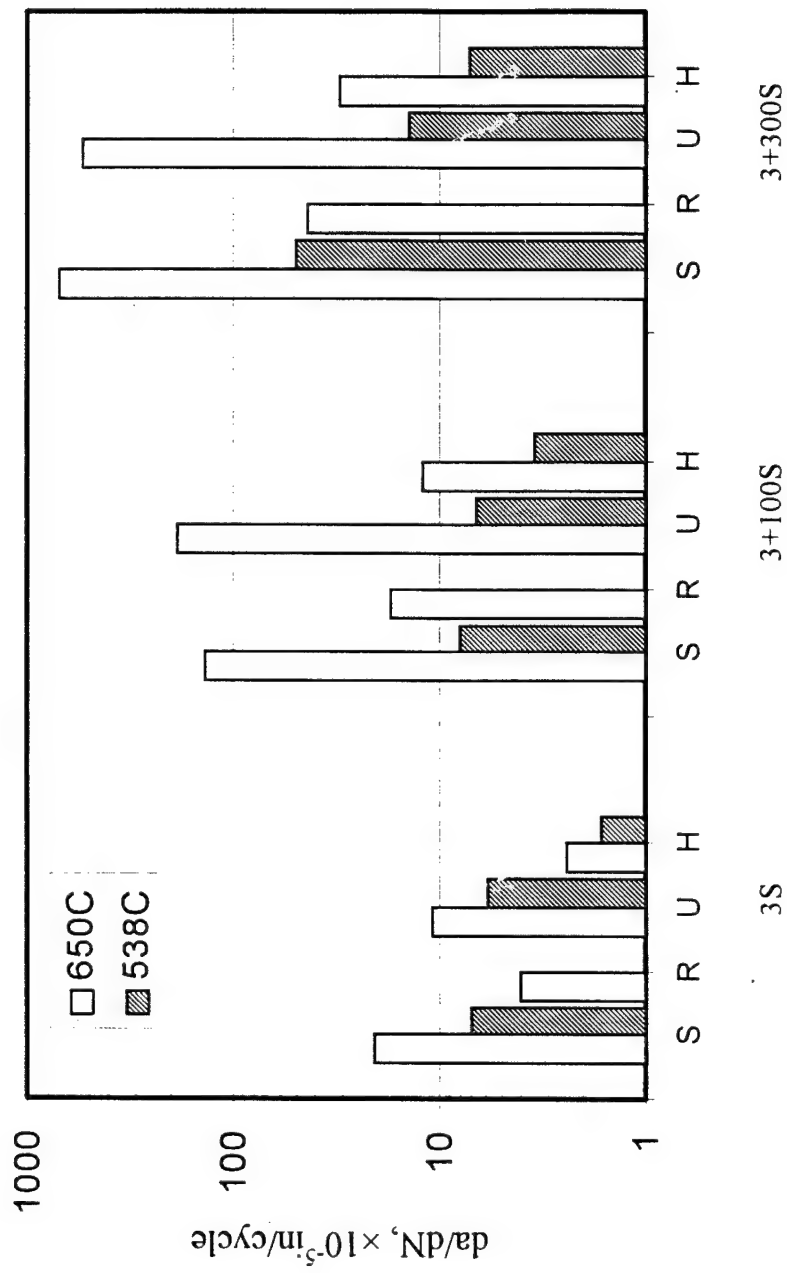


Figure 23: Fatigue crack growth comparison of IN783 alloys with various treatments.

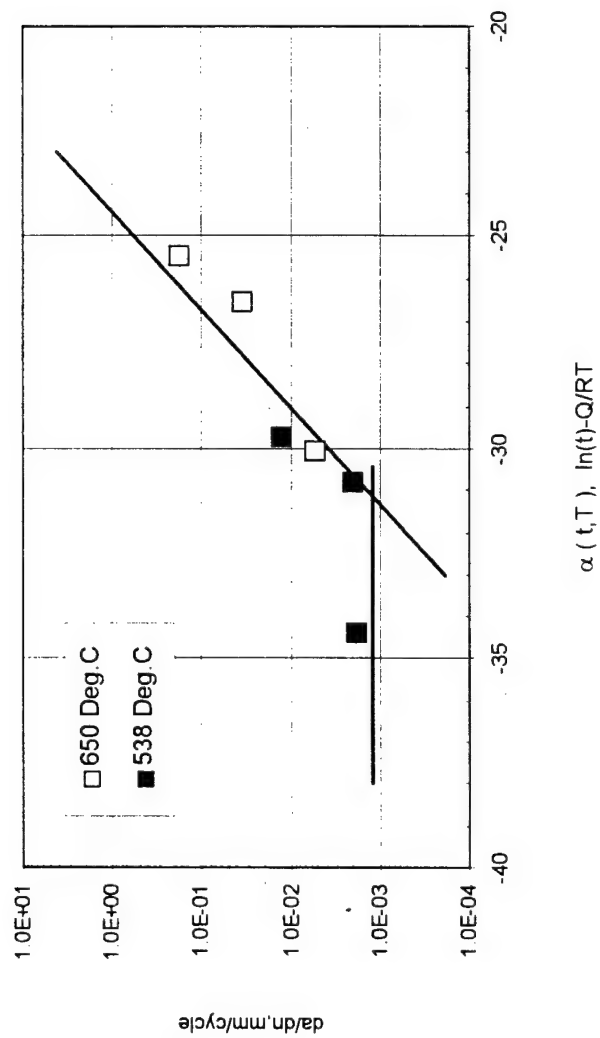


Figure 24: Fatigue crack growth rates of no β aging normalized by time dependent factor at $K=38.5 \text{ MPa}\sqrt{\text{m}}$

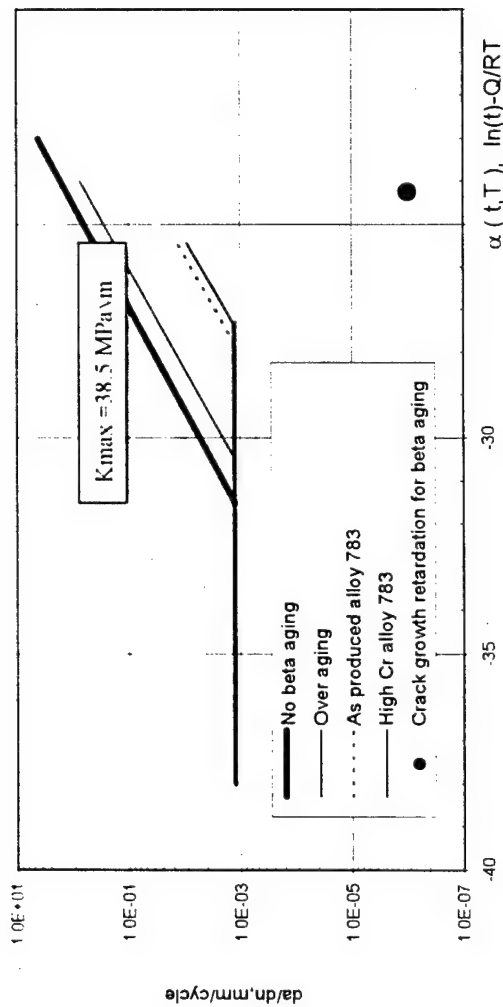


Figure 25: Normalized fatigue crack growth rates of alloy 783

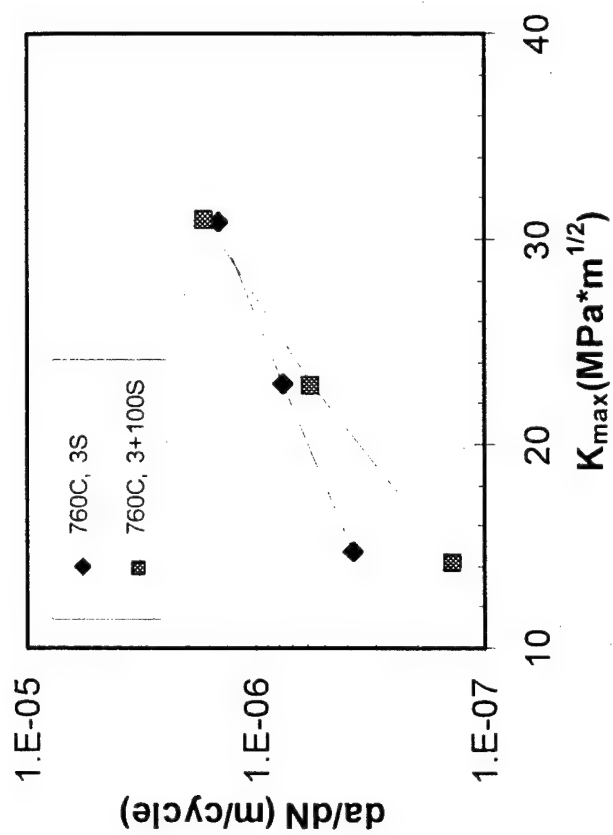


Figure 26: Effect of K on FCGR of Waspaloy at 760°C under 3S and 3+100S loading (constant K control).

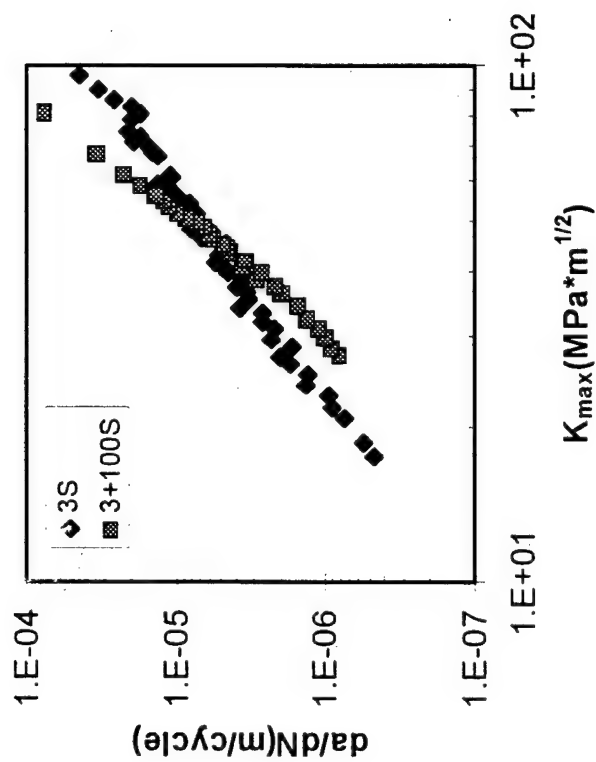
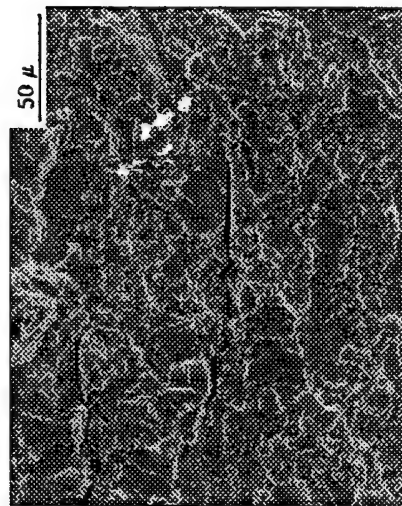
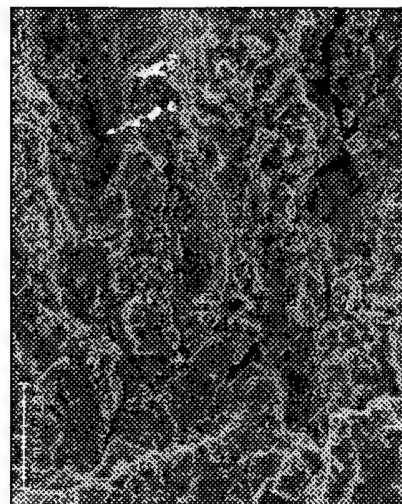


Figure 27: Effect of K on FCGR of Waspaloy at 760°C under 3S and 3+100S loading (constant load control).

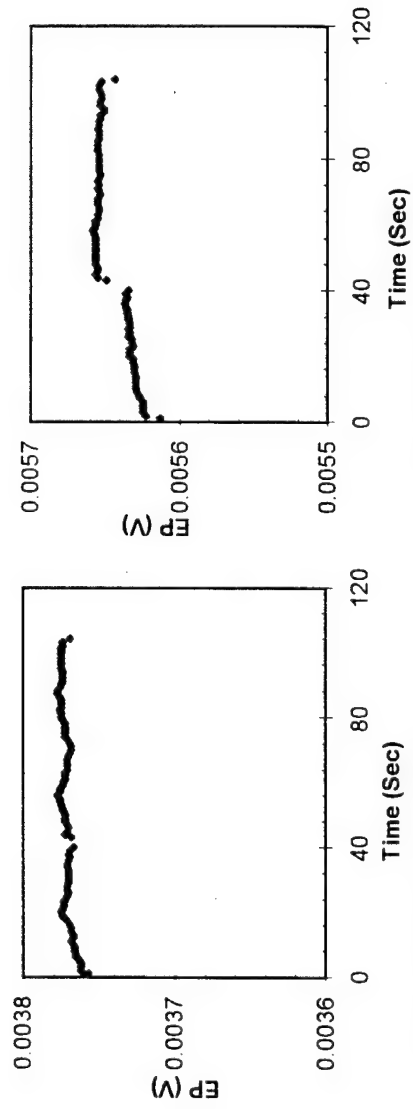


(a) Constant Load Control, 760°C, 3 S



(b) Constant Load Control, 760°C, 3+100S

Figure 28: Fracture surfaces of the specimens after constant load control FCG tests at 760°C



(a) Cycle 2806, in steady state

(b) Cycle 4626, in stage III

Figure 29: The FCG behaviors within one cycle during various stages. (760°C, 3+100S)

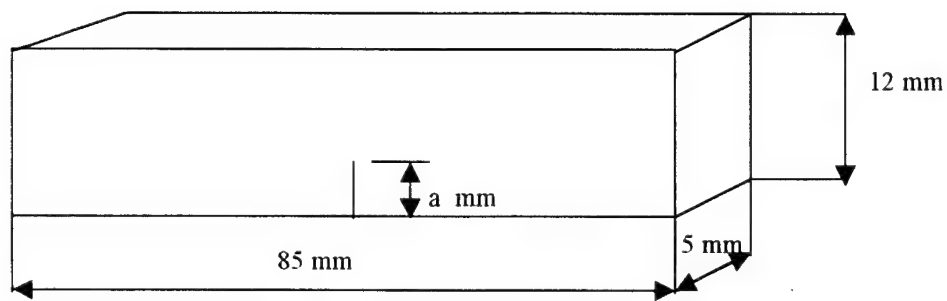


Figure 30: Specimen Dimensions

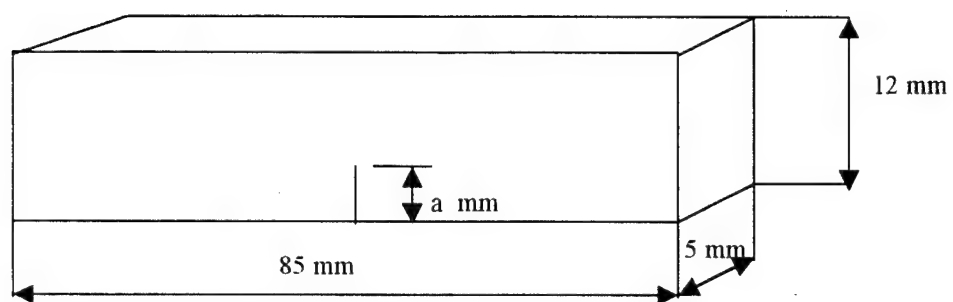
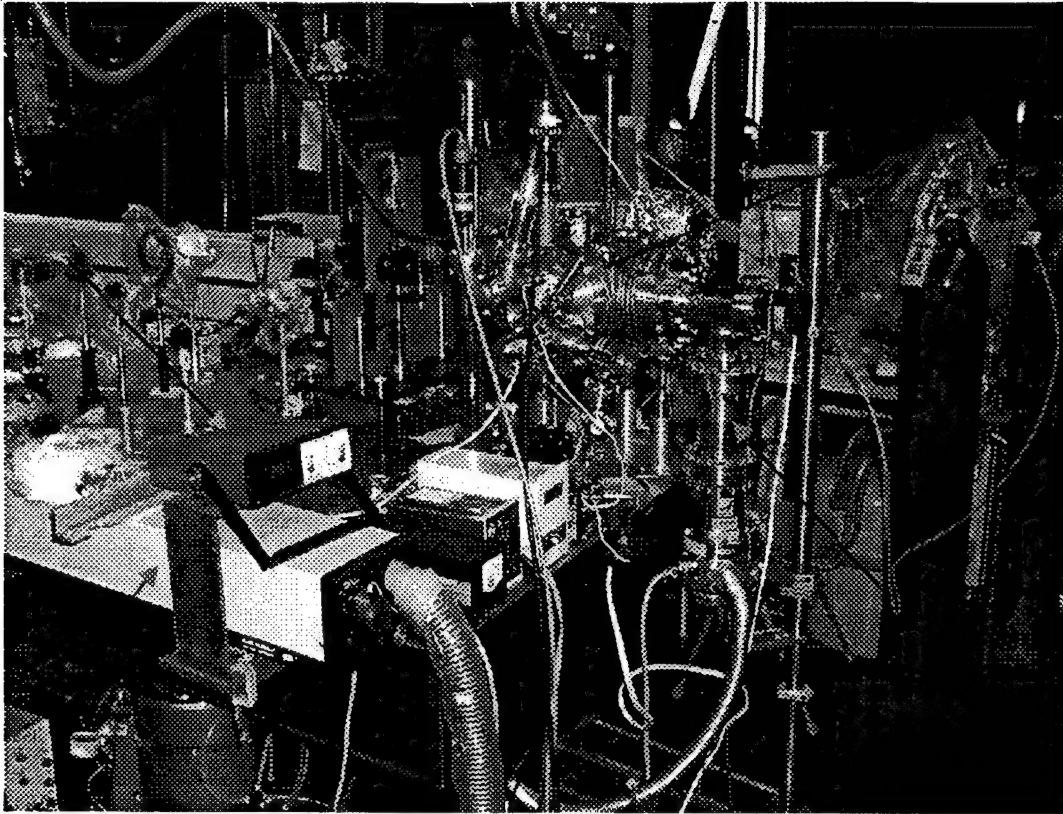
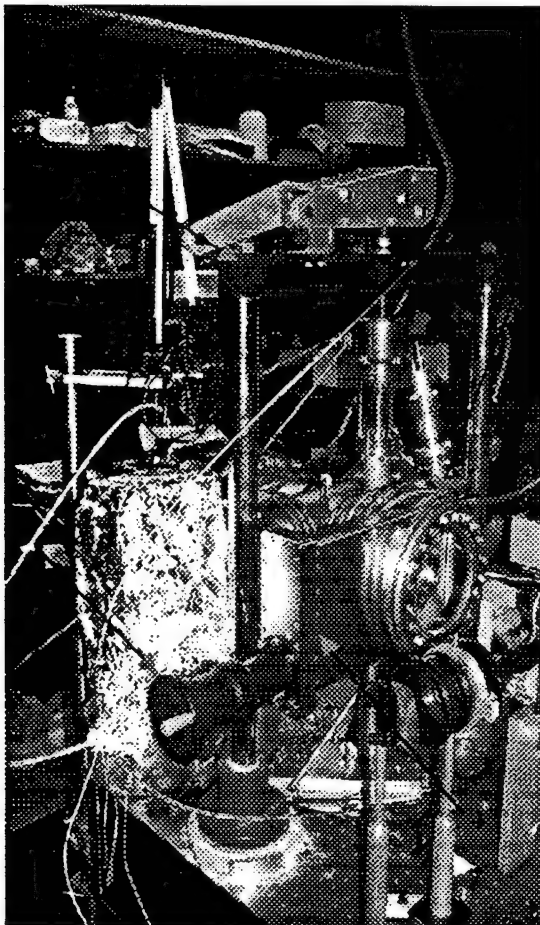


Figure 30: Specimen Dimensions



Back view



Front view

1. Ion Pump
2. Loading Frame
3. Cooling System
4. Shutter
5. Argon Laser
6. Digital Thermometer
7. Testing Chamber
8. Turbomolecular Pump

Figure 31: UHV Material Testing System

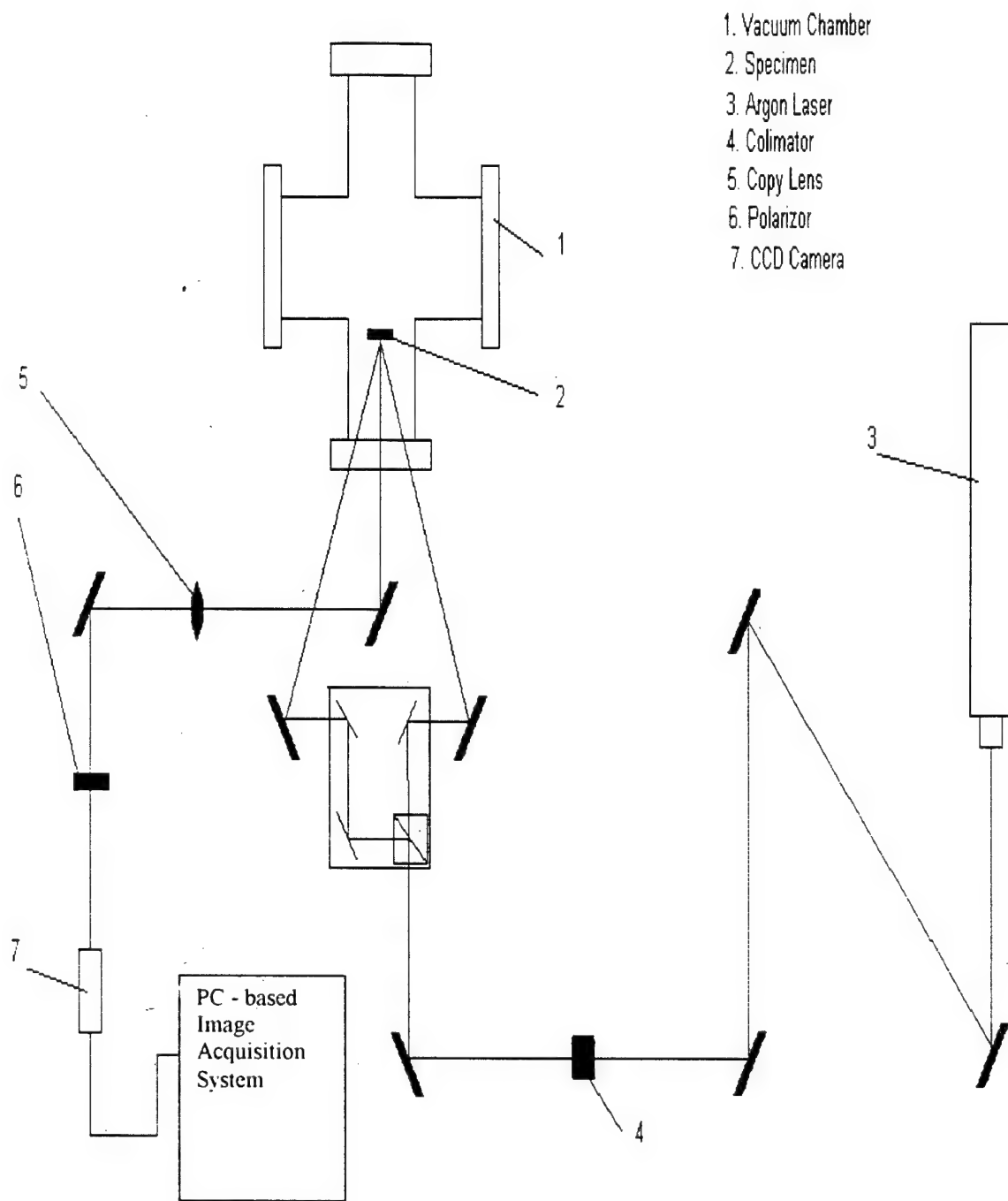


Figure 32: Schematic of Moiré Interferometry Set-up.

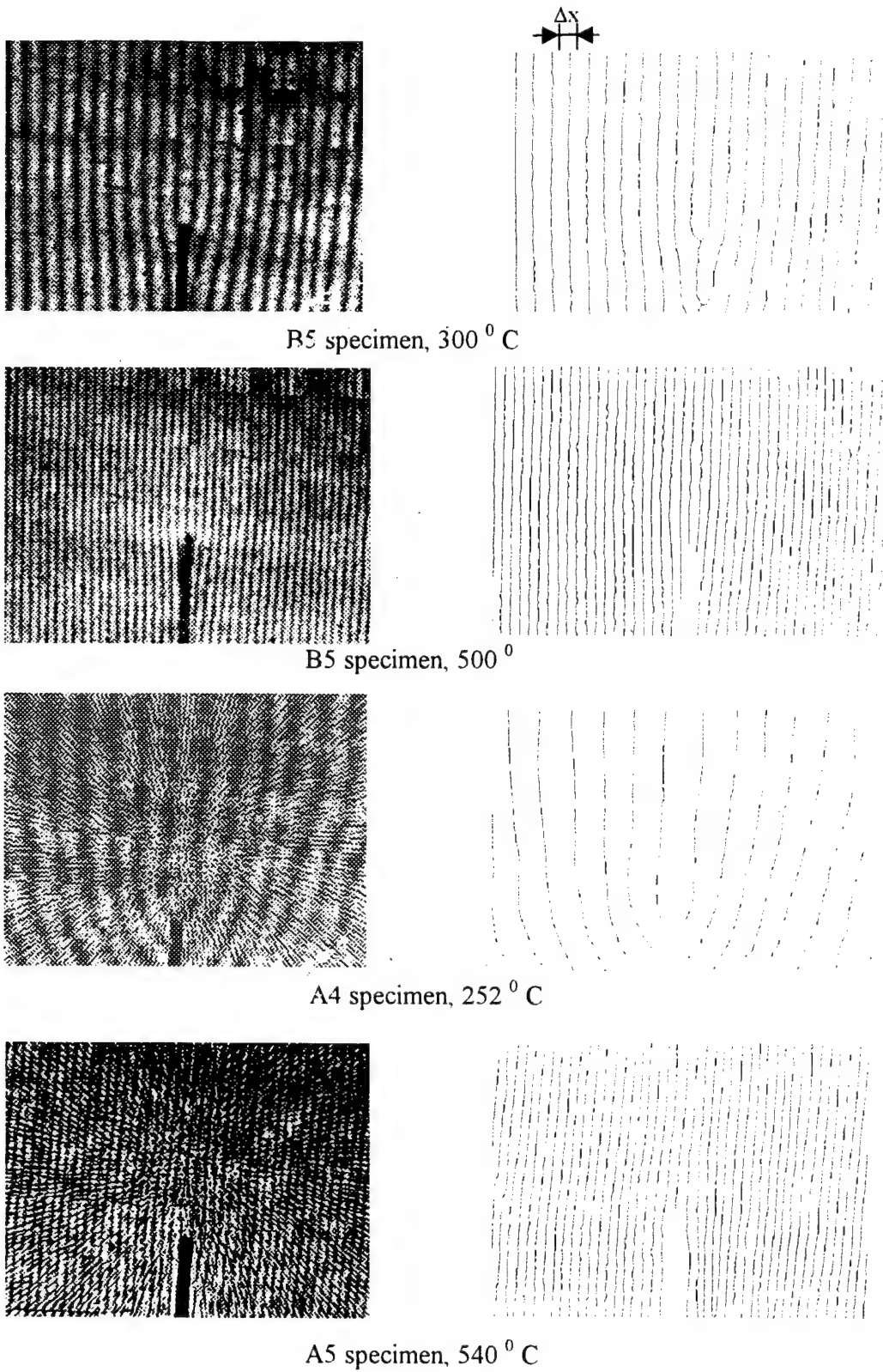


Figure 33: Comparative fringe pattern induced by thermal expansion.

Thermal expansion

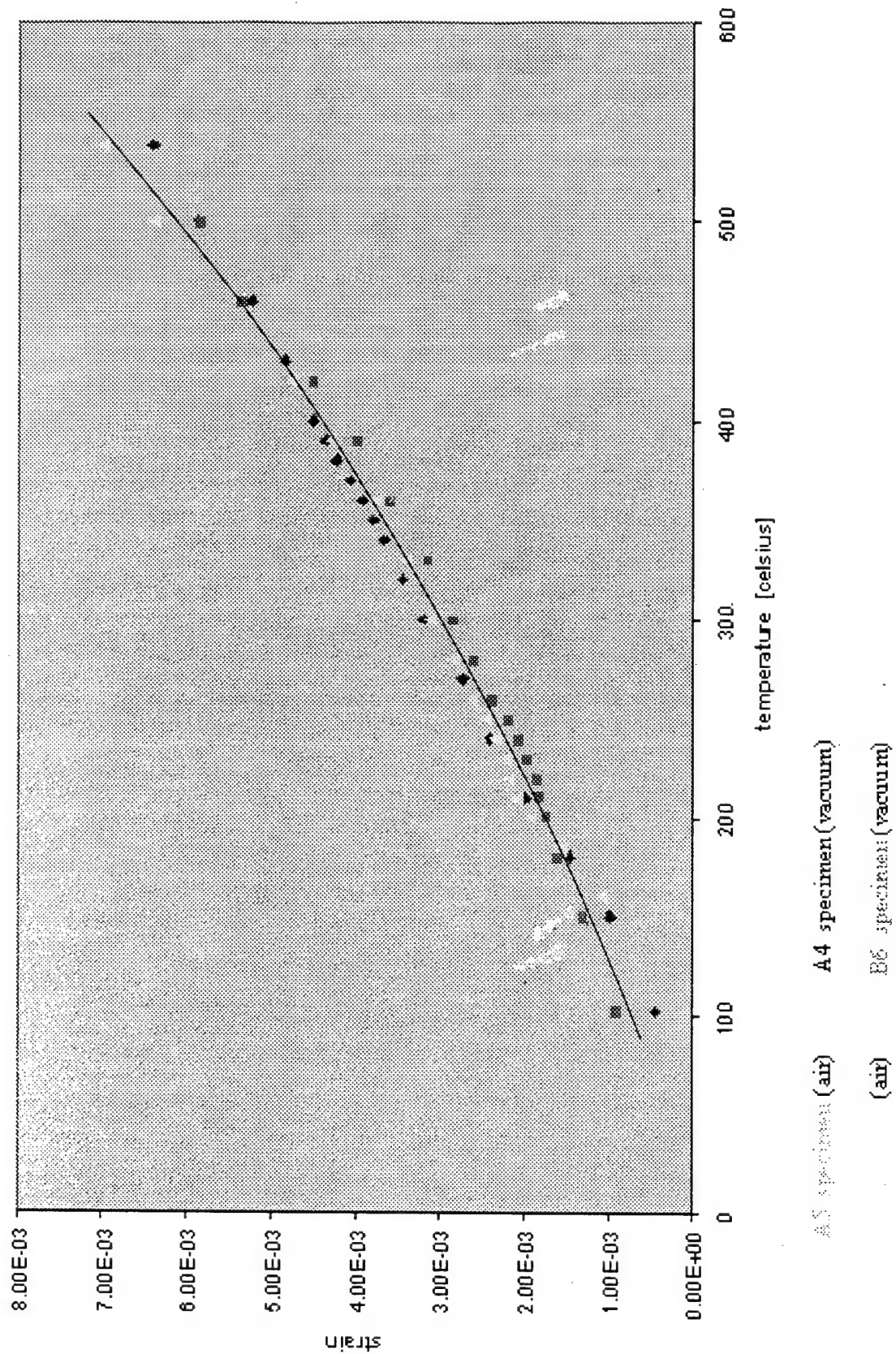
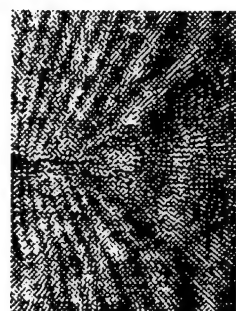
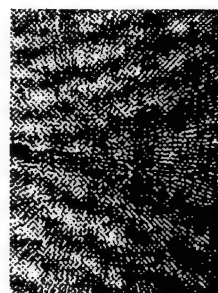


Figure 34: Comparative thermal expansion data of different specimens in different environmental conditions.



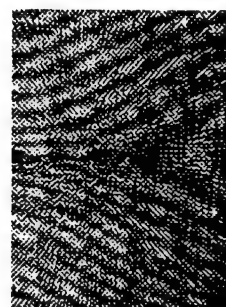
1.36 mm

$P = 578.5 \text{ N}$
 $K_I = 12.52 \text{ Mpa}\sqrt{\text{m}}$
 $t=0\text{h}$



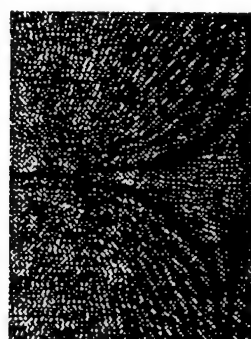
1.36 mm

$P = 1085.5 \text{ N}$
 $K_I = 23.5 \text{ Mpa}\sqrt{\text{m}}$
 $t=15 \text{ min}$



1.36 mm

$P = 2549 \text{ N}$
 $K_I = 55.2 \text{ Mpa}\sqrt{\text{m}}$
 $t=30 \text{ min}$



1.36 mm

$P = 3092 \text{ N}$
 $K_I = 63.4 \text{ Mpa}\sqrt{\text{m}}$
 $t=45 \text{ min}$



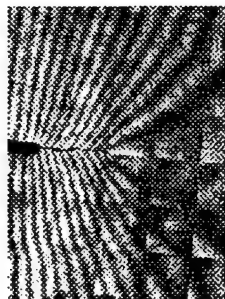
Figure 35: A5 specimen, 538°C , air

Observed initiated crack growth at $P = 694 \text{ N}$

$K_I = 12.48 \text{ Mpa}\sqrt{\text{m}}$

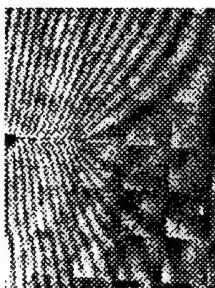
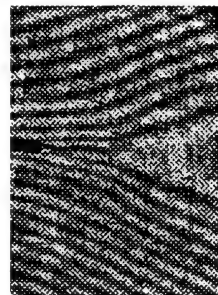
$t=0\text{h}$

0.80 mm



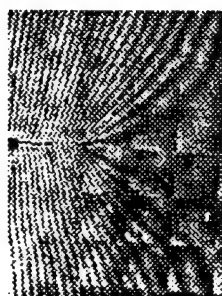
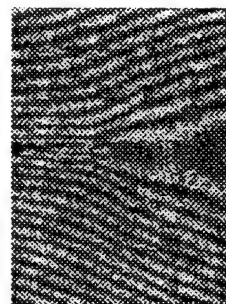
1.36 mm

$P = 1068 \text{ N}$
 $K_I = 20.31 \text{ Mpa}\sqrt{\text{m}}$
 $t=10 \text{ min}$



1.44 mm

$P = 1357 \text{ N}$
 $K_I = 26.08 \text{ Mpa}\sqrt{\text{m}}$
 $t=20 \text{ min}$



1.46 mm

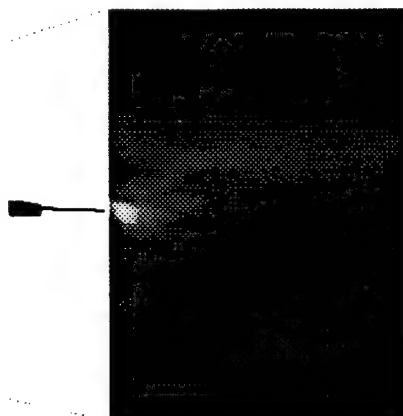
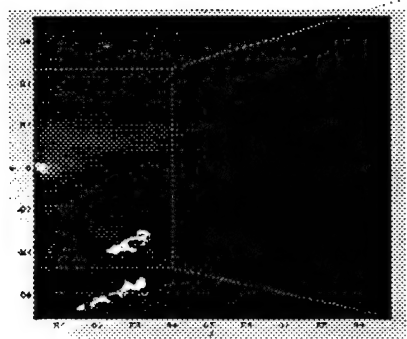
$P = 1833 \text{ N}$
 $K_I = 35.42 \text{ Mpa}\sqrt{\text{m}}$
 $t=30 \text{ min}$



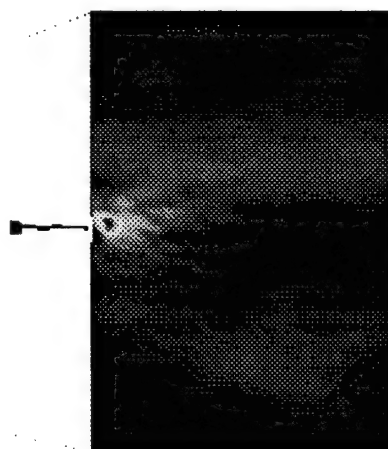
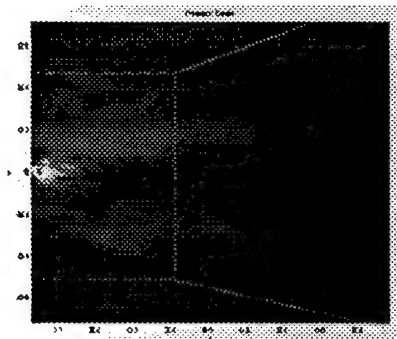
v field

u field

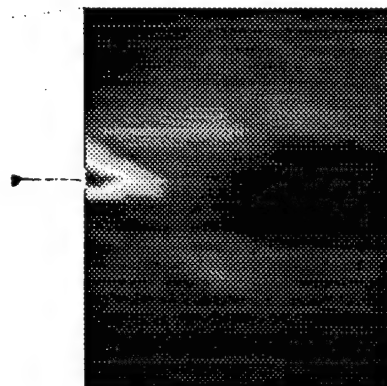
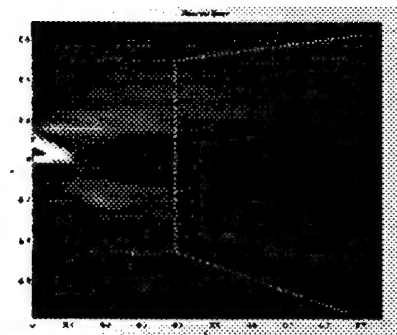
Figure 36: B5 Specimen, 538°C , air



$P = 1068 \text{ N}$
 $K_I = 20.31 \text{ Mpa}\sqrt{\text{m}}$



$P = 1357 \text{ N}$
 $K_I = 26.08 \text{ Mpa}\sqrt{\text{m}}$



$P = 1833 \text{ N}$
 $K_I = 35.42 \text{ Mpa}\sqrt{\text{m}}$

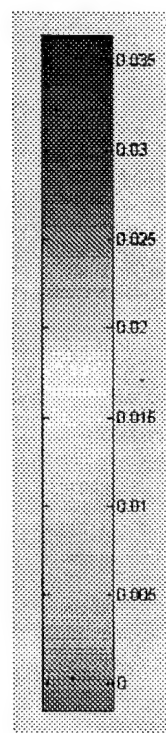
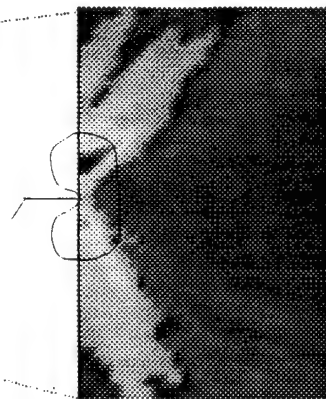
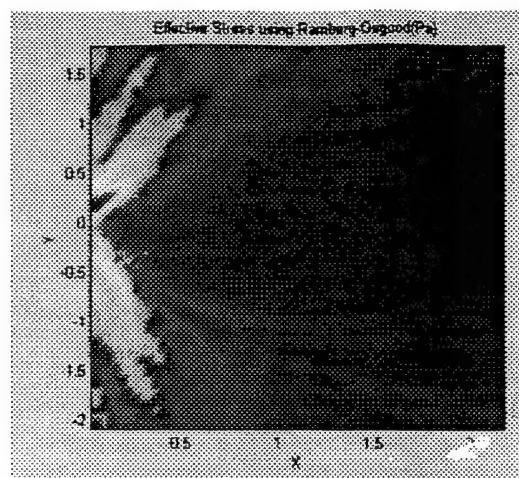
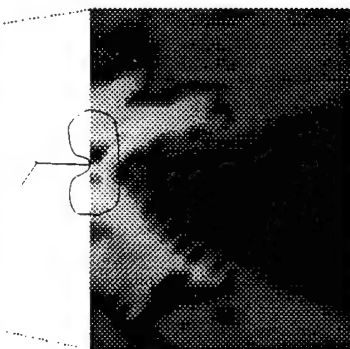
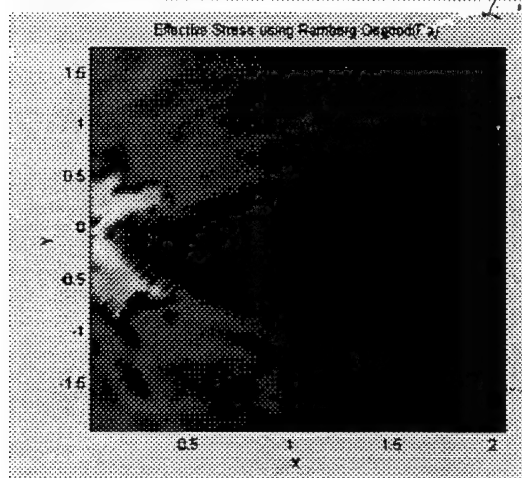


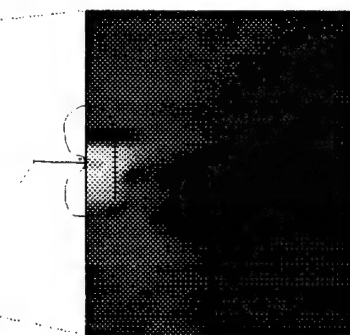
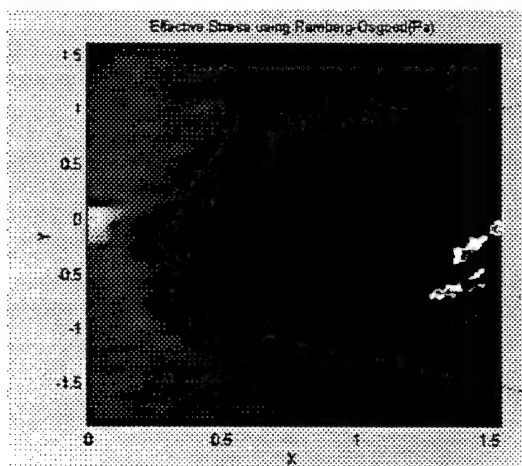
Figure 37: Principal Strains Distribution, B5 Specimen, 538°C, air



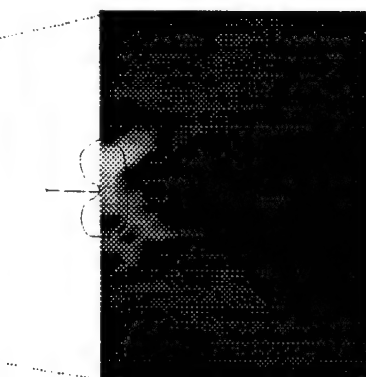
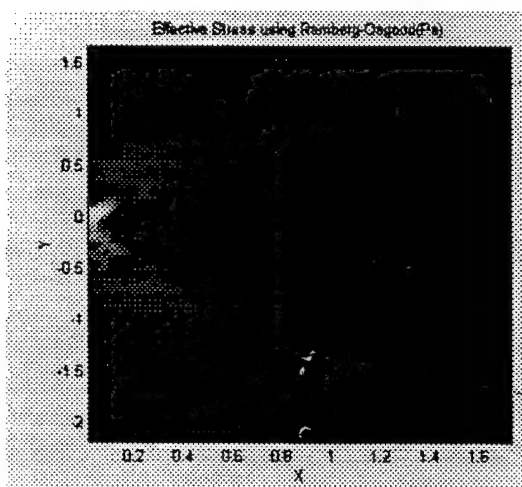
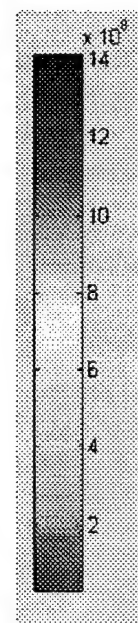
P=2385 N



P=1833 N

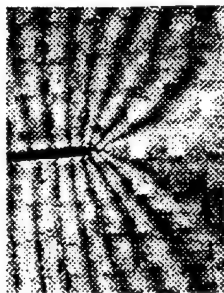


P=1357 N



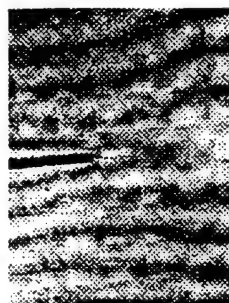
P=1068 N

Figure 38, B5 Specimen Effective Stresses

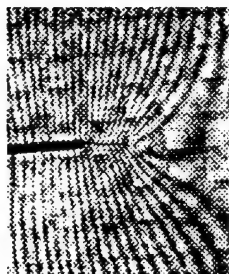


0.62 mm

t=0h

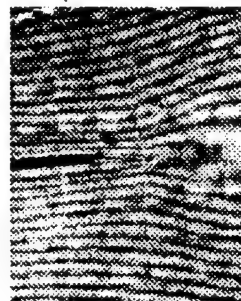


P = 542.9 N
K_I = 10.33 Mpa√m

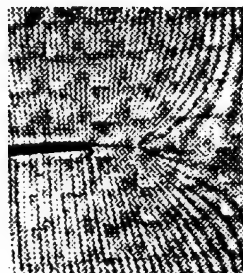


1.27 mm

t = 5 min



P = 1335 N
K_I = 29.23 Mpa√m



1.31 mm

t = 10 min

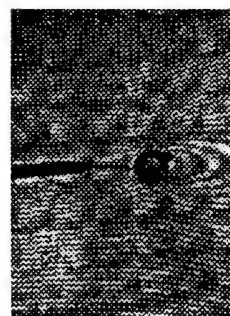


P = 2024 N
K_I = 45.30 Mpa√m



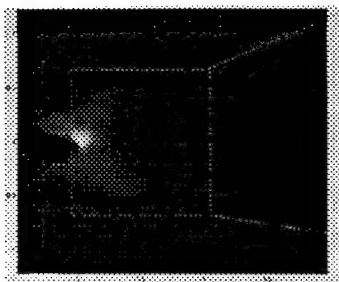
1.31 mm

t = 15 min

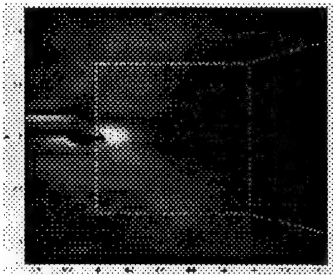
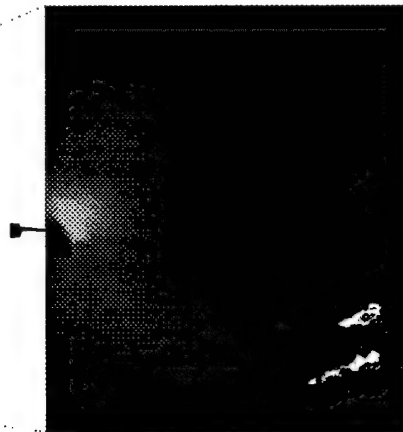


P = 2558 N
K_I = 51.2 Mpa√m

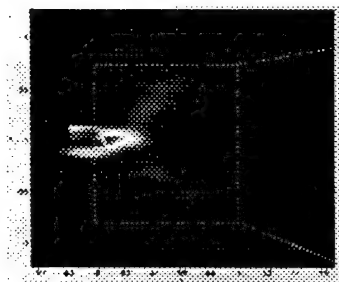
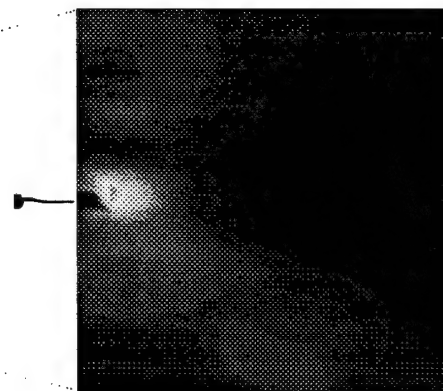
Figure 39, B4 Specimen, 650⁰ C, air



$P = 542.9 \text{ N}$
 $K_I = 10.33 \text{ Mpa}\sqrt{\text{m}}$



$P = 1335 \text{ N}$
 $K_I = 29.23 \text{ Mpa}\sqrt{\text{m}}$



$P = 2024 \text{ N}$
 $K_I = 45.30 \text{ Mpa}\sqrt{\text{m}}$

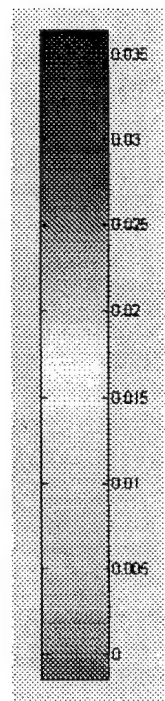


Figure 40: B4 specimen, 650⁰ C, air
 Principal Strain Distribution

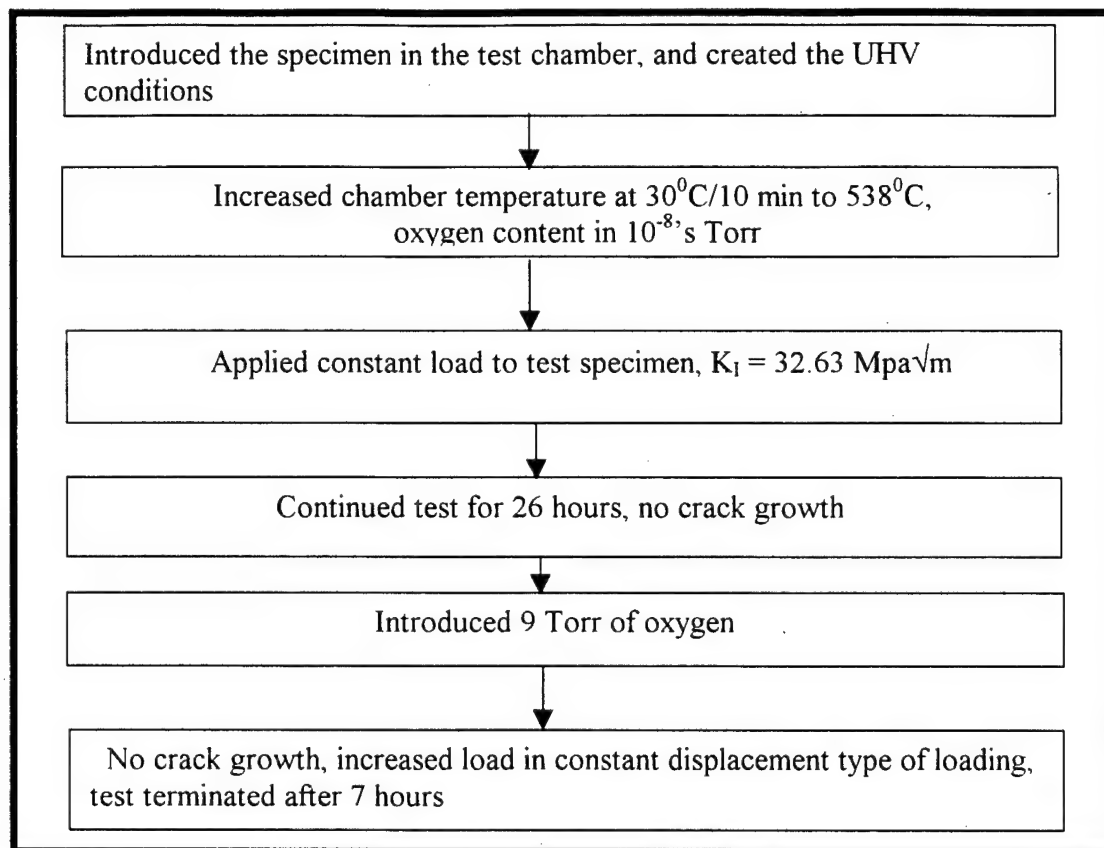


Figure 41: Testing Sequence for B6 Specimen

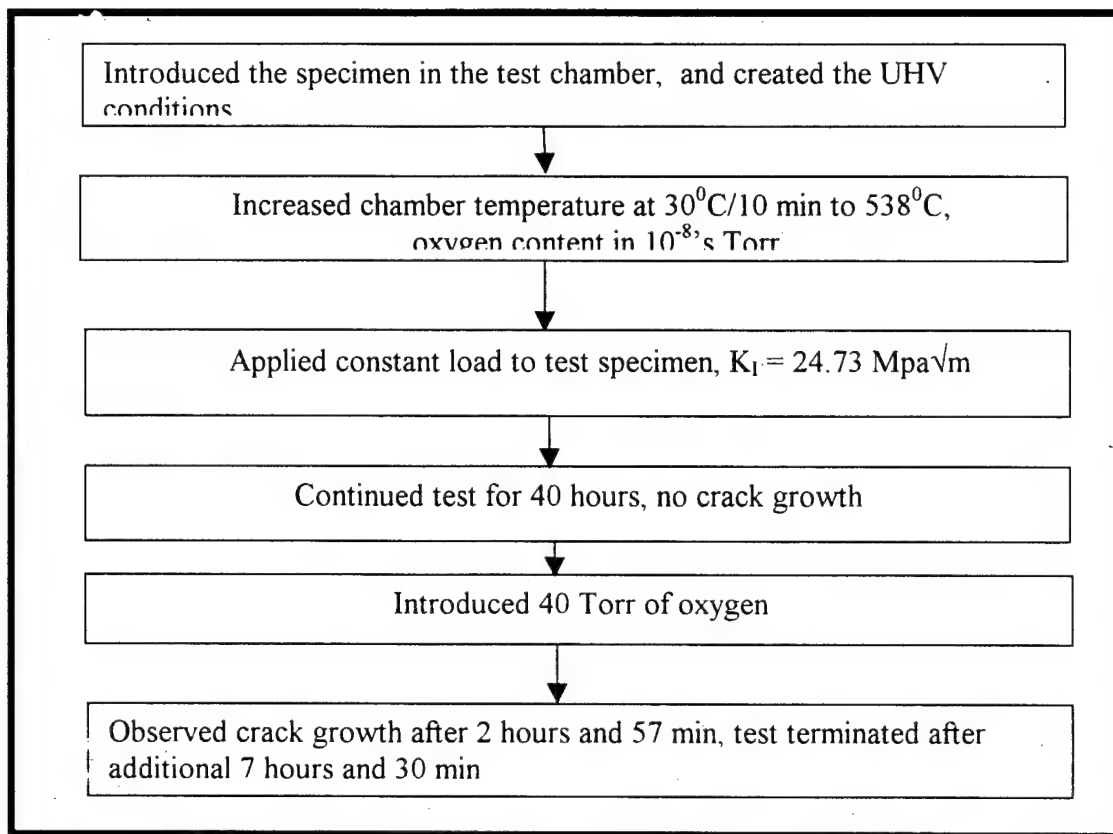


Figure 42: Testing Sequence for A4 Specimen

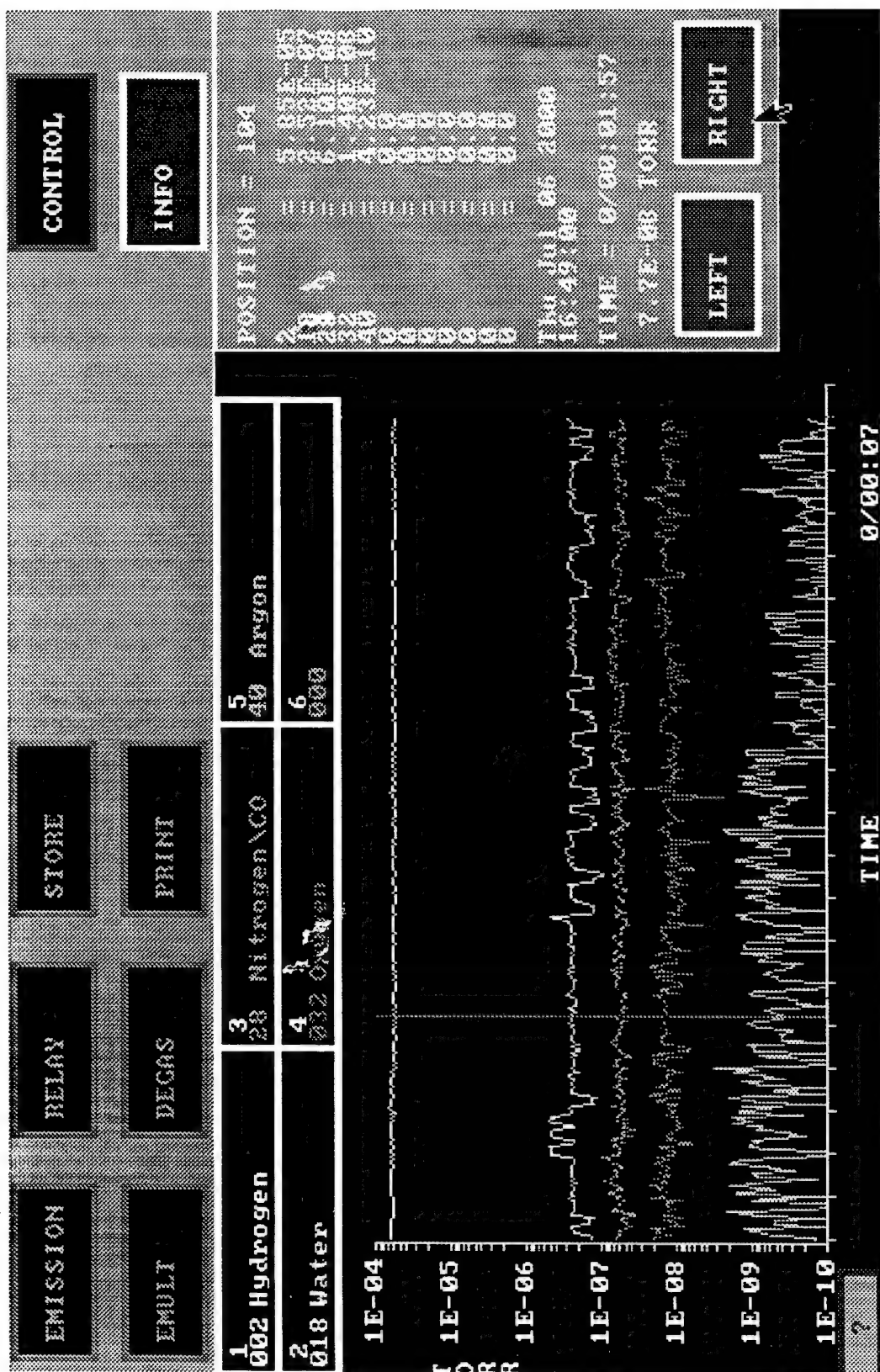


Figure43: Gas Composition in the Testing Chamber, 538°C.

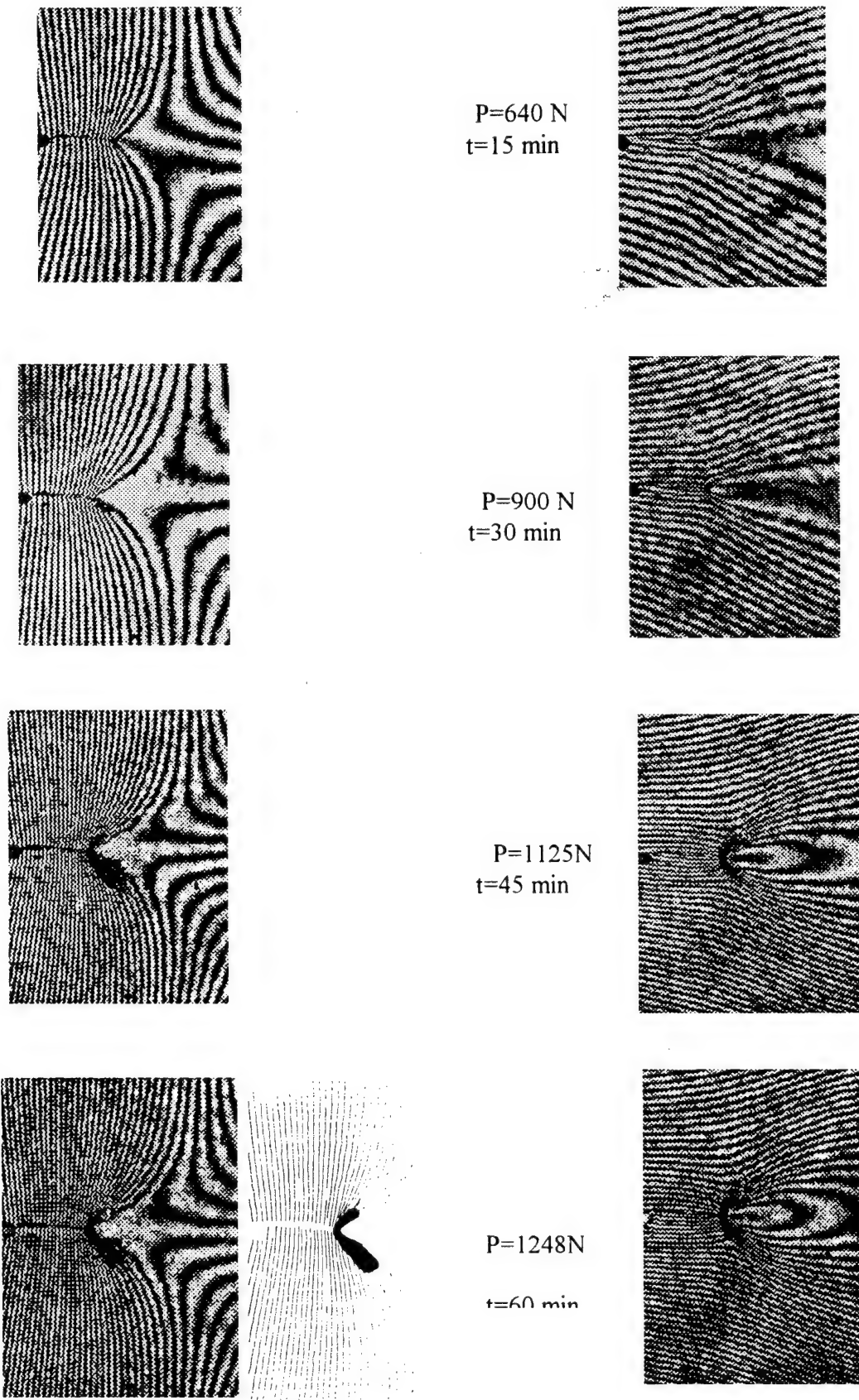


Figure 44, B6 Specimen, 538⁰C
vacuum 10⁻⁶ Torr

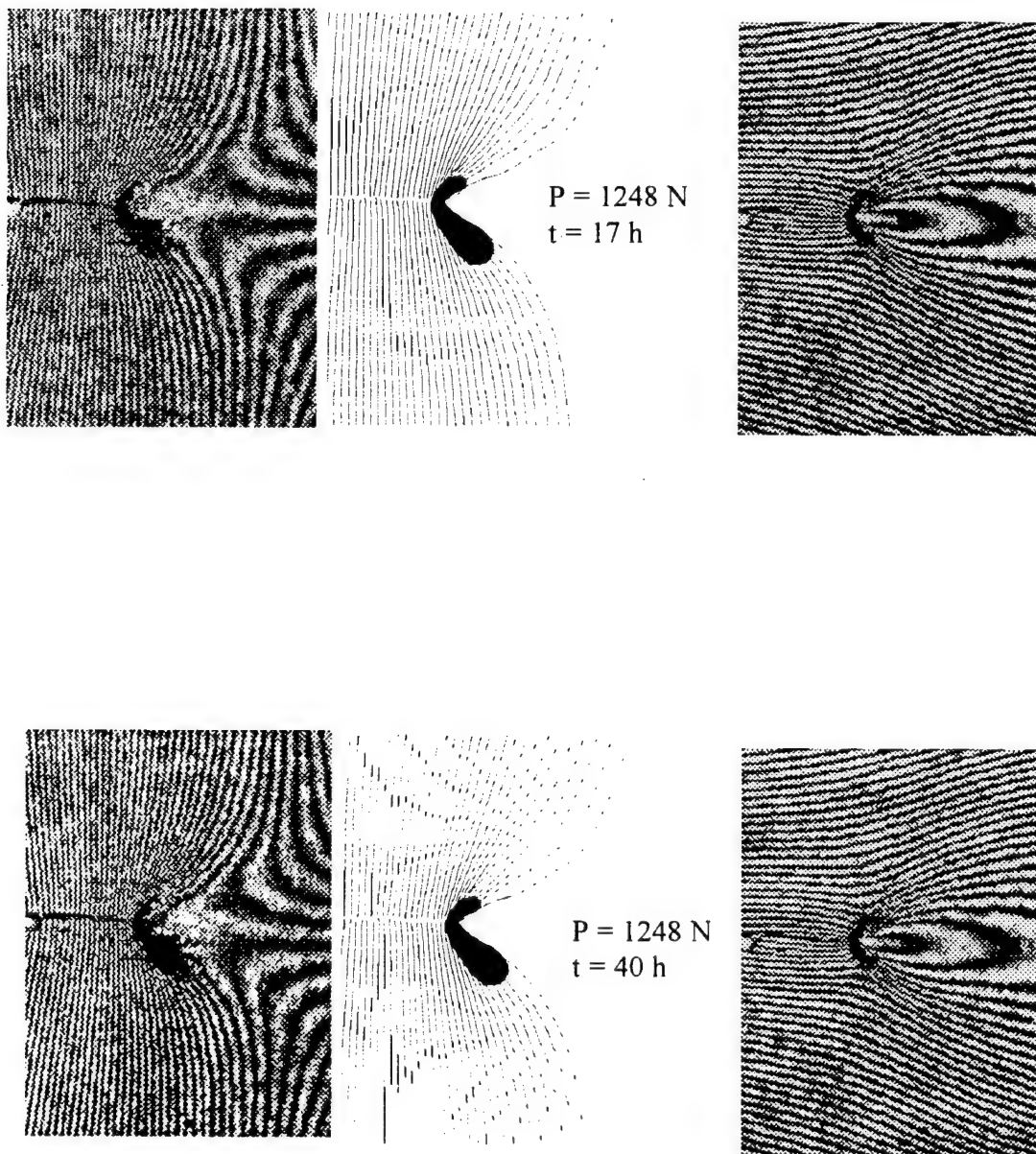
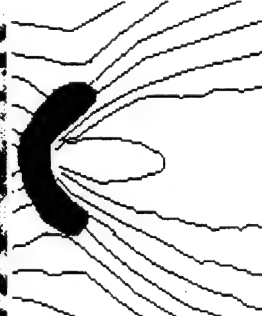
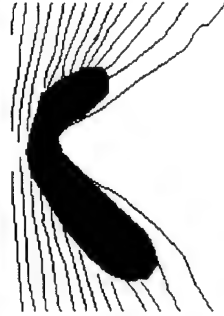
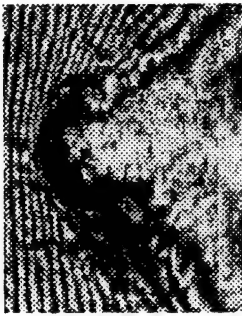


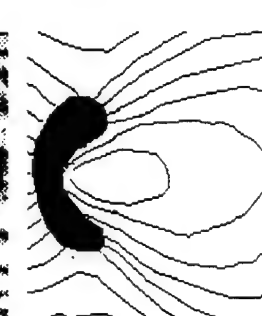
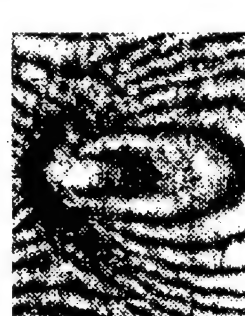
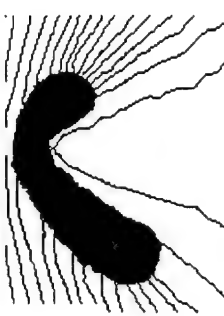
Figure 45: B6 Specimen, 538⁰ C
vacuum 10⁻⁶ Torr



$P = 1248 \text{ N}$
 $K_I = 24.73 \text{ Mpa}\sqrt{\text{m}}$
 Vacuum 10^{-6} Torr
 $t = 40 \text{ h}$ (oxygen input, 40 Torr)



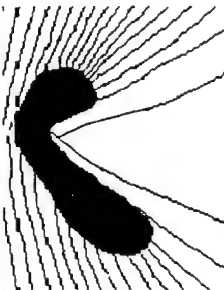
$\Delta a = 0.07 \text{ mm}$



$t = 2 \text{ h } 57 \text{ min}$
 (after oxygen input, 40 Torr)



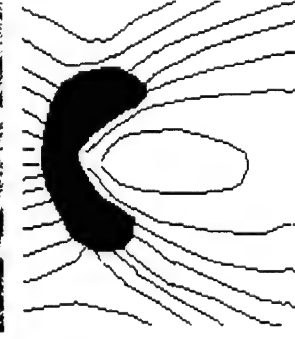
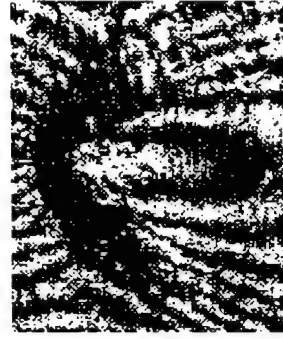
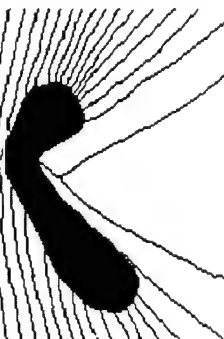
$\Delta a = 0.09 \text{ mm}$



$t = 4 \text{ h}$
 (after oxygen input, 40 Torr)

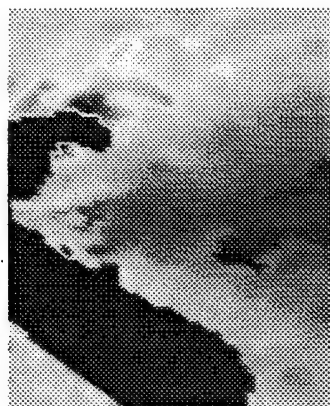
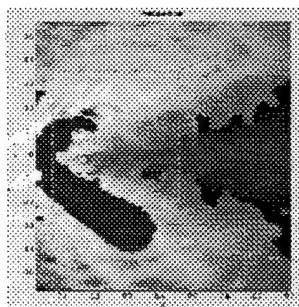


$\Delta a = 0.11 \text{ mm}$

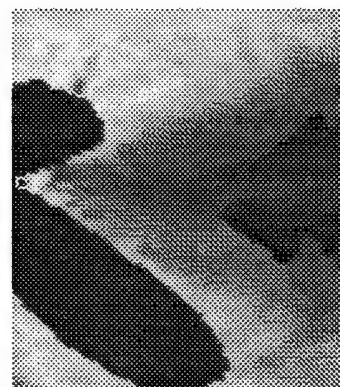
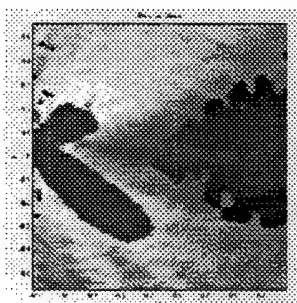


$t = 7 \text{ h}$
 (after oxygen input, 40 Torr)

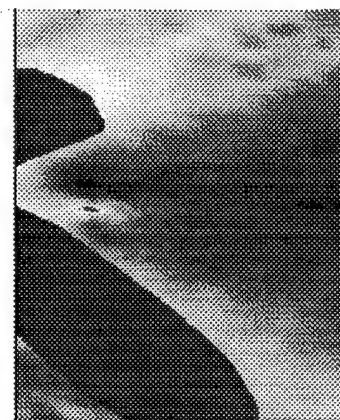
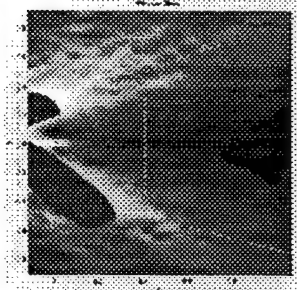
Figure 46: B6 specimen, 538°C



538°C, vacuum 10^{-6} Torr
t = 0 h



538°C, 40 Torr of oxygen
t = 2h 57min



538°C, 40 Torr of oxygen
t = 7h

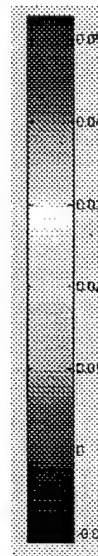
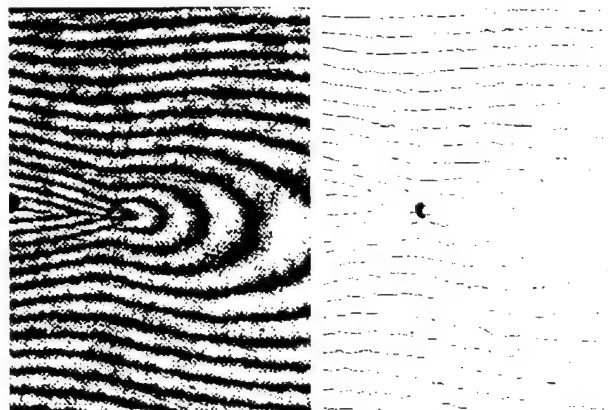
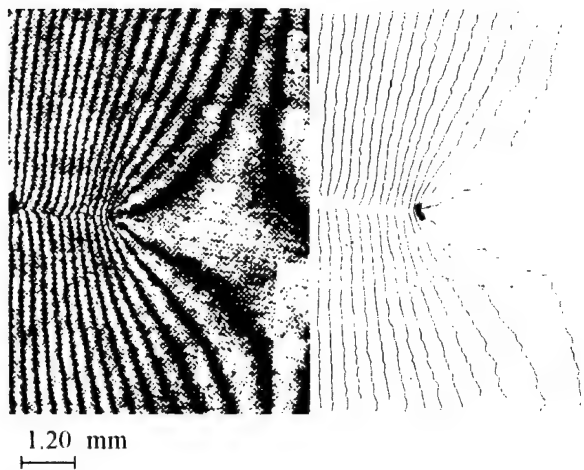
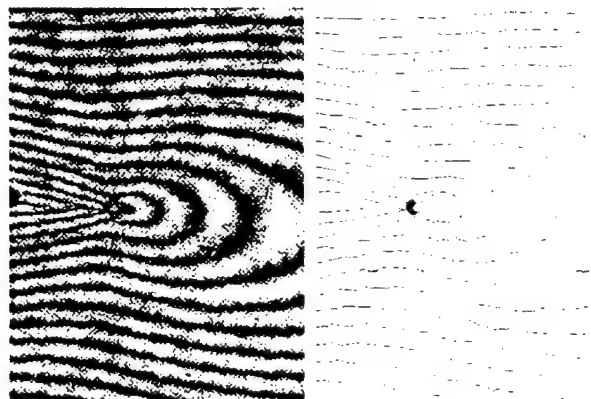
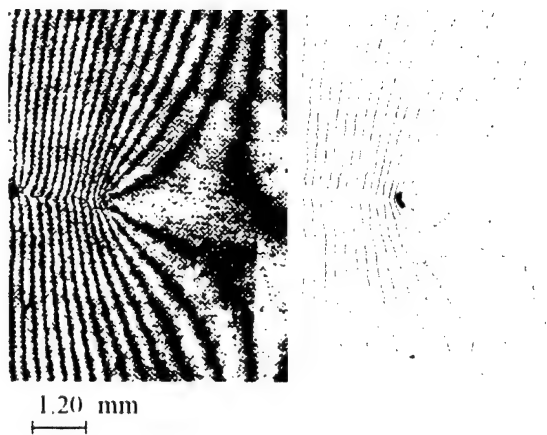


Figure 47: B6 specimen
Principal Strain Distribution



$P = 1545 \text{ N}$
 $K_I = 32.63 \text{ Mpa}\sqrt{\text{m}}$
 $t = 0 \text{ h}$

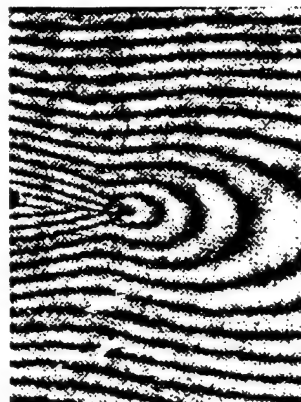
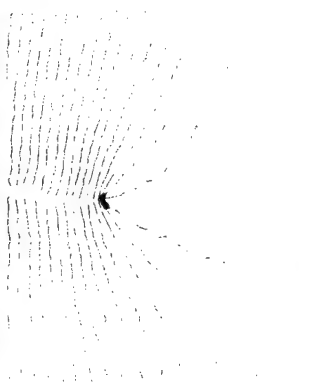


$P = 1545 \text{ N}$
 $K_I = 32.63 \text{ Mpa}\sqrt{\text{m}}$
 $t = 26 \text{ h}$
 oxygen input, 9 Torr

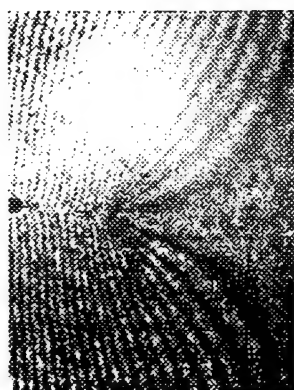
Figure 48: A4 specimen, 538° C
 vacuum 10^{-6} Torr



1.20 mm



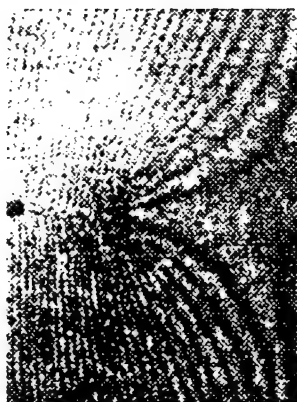
$P = 1545 \text{ N}$
 $K_I = 32.63 \text{ Mpa}\sqrt{\text{m}}$
 $t = 0 \text{ h}$



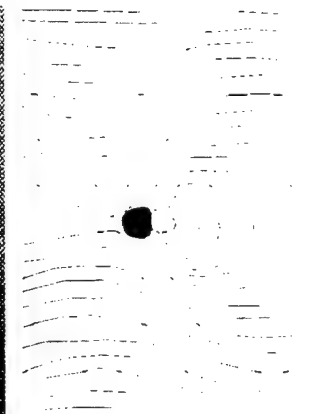
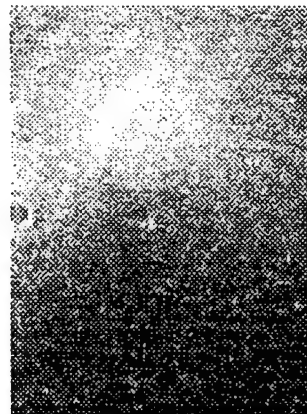
1.20 mm



$P = 1545 \text{ N}$
 $K_I = 32.63 \text{ Mpa}\sqrt{\text{m}}$
 $t = 4 \text{ h (after oxygen input)}$

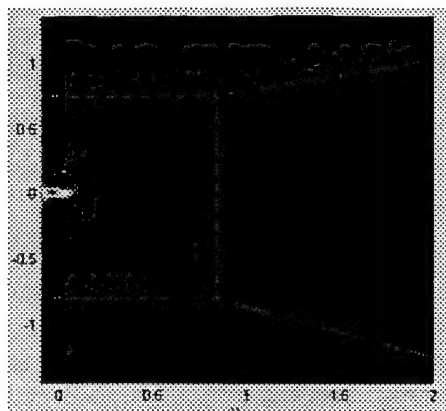


1.20 mm



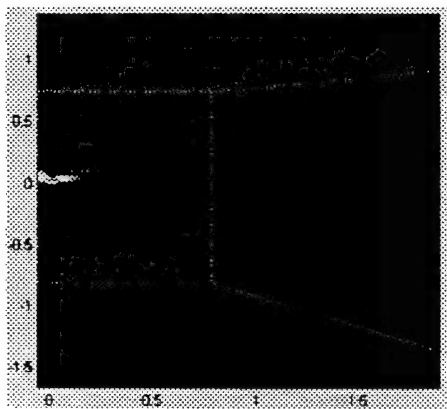
$P = 2034 \text{ N}$
 $K_I = 42.97 \text{ Mpa}\sqrt{\text{m}}$
 $t = 24 \text{ h (after oxygen input)}$

Figure 49: A4 specimen, 538°C



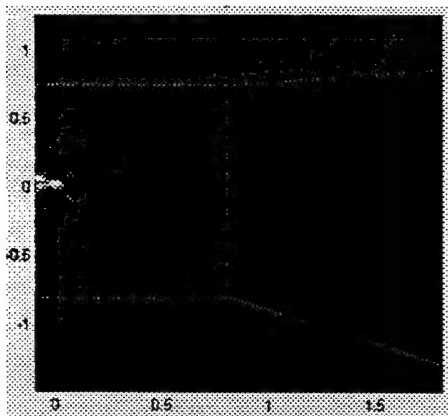
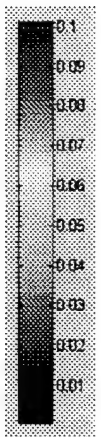
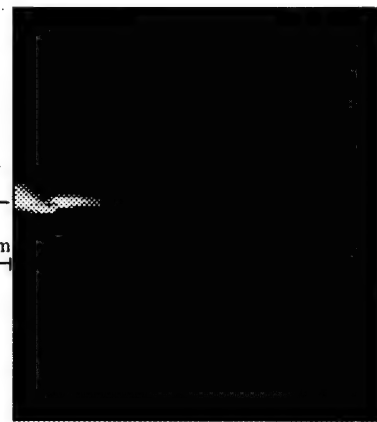
538° C, vacuum 10^{-6} Torr
t = 0 h

1.20 mm



538° C, 9 Torr of oxygen
t = 4 h (after oxygen input)

1.20 mm



538° C, 9 Torr of oxygen
t = 24 h (after increased load)

1.20 mm

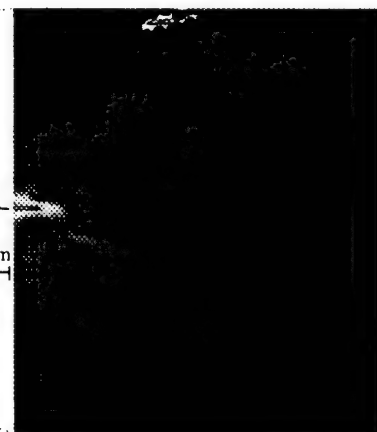


Figure 50: A4 specimen
Principal Strains Distribution

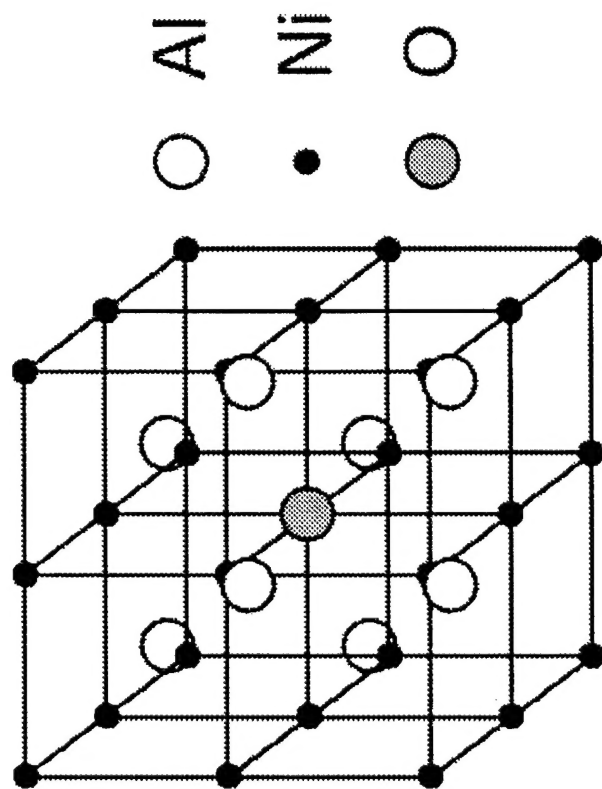


Figure 51. The 16-atom supercell used in the present work. The cubic supercell is built up from 2^3 unit cells of NiAl. The impurity atom (O) is placed at the center of the supercell, substituting for Ni in this picture (supercell $\text{Ni}_7\text{Al}_8\text{O}$). We also use a similar supercell, where the oxygen atom is placed at an Al site (supercell $\text{Ni}_8\text{Al}_7\text{O}$).

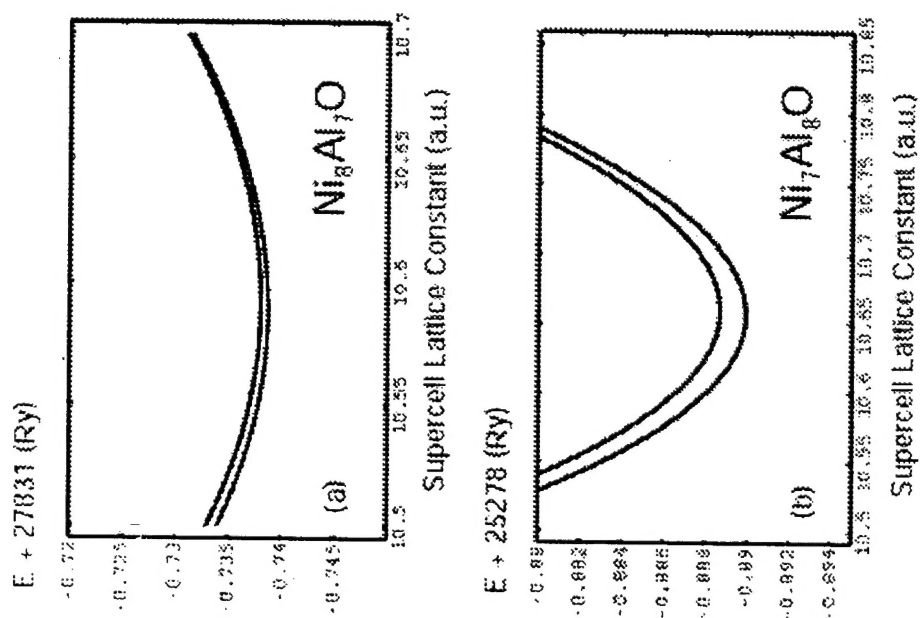


Figure 52. The FP-LMTO total energy with 16-atom supercell for the case of oxygen substituting for an aluminum atom (a), and oxygen substituting for a nickel atom (b). In both panels, the top curve is for an unrelaxed supercell while the bottom curve is for the relaxed supercell. The equilibrium lattice spacing and the relaxation energy are listed in Table III.

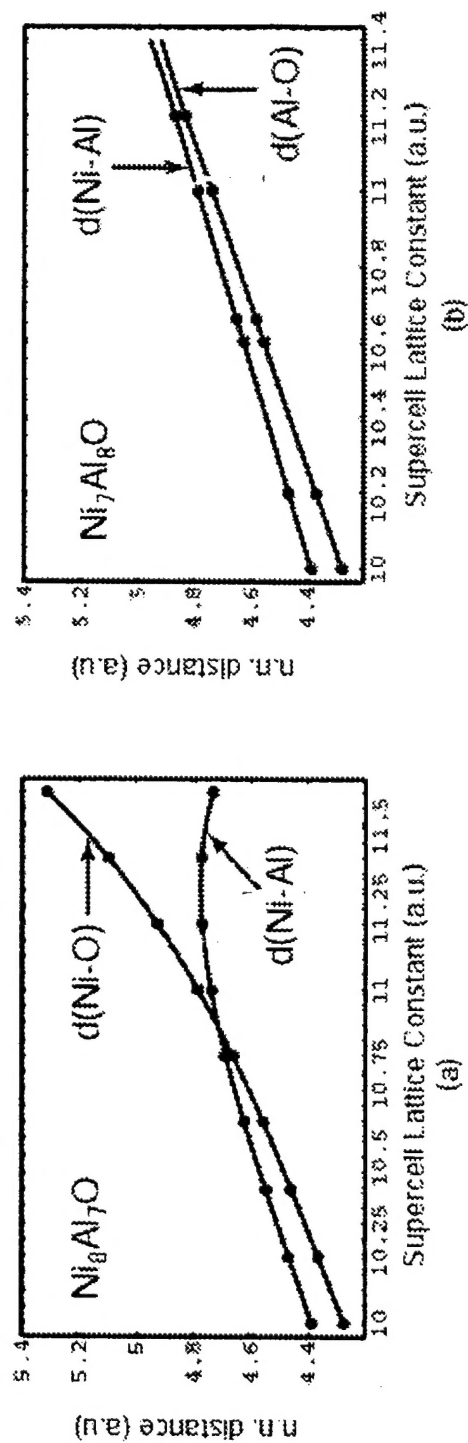


Figure 53. Nearest-neighbor (NN) distances between atoms in the unit cell on the (011) plane as a function of the supercell lattice constant. (a) Oxygen at Al site. For small lattice constants the movement of the Ni atoms is toward the central oxygen atom and away from the corner Al atoms. At large lattice constants the direction of movement reverses; the Ni atoms are displaced significantly closer to the corner Al atoms. This presumably reflects a steric repulsion between oxygen and nickel in the NiAl environment. (b) Oxygen at Ni site. Apparently, the Al atoms are attracted about equally strongly by the O and the Ni atoms. This results in small relaxation.

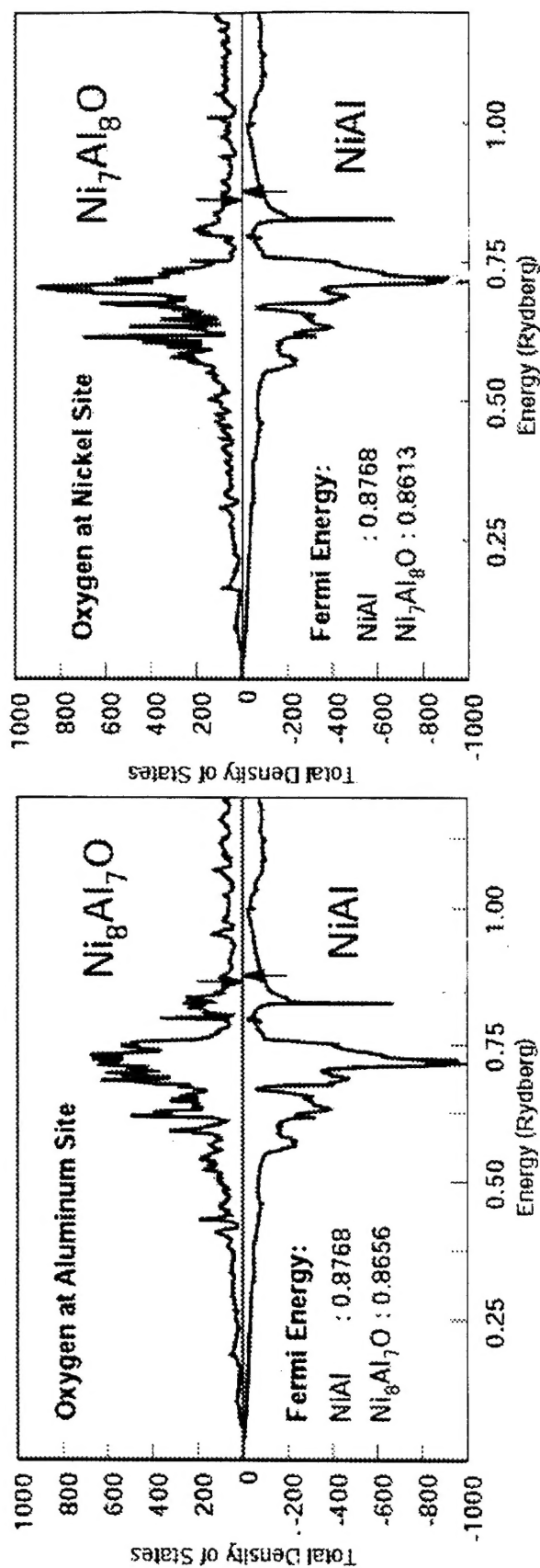


Figure 54. Total density of states for the 16-atom supercell calculated using the FP-LMTO method. For comparison, in each panel we also show the negative of the density of states for pure NiAl. Vertical arrows on the energy axis point to the positions of the Fermi energy. (a) Oxygen at Al site. (b) Oxygen at Ni site.